

## CONTENTS

<b>Mohammed Said Achbi, Sihem Kechida, Lotfi Mhamdi, Hedi Dhouibi</b> <i>A Neural-Fuzzy Approach for Fault Diagnosis of Hybrid Dynamical Systems: Demonstration on Three-Tank System.....</i>	1
<b>Volodymyr Kalchenko, Andriy Yeroshenko, Sergiy Boyko, Olga Kalchenko</b> <i>Modeling of Contact Geometry of Tool and Workpiece in Grinding Process with Crossed Axes of the Tool and Workpiece with Circular Profile.....</i>	9
<b>Mykhaylo Tkach, Yurii Halynkin, Arkadii Proskurin, Irina Zhuk , Volodymyr Kluchnyk, Igor Bobylev</b> <i>An Experimental Study of the Vibrational Characteristics of a Diamond Circular Blade Using Electronic Speckle-Pattern Interferometry and FEM.....</i>	16
<b>Mateusz Adamowicz, Leszek Ambroziak, Mirosław Kondratiuk</b> <i>Efficient Non-Odometry Method for Environment Mapping and Localisation of Mobile Robots .....</i>	24
<b>Askar Kudaibergenov, Askat Kudaibergenov, Danila Prikazchikov</b> <i>Near-Resonant Regimes of a Moving Load on a Pre-Stressed Incompressible Elastic Half-Space .....</i>	30
<b>Cezary Kownacki</b> <i>Self-Adaptive Asymmetrical Artificial Potential Field Approach Dedicated to the Problem of Position Tracking by Nonholonomic UAVs in Windy Environments .....</i>	37
<b>Borys Prydalnyi, Heorhiy Sulym</b> <i>Identification of Analytical Dependencies of the Operational Characteristics of the Workpiece Clamping Mechanisms with the Rotary Movement of the Input Link .....</i>	47
<i>Abstracts.....</i>	V

## ABSTRACTS

**Mohammed Said Achbi, Sihem Kechida, Lotfi Mhamdi, Hedi Dhouibi**

*A Neural-Fuzzy Approach for Fault Diagnosis of Hybrid Dynamical Systems: Demonstration on Three-Tank System*

This work is part of the diagnostic field of hybrid dynamic systems (HDS) whose objective is to ensure proper operation of industrial facilities. The study is initially oriented to the modelling approach dedicated to hybrid dynamical systems (HDS). The objective is to look for an adequate model encompassing both aspects (continuous and event). Then, fault diagnosis technique is synthesised using artificial intelligence (AI) techniques. The idea is to introduce a hybrid version combining neural networks and fuzzy logic for residual generation and evaluation. The proposed approach is then validated on three tank system. The modelling and diagnosis approaches are developed using MATLAB/Simulink environment.

**Volodymyr Kalchenko, Andriy Yeroshenko, Sergiy Boyko, Olga Kalchenko**

*Modeling of Contact Geometry of Tool and Workpiece in Grinding Process with Crossed Axes of the Tool and Workpiece with Circular Profile*

A general model is developed, and on its basis, there are special models formulated of the grinding process with crossed axes of the tool and workpiece with a profile in the form of a circle arc. A new method of control of the grinding process is proposed, which will provide processing by equidistant curves, and the amount of cutting of a circle equal to the allowance. This will increase the productivity and quality of grinding. The presented method of grinding implements the processing with the spatial contact line of the tool and workpiece. When the axes are crossed, the contact line is stretched, which leads to an increase of the contact area and, accordingly, to a decrease of the temperature in the processing area. This allows processing of workpieces with more productive cutting conditions.

**Mykhaylo Tkach, Yurii Halynkin, Arkadii Proskurin, Irina Zhuk, Volodymyr Kluchnyk, Igor Bobylev**

*An Experimental Study of the Vibrational Characteristics of a Diamond Circular Blade Using Electronic Speckle-Pattern Interferometry and FEM*

The compact installation and technology for determining vibration characteristics by the ESPI method has been created. The experimental determination of the dynamic characteristics of a diamond circular blade with a diameter of 203.4 mm and a thickness of 1.19 mm using real-time electronic speckle interferometry is presented. 15 mode shapes of vibration were detected in the range from 100 to 5000 Hz. The program calculation of the natural frequencies and mode shapes is carried out for three values of the clamping inner diameter (42 mm, 44 mm, 46 mm). The options for calculating a disk with a rim and without a rim are considered. It is shown that the minimum mean squared error of the calculation is achieved for the values of the diameter of the disk 46 mm, 42mm and 44 mm for the number of nodal circles 0, 1 and 2, respectively. To verify the accuracy of the interferometer, experimental, computational and analytical studies of console steel rod 200 x 22.25 x 3.78 mm in size were carried out.

**Mateusz Adamowicz, Leszek Ambroziak, Mirosław Kondratiuk**

*Efficient Non-Odometry Method for Environment Mapping and Localisation of Mobile Robots*

The paper presents the simple algorithm of simultaneous localisation and mapping (SLAM) without odometry information. The proposed algorithm is based only on scanning laser range finder. The theoretical foundations of the proposed method are presented. The most important element of the work is the experimental research. The research underlying the paper encompasses several tests, which were carried out to build the environment map to be navigated by the mobile robot in conjunction with the trajectory planning algorithm and obstacle avoidance.

**Askar Kudaibergenov, Askat Kudaibergenov, Danila Prikazchikov**

*Near-Resonant Regimes of a Moving Load on a Pre-Stressed Incompressible Elastic Half-Space*

The article is concerned with the analysis of the problem for a concentrated line load moving at a constant speed along the surface of a pre-stressed, incompressible, isotropic elastic half-space, within the framework of the plane-strain assumption. The focus is on the near-critical regimes, when the speed of the load is close to that of the surface wave. Both steady-state and transient regimes are considered. Implementation of the hyperbolic-elliptic asymptotic formulation for the surface wave field allows explicit approximate solution for displacement components expressed in terms of the elementary functions, highlighting the resonant nature of the surface wave. Numerical illustrations of the solutions are presented for several material models.

**Cezary Kownacki**

*Self-Adaptive Asymmetrical Artificial Potential Field Approach Dedicated to the Problem of Position Tracking by Nonholonomic UAVs in Windy Environments*

Artificial potential fields (APFs) are a popular method of planning and controlling the path of robot movement, including unmanned aerial vehicles (UAVs). However, in the case of nonholonomic robots such as fixed-wing UAVs, the distribution of velocity vectors should be adapted to their limited manoeuvrability to ensure stable and precise position tracking. The previously proposed local asymmetrical potential field resolves this issue, but it is not effective in the case of windy environments, where the UAV is unable to maintain the desired position and drifts due to the wind drift effect. This is reflected in the growth of position error, which, similar to the steady-state error in the best case, is constant. To compensate for it, the asymmetrical potential field approach is modified by extending definitions of potential function gradient and velocity vector field (VVF) with elements based on the integral of position tracking error. In the case of wind drift, the value of this integral increases over time, and lengths and orientations of velocity vectors will also be changed. The work proves that redefining gradient and velocity vector as a function of position tracking error integrals allows for minimisation of the position tracking error caused by wind drift.

**Borys Prydalnyi, Heorhiy Sulym**

*Identification of Analytical Dependencies of the Operational Characteristics of the Workpiece Clamping Mechanisms with the Rotary Movement of the Input Link*

The research is devoted to the problem of determining the efficiency of the workpiece fixing mechanism operation. Improving characteristics of workpiece fixing is one of the required conditions to increase the cutting modes, which may help to enhance the machining productivity. The study investigates the main characteristics and general features of a new structure of clamping mechanisms with electromechanical actuators for fixation of rotation bodies. The main advantages of using electromechanical clamping actuators with self-braking gear are presented. Two simplified dynamical models for the description of different stages of the clamping process are developed. The calculation scheme was formulated to find out how the mass-geometric parameters of mechanism elements should influence the main characteristics of the clamping mechanisms of this type.

# A NEURAL-FUZZY APPROACH FOR FAULT DIAGNOSIS OF HYBRID DYNAMICAL SYSTEMS: DEMONSTRATION ON THREE-TANK SYSTEM

Mohammed Said ACHBI\*, Sihem KECHIDA\*, Lotfi MHAMDI\*\*, Hedi DHOUBI\*\*

\*Laboratoire d'Automatique et Informatique de Guelma (LAIG), Université 8 Mai 1945 Guelma, BP 401, Guelma 24000, Algérie

\*\*Laboratory of Automatic Signal and Image Processing (LARATSI),  
National School of Engineers of Monastir, University of Monastir, 5019, Tunisia

[achbi.mohammedsaid@univ-guelma.dz](mailto:achbi.mohammedsaid@univ-guelma.dz), [kechida.sihem@univ-guelma.dz](mailto:kechida.sihem@univ-guelma.dz), [lotfienim@yahoo.fr](mailto:lotfienim@yahoo.fr), [hedi.dhouibi@laposte.net](mailto:hedi.dhouibi@laposte.net)

received 22 March 2020, revised 5 March 2021, accepted 10 March 2021

**Abstract:** This work is part of the diagnostic field of hybrid dynamic systems (HDS) whose objective is to ensure proper operation of industrial facilities. The study is initially oriented to the modelling approach dedicated to hybrid dynamical systems (HDS). The objective is to look for an adequate model encompassing both aspects (continuous and event). Then, fault diagnosis technique is synthesised using artificial intelligence (AI) techniques. The idea is to introduce a hybrid version combining neural networks and fuzzy logic for residual generation and evaluation. The proposed approach is then validated on three tank system. The modelling and diagnosis approaches are developed using MATLAB/Simulink environment.

**Key words:** hybrid dynamic systems, modelling, residual generation and evaluation, monitoring, fault diagnosis, neural-fuzzy approach

## 1. INTRODUCTION

Due to the rapid and significant development of the industrial world, the automation of industrial systems has become increasingly complex and the interaction between digital systems and continuous physical processes has given rise to a new class of so-called hybrid dynamic systems (HDS). The notion of the hybrid system refers to the set of dynamic systems in which both phenomena of a continuous and event nature interact.

The study of HDS has expanded rapidly in recent decades and has been the subject of several research works concerning the modelling, simulation, verification and synthesis of control laws (Sayed-Mouchaweh, 2018; Achbi & Kechida, 2017a; Favela Contreras, 1999). Monitoring of this class of systems has become a necessity, not only to mitigate the consequences of catastrophic failures (of different nature), but also to improve system performance and productivity (MI Rahal, 2018; Antsaklis & Koutsoukos, 1997; Tsuda et al., 2001).

In the literature, many diagnosis approaches have been developed for continuous and discrete event systems (Van Gorp, 2013; Zouaghi et al., 2011; Daher, 2018). Most of the work consists of either extending the existing techniques from continuous systems or discrete event systems to hybrid systems. In both cases, from a structural point of view, the diagnosis can only be partial. On the other hand, there is a scarcity of papers in the literature that consider both continuous and discrete dynamics (Belkhiat et al., 2011). Existing works can be divided into two categories according to whether the evolution of modes is known or not. In the case where the modes evolution of the system is unknown, the diagnosis of such system begins with the implementation of methods to know the active operating mode at any time.

In Cocquempot et al. (2004), the principle of parity space di-

agnosis is extended to a class of hybrid system (switching system). Another approach based on causal reasoning has been proposed in Karsai et al. (2003). This approach is based, firstly, on the modelling of the system by a hybrid bond-graph model and then the generation of a fault propagation graph, which makes it possible to describe the causal and temporal relations between the different modes of defaults, on the one hand, and the associated observations on the other. Alternatively, several researchers have opted for observer-based methods. For example, an active diagnosis, based on the predictive control theory associated with an observer's bench, is proposed in Tabatabaeipour et al. (2009). Pisano et al. (2014) use a sliding-mode observer to identify the active mode and detect a fault in an uncertain switching linear system (Pisano et al., 2014). A based method hybrid observer is proposed in Asma et al. (2015) to identify discrete fault and isolate sensor fault.

In Belkhiat et al. (2011), a dedicated robust observer is synthesised, using  $H_\infty$  theory, for the fault detection and isolation of a switched linear system; the synthesis is carried out under the assumptions that the system subject is capable of accepting an unknown input and/or modelling error and that the active mode is unknown. In the same perspective, a design of hybrid observer is proposed for robust fault detection and isolation (FDI) of sensor faults or discrete trajectories (Belkhiat et al., 2012).

In the same context and using other formalisms, a combination of Object Differential Petri nets and extended Kalman filter is developed for monitoring of chemical process (Olivier-Maget et al., 2008) and in Zouaghi et al. (2011), the authors present the Modified Particle Petri nets approach, which combines Petri nets and particle filtering applied to model and monitor a mobile robot.

More currently, artificial intelligence (AI) appeared as an alternative strategy for the monitoring of HDSs. Tools of AI are introduced either in modelling of system when the latter is complex or

in mechanism of residual generation and evaluation. These tools, such as Neural network, fuzzy logic or the hybrid version (neuro-fuzzy), are generally associated with classical approaches and usage of their complementarities to improve performance of diagnosis system.

In Pislariu et al. (2006), the paper details a monitoring methodology to diagnose machine faults in complex industrial processes using neuro-fuzzy system. Later, Subbaraj and Kannapiran develop Adaptive Network-based Fuzzy Inference System (ANFIS) approach for fault detection and diagnosis of a pneumatic valve used in cooler water spray system in cement industry (Subbaraj & Kannapiran, 2011). Then, the authors provide survey on applications of Neuro-Fuzzy system for diagnosis techniques and measurement (Viharos & Kis, 2015).

As for diagnosis methodologies based on hybrid automaton (HA), the literature in that field is abundant and different solutions have been proposed in Derbel (2009), Ekanayake et al. (2019), Belkacem et al. (2016) (Chanthery et al. (2015) Vento Maldonado et al. (2013), Vento Maldonado et al. (2013) and Sengupta et al. (2012) or in a mixed formalism [HA and parity space (Cocquempot et al., 2004), HA and state observers (Deng et al., 2015) and HA and bond graph (Abdallah et al., 2016)] combining the advantages of the both approaches for best performance of the diagnosis method.

In this paper, we propose a new diagnosis approach based on a combination of HA and ANFIS model. The latter is known by its capacities to solve the nonlinearity problems of a complex system (Mahmoud, 2018; Achbi & Kechida, 2020; Achbi & Kechida, 2017).

The main objective of this study is determining an adequate model for hybrid (and nonlinear) system, and then to look for a procedure of fault diagnosis through a method based on the Neural networks and fuzzy inference systems.

For modelling, the continuous dynamics is generated by a set of ANFIS models while the discrete dynamics is described by the evolution of HA modes. As for diagnosis part, fault indicators are generated through ANFIS models, and then evaluated using fuzzy reasoning to identify operating mode of process and classify faults.

The rest of this paper is organised in five sections. The second section exhibits a brief outline of Neural-fuzzy approach for fault diagnosis followed by modelling of hybrid dynamical systems used in this work (Section 3). The subsequent section is devoted to the application and discussion results. The final section concludes the paper and suggests some directions for future works.

## 2. NEURAL/FUZZY FAULT DIAGNOSIS

Generally, diagnosis is a very complex task and conventional analytical techniques often cannot provide acceptable solutions to diagnosis problems. This explains why AI techniques such as Neural networks and fuzzy logic are becoming increasingly popular in industrial diagnostic applications. The use of these techniques provides interpretable results and provides useful information for the decision phase.

The diagnosis task consists of two stages: residual generation and decision making. The generation of the residues makes it possible, from the available inputs and outputs of the system, to generate fault indicators. The generation process is based on a comparison between the observed behaviour of the system and

the expected reference behaviour (predicted by a model). On the other hand, the decision-making step consists in evaluating the residues in order to classify the detected defects.

The residue should be close to zero under normal conditions (no defects). On the contrary, in the fault occurrence, the value of this residue deviates from zero.

### 2.1. Residual generation using Neural-fuzzy system

Neural-fuzzy networks result from the association of Neural networks with fuzzy logic, so as to benefit advantages of each of these two techniques. The main characteristic of Neural-fuzzy models for industrial diagnostics is the ability to model non-linear processes and to process in a single tool the digital and symbolic knowledge of a system (Uppal et al., 2002). Diagnosis applications include mainly hybrid Neural-fuzzy models, for which Neural networks and fuzzy systems are homogeneously combined.

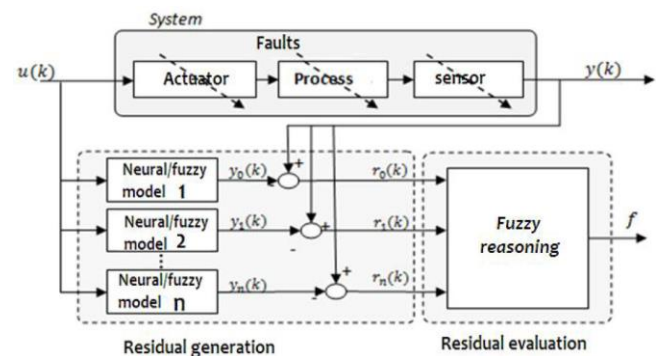


Fig. 1. Residuals generation and evaluation using Neural-fuzzy networks

Neural-fuzzy networks appear to be powerful tools combining large approximation capabilities for the modelling of nonlinear dynamical systems. To develop a diagnostic system using Neural-fuzzy models, several methods are available; nevertheless, they have some disadvantages (Achbi & Kechida, 2017). At the design level, it is necessary to have *a priori* sufficient knowledge of the system to diagnose to determine input variables, membership functions, and rules. So, it would be interesting to have clarification on the possibility of performing an online diagnosis.

Most of the applications encountered are based on the establishment of a diagnosis from the classification of residues, so they need to be able to establish a model of the system. In addition, they require a network by residues that make the system relatively complex and allow diagnosing only a limited number of defects. It will therefore be interesting to use these techniques, given their capabilities, by completely avoiding a model of the system to diagnose.

Hierarchical Neural-fuzzy networks can be used to solve the dimensionality problem by decomposition the system into a series of MISO systems and/or SISO systems called hierarchical systems. The criteria on which a Neural-fuzzy model is built are based on the requirements of the fault diagnosis model and the characteristics of the system. The residuals are obtained by comparing the outputs of the process and the outputs of the model. In normal operation, the residual value fluctuates around zero.

### 2.1.1. Adaptive Network-based Fuzzy Inference System (ANFIS)

The ANFIS may be the first integrated Neural-fuzzy system; it becomes more widespread, especially in approaches concerning fault diagnosis. Consequent to its capacities, it allows description of the behaviour of a complex system (Jang, 1992).

The ANFIS implements a fuzzy inference system of the Takagi Sugeno (TS) type and comprises five layers.

The first hidden layer is responsible for input variable mapping relative to each of the membership functions, i.e. this input layer is a layer that allows the 'fuzzification' of the variables. The T-standard operator is applied in the hidden second layer to compute the history of the rules. The third hidden layer normalises the results provided by the previous layer, followed by the fourth hidden layer where the consequent rules are determined. The output layer calculates the overall output as the sum of all the signals that arrive at that layer.

ANFIS uses back propagation learning to determine input membership function parameters and the least mean squares method to determine the consequent parameters. Each step of the iterative learning algorithm has two parts. In the first part, the back-propagation is used to update the antecedent parameters and the least mean squares to update the consequent parameters, while the antecedent parameters are considered to be fixed. In the second part, the input models are propagated again, and at each iteration, the back propagation learning algorithm is used to modify the parameters of the antecedents, while the consequents remain fixed. For more details, the readers can refer to Subbaraj and Kannapiran (2011).

## 2.2. Residual evaluation based on fuzzy model

The most common use of fuzzy logic in FDI methods is residual evaluation. There are three main approaches in the decision-making process: fuzzy adaptive threshold, fuzzy classification, and fuzzy reasoning.

### 2.2.1. Fuzzy reasoning

The main advantage of fuzzy reasoning is that it can mainly introduce heuristic information into the analysis scheme. Fuzzy reasoning schemes are also easy to understand. The basic idea behind the use of fuzzy inference for residual analysis is that each residue is zero, positive or negative compared to a certain degree. A fuzzy scheme has three steps:

#### 2.2.1.1. Fuzzification

This is the transformation of raw data values into fuzzy input values. For this, we determine for each input and output its fuzzy membership function.

#### 2.2.1.2. Inference

This step makes the determination of the basis of the rules that are formed to determine the conditions under which the defect exists and under which the system is non-defective.

For example:

- IF residue 1=0 AND residue 2=0, THEN, no fault detected.
- IF residue 1>0 AND residue 2 <0, THEN, fault 1 detected.

If the rules do not reflect the experience of an operator, then they can be difficult to validate.

### 2.2.1.3. Defuzzification

It is the step of constructing raw output values from the inference sets. The output of the logical decision procedure is a value that gives the degree to which a fault is present in the system, rather than a simple statement of default/non-default. This degree can be an indication of the size of the present defect, than the certainty with which a defect is present in the system. Such an output is given for each defect considered. The absence of formal methods of design represents one of the major drawbacks to realise FDI schemes.

## 3. MODELLING HYBRID DYNAMIC SYSTEM FOR DIAGNOSIS

When continuous and discrete dynamics coexist and interact with each other, it is important to develop models which exactly describe the dynamic behaviour of such dynamic systems, i.e. which model not only the continuous and discrete aspects but also their interactions (KECHIDA, 2007). For modelling HDS (Branicky, 1995), there are several approaches; the common point between them is that continuous evolution is affected by discrete events.

One of the most used modelling tools is the HA (Alur et al., 1992) which presents a more simplistic representation of Hybrid Systems (Fig. 2).

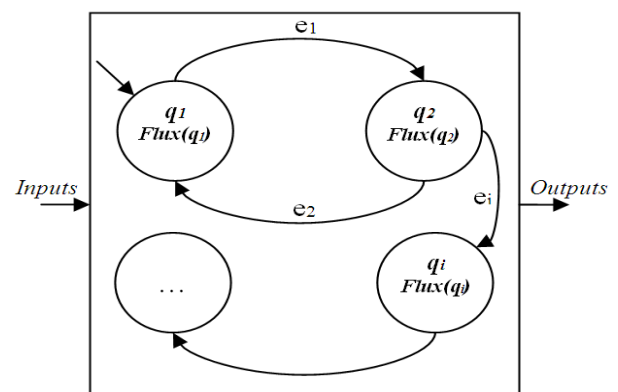


Fig. 2. HA – hybrid automata

### 3.1. Hybrid Automata (HA)

HA were introduced in the study of hybrid systems in the early 1990s; they are the generalised version of a classical finite state automaton. HA provide a general modelling formalism for the analysis of hybrid systems, which combines transitions (defined by invariants and guards) for capturing discrete evolution and a set of equations for capturing continuous behaviour.

The syntax of HA is defined as follows:

$$HA = (Q, \Sigma, X, flux, Init, \delta) \quad (1)$$

where:  $\Sigma$  is the set of system events;  $X$  is a finite set of continuous variables describing the continuous dynamics of the system;  $flux: Q \times X \rightarrow \mathbb{R}$  is a function characterising the continuous dynamic evolution of  $X$  in each state  $q$ ; and  $\delta: Q \times \Sigma \rightarrow Q$  is the state transition function of the system.

A transition  $\delta(q, e) = q_+$  corresponds to a change from state  $q$  to state  $q_+$  after the occurrence of discrete event  $e \in \Sigma$ ; also,  $Init = (q_1 \in Q, X(q_1), flux(q_1))$  is the set of initial conditions (Uppal et al., 2002).

### 3.2. Fault diagnosis through Neural-fuzzy and HA

The goal is to design a diagnoser to analyse, detect and locate a class of fault affecting a system. The mixed method is based on the use of HA, a tool for modelling

The goal is to design a diagnoser to analyse, detect and locate a class of fault affecting a system. The mixed method is based on the use of HA, a tool for modelling and monitoring methodology, combined with Neural-fuzzy models.

Fig. 3 illustrates the overall diagram of the diagnose design. This diagnosis strategy is applied to the hydraulic/thermal system.

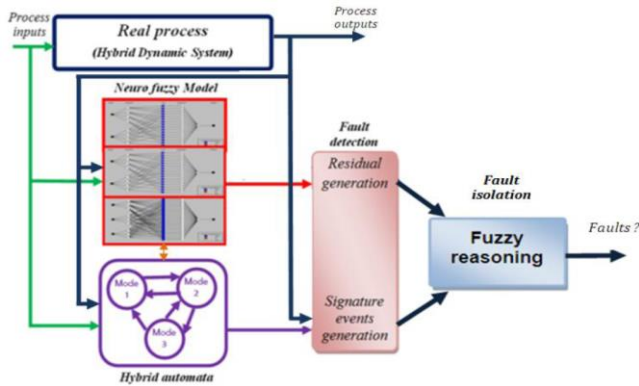


Fig. 3. The basic block diagram of the proposed approach

## 4. SYSTEM PRESENTATION

We consider a hydraulic/thermal process, as shown in Fig. 5. This system consists of three cylindrical tanks of identical section  $S = 0.0154m^2$ . The viscosity coefficients are given by  $\mu_1 = \mu_2 = 2.1082 \cdot 10^{-5}$  and  $\mu_3 = 4.2164 \cdot 10^{-5}$ .

Two pumps provide the same inlet flow  $Q_1$  and  $Q_2$  in each tank. The nominal system outlet flow is located at Tank 3. Two valves  $V_{13}$  and  $V_{23}$  allow the evacuation of the liquid in the third tank, which serves to mix the liquid and then evacuates the mixture through a valve  $V_3$ . The liquid temperature in the third tank is adjusted by an electrical resistance  $P_3$ .

The measurements are the temperature  $T_3$  in third tank and the liquid levels ( $h_1, h_2, h_3$ ) in each tank. The tanks are supposed to be perfectly insulated and their thermal capacities are negligible. The main goal is to keep the liquid level in tanks between 0.4 m and 0.6 m and the temperature in the third tank between 30 °C and 40 °C.

By carrying out the volume balance and the calorimetric balance, we obtain the nonlinear representation of the system:

$$\dot{h}_1 = \frac{1}{S} (Q_1 - \alpha_1 \sqrt{h_1}) \quad (2)$$

$$\dot{h}_2 = \frac{1}{S} (Q_2 - \alpha_2 \sqrt{h_2}) \quad (3)$$

$$\dot{h}_3 = \frac{1}{S} (\alpha_1 \sqrt{h_1} + \alpha_2 \sqrt{h_2} - \alpha_3 \sqrt{h_3}) \quad (4)$$

$$\dot{T}_3 = \frac{1}{Sh_3} \left[ \frac{P_3}{w.c} + Q_{13} \cdot (T_1 - T_3) + Q_{23} \cdot (T_2 - T_3) \right] \quad (5)$$

with  $c$  being the specific heat of the fluid; and  $w$  its volumetric mass density. The physical system is a nonlinear multivariable system composed of three actuators and six sensors. The control signals are  $P_3$ , the power delivered by the resistance; and  $Q_1, Q_2$ , the flow rates provided by the two pumps. The measurements are the temperatures ( $T_1, T_2, T_3$ ) and the liquid levels ( $h_1, h_2, h_3$ ) in each tank.

Fig. 5 illustrates the physical decomposition of the system.

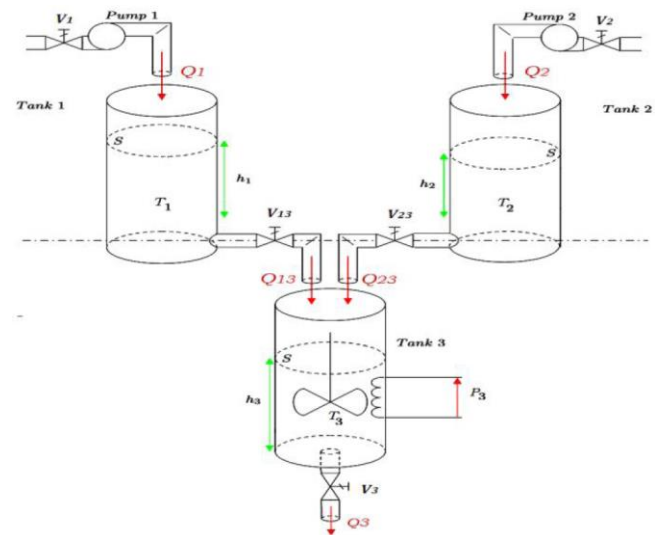


Fig. 4. Three tanks system diagram

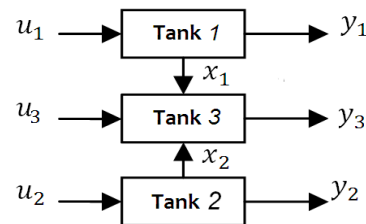


Fig. 5. The physical decomposition of the system

The command has all the possible inputs  $u = [Q_1, Q_2, P_3]^T$ . The valves ( $V_1, V_2, V_3$ ) are either open or closed. The outputs of the global system are:

$$Y = \begin{bmatrix} y_1 \\ y_2 \\ y_3 \end{bmatrix} = \begin{bmatrix} h_1 \\ h_2 \\ h_3, t_3 \end{bmatrix} \quad (6)$$



#### 4.1. Development of HA ANFIS Model for fault diagnosis

This hydraulic/thermal process explicitly and simultaneously involves models with continuous dynamics and event dynamics (discrete). The event part involves the notion of mode where each mode is associated with its own continuous dynamic. The set of modes characterises the complete operation of the system. An automaton generates the change from one mode to another by means of the measurements and taking into account all the controlled (opening and closing of valves and on/off of the resistance) and spontaneous events (dependencies of liquid level in tanks) generated by the system.

The goal is to design a diagnoser to analyse, detect and locate a class of fault affecting a system. The mixed method is based on the use of HA, a tool for modelling and monitoring methodology, combined with Neural-fuzzy models.

In normal operating, the nominal behavior is based on the values of the variables  $h_i$  ( $i = 1,2,3$ ) and status of discrete components ( $V_i$ , ( $i = 1,2,3$ ) and  $P_3$ ). It must verify operating constraints formulated by:  $0.4\text{m} < h_i < 0.6\text{m}$ , ( $i = 1,2,3$ ) and  $30^\circ\text{C} < T_3 < 40^\circ\text{C}$ .

The numerical values, considered in this study, of the various parameters are:  $Q_1 = 3.9 \cdot 10^{-6} \text{m}^3 \cdot \text{s}^{-1}$ ,  $Q_2 = 3.9 \cdot 10^{-6} \text{m}^3 \cdot \text{s}^{-1}$ ,  $w = 4180 \text{J} \cdot \text{kg}^{-3} \cdot \text{C}^{-1}$ ,  $c = 1000 \text{J} \cdot \text{kg}^{-3}$ ,  $P_3 = 500 \text{watt}$ ,  $\alpha_1 = \alpha_2 = 2.1082 \cdot 10^{-5}$ ,  $\alpha_3 = 4.2164 \cdot 10^{-5}$ . The system operates under the following initial conditions:  $h_{10} = 0.5\text{m}$ ,  $h_{20} = 0.5\text{m}$ ,  $h_{30} = 0.5\text{m}$ ,  $T_{10} = 10^\circ\text{C}$ ,  $T_{20} = 40^\circ\text{C}$ ,  $T_{30} = 32^\circ\text{C}$ .

Depending on the operation and the architecture of the system and on the basis of the input and output relation of a system, the nonlinear system can be expressed by a model composed of four ANFIS:

$$h_1(k) = F_1(Q_1(k-1), h_1(k-1)) \quad (7)$$

$$h_2(k) = F_2(Q_2(k-1), h_2(k-1)) \quad (8)$$

$$h_3(k) = F_3(h_1(k-1), h_2(k-1), h_3(k-1)) \quad (9)$$

$$T_3(k) = F_4(h_1(k-1), h_2(k-1), h_3(k-1), T_3(k-1)) \quad (10)$$

The normal behaviour of the process is depicted by HA. Fig. 6 describes the trajectories corresponding to the system configurations in normal operating. Each configuration is defined by the mode of the discrete state (valves status

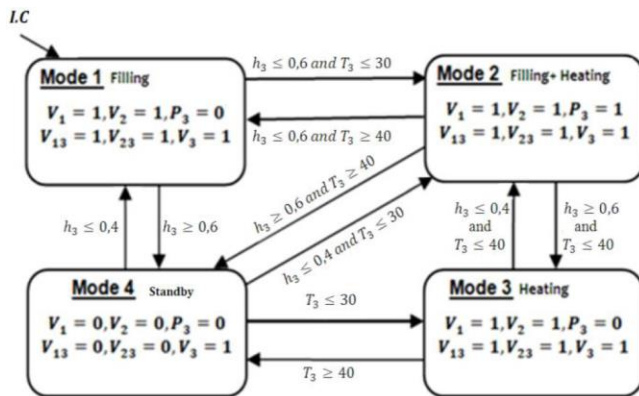


Fig. 6. Hybrid Automata

The goal is to design a diagnoser to analyse, detect and locate a class of fault affecting a system. The mixed method is based on the use of HA, a tool for modelling and monitoring methodology, combined with Neural-fuzzy models. Each configuration is defined by the mode of the discrete state (valves status  $V_i$  and  $T_3$ ), by the continuous evolution associated with this configuration (described by ANFIS models) and the domain of validity (constraints defined previously). The switching from one mode to another is conditioned by the level of the liquid  $h_3$  and/or its temperature.

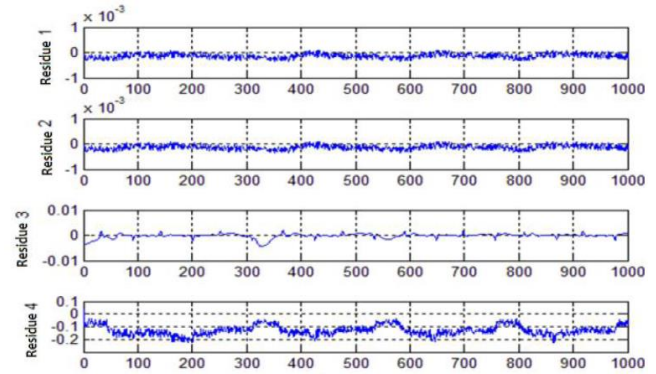


Fig. 7. Behaviour of residuals (case without fault)

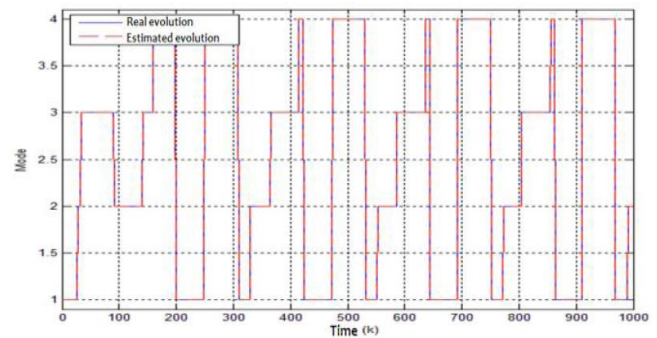


Fig. 8. Real and estimated mode evolution

Mode 1 (Filling): Tank 3 has to be filled until the level  $h_3$  has reached 0.6 m (All valves are opened).

Mode 2 (Filling and heating): The fluid in Tank 3 has to be heated between  $30^\circ\text{C}$  and  $40^\circ\text{C}$  ( $P_3$  is opened).

Mode 3 (heating): The temperature in Tank 3 exceeds  $40^\circ\text{C}$  ( $P_3$  The goal is to design a diagnoser to analyse, detect and locate a class of fault affecting a system. The mixed method is based on the use of HA, a tool for modelling and monitoring methodology, combined with Neural-fuzzy models.

Mode 4 (standby): Tanks 1 and 2 exceed limits and the temperature in Tank 3 exceeds  $40^\circ\text{C}$ ; (All valves and  $P_3$  are closed).

It should be noted that the model thus designed represents a reduced version of the overall behaviour of the system.

The modes evolution (discrete evolution) is illustrated by Fig. 8. It is clearly perceptible from Fig. 8 that the ANFIS models provide the same behaviour as real evolution described by nonlinear equations. The goal is to design a diagnoser to analyse, detect and locate a class of fault affecting a system. The mixed method is based on the use of HA, a tool for modelling and monitoring methodology, combined with Neural-fuzzy models.

A consistency test carried out between the observations taken and the evolution in normal mode is illustrated by the behaviour of



the residues (Fig. 7) where we can observe their convergences towards zero, thus indicating the absence of any anomaly in the system.

## 4.2. Diagnosis strategy

After the modelling step and the residual generation step, we proceed to residual evaluation. In this section, we consider faulty operation (with default), and we apply a fuzzy reasoning to classify 'intermittent' faults and specify the modes evolution of the system.

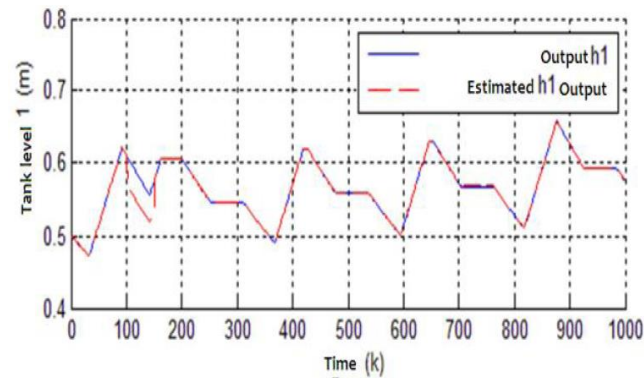
To illustrate the proposed method and to verify the efficiency and reliability of the diagnostic system, we consider fault scenarios, noted  $f$ , consisting of losses of efficiency valves  $V_1, V_2$  and power loss of the heating resistor of Tank 3.

In fact, the fault of  $V_1$  i.e. loss of efficiency of 5% signify that  $V_1$  is not entirely opened (it is partially opened).

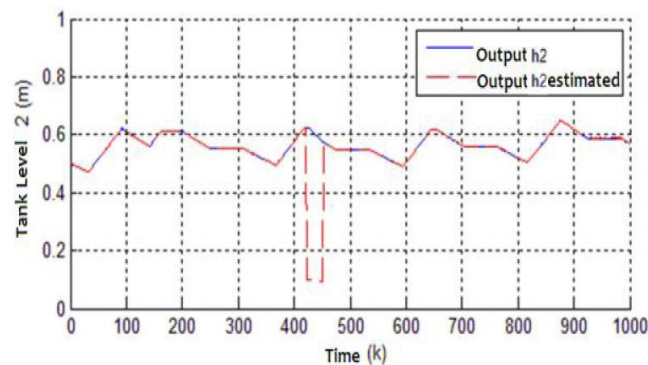
**Tab. 1.** Simulated faults.

Affected actuator	Fault	Fault appearance time	Loss of efficiency
$V_1$	$f_{V_1}$	[100 – 150]	5%
$V_2$	$f_{V_2}$	[420 – 450]	30%
$P_3$	$f_{P_3}$	[800 – 900]	50%

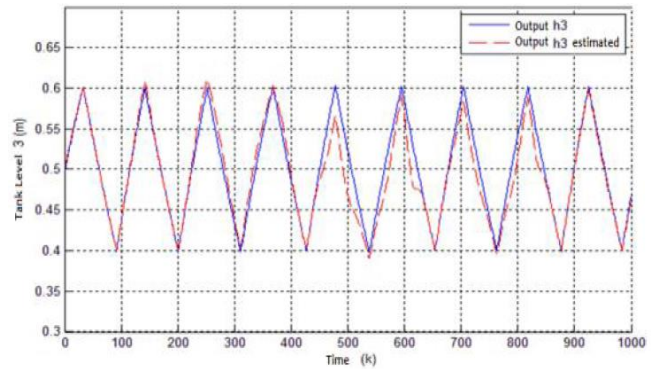
Figs. 9–11 depict dynamical evolution of three levels in presence of faults while Fig. 12 displays the temperature behaviour in Tank 3. Fig. 12 shows the effect of different faults on behaviour



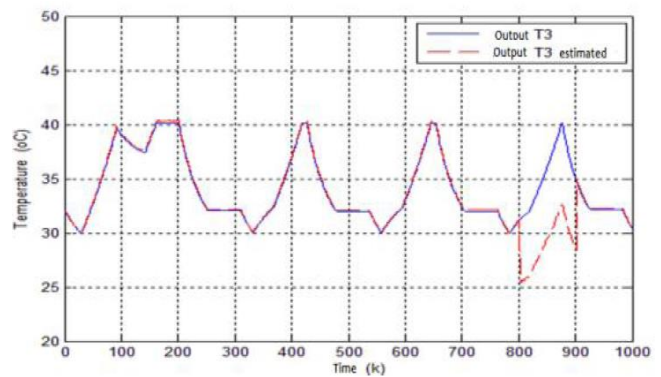
**Fig. 9.** Evolution of the output  $h_1$



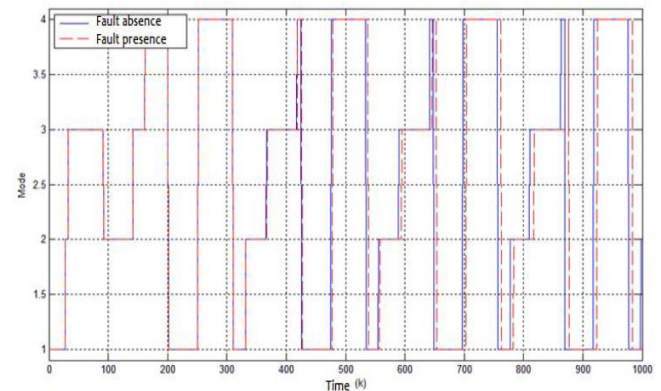
**Fig. 10.** Evolution of the output  $h_2$



**Fig. 11.** Evolution of the output  $h_3$

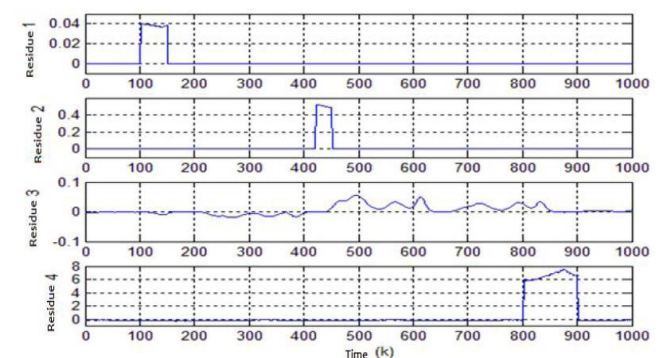


**Fig. 12.** Evolution of the output  $T_3$



**Fig. 13.** Mode sequence: Absence of faults (-), Presence of faults (- -)

The sensibility of generated residuals is shown in Fig. 14 where we clearly observe the corresponding default signature.



**Fig. 14.** Residuals behaviour

To evaluate these residuals, we apply the reasoning fuzzy to identify failures.

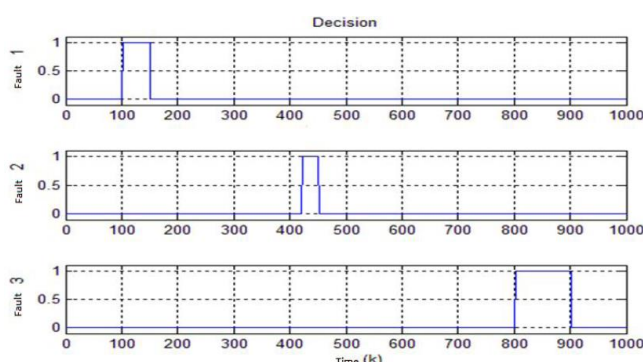


Fig. 15. Decision procedure

It is clear from Figs. 14 and 15 that the residues have almost zero values until the appearance time of the defects and the diagnosis system makes a positive decision between the two instants in the case where the fault causes the actuator input.

## 5. CONCLUSION

In this work, we have tackled a methodology for monitoring HDS using a combination of HA and AI techniques. The study has enabled us to confirm the advantages of AI techniques for the fault diagnosis of HDS. Also, the obtained results show detection efficiency and isolation ability in solving problems of diagnosis.

As future work, we propose to extend the proposed approach to diagnose the system in presence of simultaneous actuators and sensors faults. We plan also to study mastery of propagation of defects in a hybrid dynamic system.

## REFERENCES

1. Abdallah I., Gehin A.-L., Bouamama B. O. (2016), Event driven hybrid bond graph for diagnosis, *2016 European Control Conference (ECC)*, 2353–2358.
2. Abid A., Khan M.T., Lang H., de Silva C.W. (2019), Adaptive system identification and severity index-based fault diagnosis in motors, *IEEE/ASME Transactions on Mechatronics*, 24(4), 1628–1639.
3. Achbi M.S., Kechida S. (2017), Hybrid dynamic systems fault diagnosis approach based on hybrid automata and ANFIS, *The 2 Nd International Conference on Applied Automation and Industrial Diagnostics*, ICAAID2017.
4. Achbi M.S., Kechida S. (2017a), Fault diagnosis of a reverse osmosis water desalination plant through a hybrid approach, *ICENT2017*.
5. Achbi M.S., Kechida S. (2017b), Fault tolerant control of Reverse Osmosis Desalination Plant with the application of SCADA system, *The 2nd International Conference on Applied Automation and Industrial Diagnostics*, ICAAID2017.
6. Achbi M.S., Kechida S. (2020), Methodology for monitoring and diagnosing faults of hybrid dynamic systems: A case study on a desalination plant, *Diagnostyka*, 21(1), 1641–6414.
7. Achbi M.S., Mhamdi L., Kechida S., Dhouibi H. (2020), Methodology to knowledge discovery for fault diagnosis of hybrid dynamical systems: demonstration on two tanks system, *Diagnostyka*, 21.
8. Alur R., Courcoubetis C., Henzinger T.A., Ho P.-H. (1992), Hybrid automata: An algorithmic approach to the specification and verification of hybrid systems, *Hybrid systems*, 209–229, Springer.
9. Antsaklis P., Koutsoukos X. (1997), On hybrid control of complex systems: A survey, *ISIS*, 97, 017.
10. Asma T., Islem L., Zanzouri N., Ksouri M. (2015), Robust diagnosis for hybrid dynamical systems, *2015 IEEE 12th International Multi-Conference on Systems, Signals Devices (SSD15)*, 1–6.
11. Belkacem L., Mhamdi L., Simeu-Abazi Z., Messaoud H., Gascard E. (2016), Diagnosis of Hybrid Dynamical Systems through Hybrid Automata, *IFAC-PapersOnLine*, 49(12), 990–995.
12. Belkhiat D.E.C., Manamanni N., Messai N., Djemai M. (2012), Fault detection isolation for a class of hybrid systems: A dedicated switched robust observer scheme, *2012 20th Mediterranean Conference on Control Automation (MED)*, 984–989.
13. Belkhiat D.E.C., Messai N., Manamanni N. (2011), Design of a robust fault detection based observer for linear switched systems with external disturbances, *Nonlinear Analysis: Hybrid Systems*, 5(2), 206–219.
14. Branicky M. S. (1995), *Studies in hybrid systems: Modeling, analysis, and control*, Massachusetts Inst Of Tech Cambridge Lab For Information And Decision Systems.
15. Chanthery E., Pencolé Y., Ribot P., Travé-Massuyès L. (2015), *HYDIAG: Extended diagnosis and prognosis for hybrid systems*.
16. Chanthery E., Szyber A., Travé-Massuyès L., Pérez-Zuñiga C.G. (2020), Process decomposition and test selection for distributed fault diagnosis, *International Conference on Industrial, Engineering and Other Applications of Applied Intelligent Systems*, 914–925, Springer, Cham.
17. Cocquempot V., El Mezzyani T., Staroswiecki M. (2004), Fault detection and isolation for hybrid systems using structured parity residuals, *2004 5th Asian Control Conference (IEEE Cat. No. 04EX904)*, 2, 1204–1212.
18. Daher A. (2018), *Default diagnosis and prognosis for a preventive and predictive maintenance, Application to a distillation column* [PhD Thesis].
19. Deng Y., D'Innocenzo, A., Julius A.A. (2015), Trajectory-based observer for hybrid automata fault diagnosis, *2015 54th IEEE Conference on Decision and Control (CDC)*, 942–947.
20. Derbel H. (2009), *Diagnostic à base de modèles des systèmes temporisés et d'une sous-classe de systèmes dynamiques hybrides* [PhD Thesis].
21. Ekanayake T., Dewasurendra D., Abeyratne S., Ma L., Yarlagaadda P. (2019), Model-based fault diagnosis and prognosis of dynamic systems: A review, *Procedia Manufacturing*, 30, 435–442.
22. Favela Contreras A. (1999), *Modélisation et analyse du comportement dynamique des systèmes hybrides: Une approche basée sur le modèle d'automate hybride* [PhD Thesis], Grenoble INPG.
23. Gara H., Saad K.B. (2020), Fault diagnosis for hybrid systems based on a bank of linear observers and a discrete automaton, *SN Applied Sciences*, 2(11), 1–9.
24. Guo D., Zhong M., Ji H., Liu Y., Yang R. (2018), A hybrid feature model and deep learning based fault diagnosis for unmanned aerial vehicle sensors, *Neurocomputing*, 319, 155–163.
25. Jang J.-S. (1992), *Neuro-fuzzy modeling: Architectures, analyses, and applications*, University of California, Berkeley.
26. Karsai G., Abdelwahed, S., Biswas, G. (2003), Integrated diagnosis and control for hybrid dynamic systems, *AIAA Guidance, Navigation, and Control Conference and Exhibit*, 5673.
27. Kechida S. (2007), *Synthèse des générateurs de résidus robustes pour la détection de défauts* [PhD Thesis], Université de Annaba-Badji Mokhtar.
28. Mahmoud M.S. (2018), *Fuzzy control, estimation and diagnosis*, Saudi Arabia: Springer International.
29. Mhamdi L., Achbi M. S., Dhouibi H., Kechida S. (2020), Diagnosis of hybrid systems through bond graph, observers and timed automata, *Diagnostyka*, 21.

30. **MI Rahal B.** (2018), Modeling and robust fault diagnosis of hybrid system based on hybrid bond graph approach, *Int Rob Auto J*, 4(4), 266–272.
31. **Olivier-Maget N., Hétreux G., Le Lann J.-M., Le Lann M.-V.** (2008), Fault detection and isolation based on the model-based approach: Application on chemical processes, *Computer Aided Chemical Engineering*, 25, 411–416, Elsevier.
32. **Patel H.R., Raval S.K., Shah V.A.** (2021), A novel design of optimal intelligent fuzzy TID controller employing GA for nonlinear level control problem subject to actuator and system component fault, *International Journal of Intelligent Computing and Cybernetics*.
33. **Pérez-Zuñiga G., Rivas-Perez R., Sotomayor-Moriano J., Sánchez-Zurita V.** (2020), Fault Detection and Isolation System Based on Structural Analysis of an Industrial Seawater Reverse Osmosis Desalination Plant, *Processes*, 8(9), 1100.
34. **Pisano A., Rapaić M. R., Usai E.** (2014), Discontinuous dynamical systems for fault detection, A unified approach including fractional and integer order dynamics, *Mathematics and Computers in Simulation*, 95, 111–125.
35. **Pislaru M., Trandabat A.F., Schreiner C.** (2006), *Neuro-fuzzy surveillance for industrial process fault detection*.
36. **Rivas-Perez R., Sotomayor-Moriano J., Pérez-Zuñiga G., Soto-Angles M.E.** (2019), Real-time implementation of an expert model predictive controller in a pilot-scale reverse osmosis plant for brackish and seawater desalination, *Applied Sciences*, 9(14), 2932.
37. **Sadhukhan C., Mitra S.K., Naskar M.K., Sharifpur M.** (2021), Fault diagnosis of a nonlinear hybrid system using adaptive unscented Kalman filter bank, *Engineering with Computers*, 1–12.
38. **Sayed-Mouchaweh M.** (2018), *Fault diagnosis of hybrid dynamic and complex systems*, Springer.
39. **Sengupta S., Mukhopadhyay S., Deb A., Pattada K., De S.** (2012), Hybrid automata modeling of SI gasoline engines towards state estimation for fault diagnosis, *SAE International Journal of Engines*, 5(3), 759–781.
40. **Subbaraj P., Kannapiran B.** (2011), Adaptive neuro-fuzzy inference system approach for fault detection and diagnosis of pneumatic valve in cement industry, *International Journal of Computational Intelligence and Applications*, 10(04), 399–423.
41. **Sun S., Cui Z., Zhang X., Tian W.** (2020), A hybrid inverse problem approach to model-based fault diagnosis of a distillation column, *Processes*, 8(1), 55.
42. **Tabatabaeipour S., Ravn A.P., Izadi-zamabadi R., Bak T.** (2009), Active diagnosis of hybrid systems—A model predictive approach, *2009 IEEE International Conference on Control and Automation*, 465–470.
43. **Tsuda K., Mignone D., Ferrari-Trecate G., Morari M.** (2001), Reconfiguration strategies for hybrid systems, *Proceedings of the 2001 American Control Conference (Cat. No. 01CH37148)*, 2, 868–873.
44. **Uppal F. J., Patton R. J., Palade V.** (2002), Neuro-fuzzy based fault diagnosis applied to an electro-pneumatic valve, *IFAC Proceedings Volumes*, 35(1), 477–482.
45. **Van Gorp J.** (2013), *Diagnostic et observation d'une classe de systèmes dynamiques hybrides, Application au convertisseur multicellulaire série* [PhD Thesis].
46. **Vento Maldonado J., Travé-Massuyès L., Sarrate Estruch R., Puig Cayuela V.** (2013), Hybrid automaton incremental construction for online diagnosis, *Proceedings DX'13*, 186–191.
47. **Viharos Z. J., Kis K. B.** (2015), Survey on neuro-fuzzy systems and their applications in technical diagnostics and measurement, *Measurement*, 67, 126–136.
48. **Zhirabok A., Shumsky A.** (2018), Fault diagnosis in nonlinear hybrid systems, *International Journal of Applied Mathematics and Computer Science*, 28(4), 635–648.
49. **Zouaghi L., Alexopoulos A., Wagner A., Badreddin E.** (2011), Modified particle petri nets for hybrid dynamical systems monitoring under environmental uncertainties, *2011 IEEE/SICE International Symposium on System Integration (SII)*, 497–502.

# MODELLING OF CONTACT GEOMETRY OF TOOL AND WORKPIECE IN GRINDING PROCESS WITH CROSSED AXES OF THE TOOL AND WORKPIECE WITH CIRCULAR PROFILE

Volodymyr KALCHENKO\*, Andriy YEROSHENKO\*, Sergiy BOYKO\*, Olga KALCHENKO\*

\*Mechanical Engineering Department, Chernihiv National University of Technology,  
95 Shevchenko street, 14035, Chernihiv, Ukraine

[vvkalchenko74@gmail.com](mailto:vvkalchenko74@gmail.com), [yeroshenkoam@gmail.com](mailto:yeroshenkoam@gmail.com), [svboyko.cstu@gmail.com](mailto:svboyko.cstu@gmail.com), [onkalchenko.2014@gmail.com](mailto:onkalchenko.2014@gmail.com)

received 28 April 2020, revised 9 March 2021, accepted 15 March 2021

**Abstract:** A general model is developed, and on its basis, there are special models formulated of the grinding process with crossed axes of the tool and workpiece with a profile in the form of a circle arc. A new method of control of the grinding process is proposed, which will provide processing by equidistant curves, and the amount of cutting of a circle equal to the allowance. This will increase the productivity and quality of grinding. The presented method of grinding implements the processing with the spatial contact line of the tool and workpiece. When the axes are crossed, the contact line is stretched, which leads to an increase of the contact area and, accordingly, to a decrease of the temperature in the processing area. This allows processing of workpieces with more productive cutting conditions.

**Key words:** circular arc, grinding, equidistant curves, cutting edge, abrasive surface, abrasive materials, crossed axes, abrasive wheel, heat stress, grinding performance

## 1. INTRODUCTION

Parts with high-precision surfaces and a profile in the form of arc of a circle, the final quality of which is ensured by abrasive machining, are widespread in modern mechanical engineering. Therefore, the amount of processing with abrasive tool is constantly growing in the total volume of the processing complexity.

One of the means of increasing the productivity and accuracy of grinding surfaces with a profile in the form of an arc of a circle is the development of grinding methods with intersecting axes of the tool and workpiece.

For grinding surfaces with a profile in the form of a circular arc angle of crossing axes, circle and part is a parameter that affects the productivity and quality of the grinding. It determines the distribution of the allowance and the amount of cutting the tool, the heat intensity of the grinding process, and the location and resistance of the forming section of the circle.

Therefore, for the effective processing of such surfaces, it is necessary to determine the optimal angles of the crossing axes of the workpiece and the tool (stationary or controlled), which provide an increase in productivity and accuracy of processing.

The main problem of grinding parts with a circular profile is the low resistance of the profile of abrasive tool, especially when grinding surfaces having high hardness and large machining allowances (Anderson et al., 2011; Kalpana et al., 2018). It is the crossing of the axes of the circle and the workpiece that determines the position of the forming section. Its combination with the normal along the coordinate of the processing makes it possible to compensate for the influence of the wear of the wheel profile on the accuracy of shaping, and increases the productivity and durability of the abrasive tool.

The development of new grinding methods with crossing axes of tool and parts with a profile in the form of a circular arc, and the

determination of rational angles axes crossing and tool profiling are urgent tasks of the grinding process, the solution of which will significantly increase productivity and machining accuracy, and ensure the abrasive wheel durability and the required quality of the machined surfaces.

Using the tool-oriented machining method, when the tool further alters the angular orientation with respect to the workpiece during cutting, it thereby eliminates the disadvantages of grinding with parallel axes of the tool and workpiece (Kalchenko et al., 2018). The removal of the allowance when grinding with the crossed axes is due to the transverse movement of the circle and its rotation relative to the straight line connecting the axis of rotation of the tool and the workpiece.

Thus, the purpose of the work is to develop a common model and, on its basis, special models of the grinding process with crossed axes of the tool and workpiece with circular profile.

## 2. THE GENERAL MODEL OF THE NOMINAL SURFACE OF THE WORKPIECE

In the works of other authors (Cong et al., 2018; Kacalak et al., 2018) there is a discussion concerning the development of a general model; to enable this development, it is necessary to solve the direct problem of the theory of formation. For this we need to mathematically describe complex surface detail, which is the general case all possible surfaces.

The surface of the workpiece is described by a spherical module. The sphericity of the module is caused by the presence of two independent angular parameters:  $\theta_w$  – is the angle of rotation around the axis of the workpiece rotation, and  $\varphi_w$  – angular coordinate of a circular profile, which may take a positive or negative value depending on the location of the starting point relative to the axial plane of the profile. All other model param-



ters are functionally dependent on these two parameters.

The mathematical description of nominal workpiece surface can be performed by spherical module:

$$\bar{r}_w = S_{z_w \theta_w y_w \varphi_w y_p}^w \cdot e^{-4}, \quad (1)$$

where  $\bar{r}_w$  – is the radius vector of the points of the surface of a complex part;  $S_{z_w \theta_w y_w \varphi_w y_p}^w$  – spherical module a matrix of switching from the starting point in a coordinate system of the workpiece; and  $e^{-4} = (0,0,0,1)^T$  – radius vector of starting point (Kalchenko et al., 2018).

Spherical module of workpiece is a product of one-coordinate matrix (Kalchenko et al., 2018):

$$S_{z_w \theta_w y_w \varphi_w y_p}^w = M_3(z_w) M_6(\theta_w) \cdot M_2(y_w) \cdot M_4(\varphi_w) \cdot M_2(y_p), \quad (2)$$

where  $z_w$  – the axial coordinate of the profile offset which providing the screw surface;  $\theta_w$  – is the angle of rotation around the axis of the workpiece rotation;  $y_w$  – is the distance from the center of the profile to the axis of the workpiece rotation;  $\varphi_w$  – is the angle of rotation around the axis of OX;  $y_p = \rho_w$  – is the radius profile of the workpiece.

Thus, the matrices (Kalchenko et al., 2018), of which the module consists, have the following physical meaning:

$$M_2(y_p) = \begin{pmatrix} 1 & 0 & 0 & 0 \\ 0 & 1 & 0 & \pm y_p \\ 0 & 0 & 1 & 0 \\ 0 & 0 & 0 & 1 \end{pmatrix} - \text{the point displacement matrix}$$

along the axis  $O_w Y_w$ . Since the radius of curvature of the profile of a complex part varies depending on the axial coordinate  $z_w$ , which is functionally dependent on the angle of rotation  $\theta_w$ , the parameter  $y$  of the matrix  $M_2$  is a function of  $\theta_w$ :  $y_p = \rho_w(\theta_w)$ . In the particular case, when the radius of the workpiece profile does not change, the matrix parameter is converted to a constant. The sign ‘ $\pm$ ’ indicates that the radius can be set in different directions relative to the axis  $O_w Y_w$ . The sign ‘ $+$ ’ indicates a concave outer or convex inner profile, and a ‘ $-$ ’ indicates a convex outer or inner concave profile (Fig. 1).

$M_4(\pm \varphi_w) = \begin{pmatrix} \cos \varphi_w & 0 & \sin \varphi_w & 0 \\ 0 & 1 & 0 & 0 \\ -\sin \varphi_w & 0 & \cos \varphi_w & 0 \\ 0 & 0 & 0 & 1 \end{pmatrix}$  – matrix of generalized rotations of point about the axis  $O_w X_w$ . The range of parameter change lies within the central angle  $\xi$ .

The positive or negative values of the parameters  $\rho_w$  and  $\varphi_w$  are set depending on the direction of the axes of the selected coordinate system. Fig. 1 shows the directions of the axes of the coordinate system and the corresponding signs of the parameters  $\rho_w$  and  $\varphi_w$  for the various parts surfaces adopted in this work. For example, to describe the concave outer profile of the groove of the inner bearing ring  $\rho_w$  and  $\varphi_w$ , we take positive values (Fig. 1(a)), as well as for the convex outer profile of the belt pulley negative (Fig. 1(b)). Fig. 1 (a-d) shows surfaces with a central profile angle  $\xi = 180^\circ$ . Fig. 1(e) shows the general case of a concave outer surface for which the central angle is not equal to  $180^\circ$ .

$$M_2(y_w) = \begin{pmatrix} 1 & 0 & 0 & 0 \\ 0 & 1 & 0 & R_w \\ 0 & 0 & 1 & 0 \\ 0 & 0 & 0 & 1 \end{pmatrix} - \text{the point displacement matrix}$$

along the axis  $O_w Y_w$ , which sets the coordinate of the center of the

workpiece profile. For a complex part, this parameter, similar to  $y_p$ , is a function of the angle of rotation  $\theta_w$  and is converted to a constant value  $R_w$  for cylindrical parts.

$$M_6(\theta_w) = \begin{pmatrix} \cos \theta_w & -\sin \theta_w & 0 & 0 \\ \sin \theta_w & \cos \theta_w & 0 & 0 \\ 0 & 0 & 1 & 0 \\ 0 & 0 & 0 & 1 \end{pmatrix} - \text{a matrix of generalized rotations about the axis } O_w Z_w \text{ of the workpiece rotation.}$$

$$M_3(z_w) = \begin{pmatrix} 1 & 0 & 0 & 0 \\ 0 & 1 & 0 & 0 \\ 0 & 0 & 1 & z_w \\ 0 & 0 & 0 & 1 \end{pmatrix} - \text{axial displacement matrix of the profile.}$$

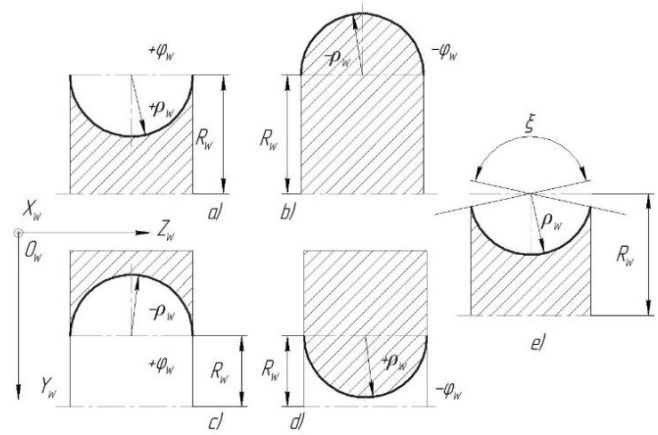


Fig. 1. Determining the type of workpiece profile

By rotating the profile of the workpiece around its axis of rotation with an angular coordinate  $\theta_w$  and giving it an axial offset with the coordinate  $z_w$ , we finally form the surface of the part. The axial coordinate of the screw surface  $z_w$  is a function of the angle of rotation of the workpiece:

$$z_w = \theta_w \cdot p \quad (3)$$

where  $p = \frac{S}{2\pi}$  – is screw motion parameter; and  $S$  – step screw surface.

Model (1) is general and describes all possible surfaces of parts with a circular profile. By taking the constants of individual model parameters, it becomes possible to describe the surfaces of specific parts. Consider the possible special models that can be obtained from the general model.

1. Screw surface with profile in the form of an arc of a circle. The screw surface is characterised by the dependence of the angular coordinate of the screw  $z_w$  on the angle of the workpiece rotation  $\theta_w$ , the constancy of the distance  $R_w$  from the centre of the profile to the axis of the workpiece rotation and the radius of the profile of the workpiece  $\rho_w$ . Thus, the radius-vector of the points of the screw surface, based on the general model (1) and the module of the workpiece (2), will be:

$$\bar{r}_w = S_{z_w \theta_w R_w \varphi_w \rho_w}^w \cdot e^{-4}, \quad (4)$$

$$S_{z_w \theta_w R_w \varphi_w \rho_w}^w = M_3(z_w(\theta_w)) M_6(\theta_w) \cdot M_2(R_w) \cdot M_4(\varphi_w) \cdot M_2(\pm \rho_w) \quad (5)$$

The radius of the profile  $\rho_w$  can take a positive and a negative value; a positive value indicates the screw surface of the screw and a negative value indicates the nuts. Model (4) can describe,

for example, the screw surfaces of the screw and the nuts of the ball screws.

2. Rotating surface with variable radius profile on the angle of rotation of the workpiece. Such a surface is characterized by the absence of the angular coordinate of the screw  $z_w$  and the constant distance  $R_w$  from the centre of the profile to the axis of the workpiece rotation. Thus, the radius vector of the points of rotation surface with a variable circular profile, based on the general model (1) and the module of the part (2), will be:

$$\bar{r}_w = S_{\theta_w R_w \varphi_w y_p}^w \cdot e^{-4}, \quad (6)$$

$$S_{\theta_w R_w \varphi_w y_p}^w = M_6(\theta_w) \cdot M_2(R_w) \cdot M_4(\varphi_w) \cdot M_2(y_p) \quad (7)$$

Model (6) can describe, for example, the working surface of pipe rolls for the manufacture of seamless pipes. For such rolls, the parameters of the matrices  $y_p$  and  $\varphi_w$  on the crimp section are functions of the independent parameter  $\theta_w$ . On the calibration section, where the profile becomes constant, they are converted to constants.

3. Concave torus surface. Such a surface is characterized by the absence of the angular coordinate of the screw  $z_w$ , the constancy of the distance  $R_w$  from the centre of the profile to the axis of the workpiece rotation and the radius of the profile of the torus surface  $\rho_w$ . Thus, the radius vector of the points of the rotation body of the concave torus surface, based on the general model (1) and the module of the part (2), will be:

$$\bar{r}_w = S_{\theta_w R_w \varphi_w \rho_w}^w \cdot e^{-4}, \quad (8)$$

$$S_{\theta_w R_w \varphi_w \rho_w}^w = M_6(\theta_w) \cdot M_2(R_w) \cdot M_4(\varphi_w) \cdot M_2(\pm \rho_w) \quad (9)$$

The radius of the profile  $\rho_w$  can take both positive and negative values. A positive value indicates an external concave torus surface and a negative value indicates an internal one. Model (8) can describe, for example, the grooves of the inner and outer bearing rings.

4. Convex torus surface. Such a surface is characterised by the absence of the angular coordinate of the screw  $z_w$ , the constancy of the distance  $R_w$  from the centre of the profile to the axis of the workpiece rotation and the radius of the profile of the torus surface  $\rho_w$ . Thus, the radius vector of the points of the rotation body with a convex torus surface, based on the general model (1) and the module of the part (2), will be:

$$\bar{r}_w = S_{\theta_w R_w \varphi_w \rho_w}^w \cdot e^{-4}, \quad (10)$$

$$S_{\theta_w R_w \varphi_w \rho_w}^w = M_6(\theta_w) \cdot M_2(R_w) \cdot M_4(-\varphi_w) \cdot M_2(-\rho_w) \quad (11)$$

From Fig. 1, we can infer that  $\varphi_w$  and  $\rho_w$  take negative values for the outer convex torus surface. Model (10) may describe, for example, roller saw blades, roll forming rollers, and belt pulleys.

### 3. GENERAL MODEL OF THE NOMINAL SURFACE OF THE TOOL

No matter which model describes the nominal surface of the workpiece, the tool radius vector in modular form is described by the transition matrix based on the workpiece shape.

$$\bar{r}_t = M_{tw} \cdot \bar{r}_w, \quad (12)$$

where  $M_{tw}$  – is the transition matrix from the coordinate system of the workpiece to the coordinate system of the tool. It describes the forming system of a machine tool that is involved in profiling the tool.

The matrix of transition (12) is the product of two spherical modules:

$$M_{tw} = S_{\theta_t y_c}^{\varphi_t} \cdot S_{\psi}^0, \quad (13)$$

where:  $S_{\theta_t y_c}^{\varphi_t}$  – is the module of the shape-building of a tool;  $S_{\psi}^0$  – is the module of the angular orientation of the tool relative to the details.

Shape-building module (13) consists of the product of two matrices:

$$S_{\theta_t y_c}^{\varphi_t} = M_6(\theta_t) \cdot M_2(y_c), \quad (14)$$

where:  $\theta_t$  – is the angle of rotation of the workpiece coordinate system relative to the axis of rotation of the tool;  $y_c$  – is the distance between the axes of rotation of the tool and workpiece.

The module of orientation (13) is presented by the matrix of relative rotations:

$$S_{\psi}^0 = M_5(\psi), \quad (15)$$

where:  $\psi$  – the angle of inclination of the grinding wheel.

The abrasive tool is editing on a constant surface (for example, on the calibration section of a tubular roll of variable radius profile); therefore only one variable parameter is used in module (15) – the angle of inclination of the wheel  $\psi$ .

To profile the tool, it is necessary to make an equation that determines the contact line, as follows:

$$\overline{V}_{tw} \cdot \overline{n}_w = 0, \quad (16)$$

where:  $\overline{n}_w$  – is the unit vector of normal line to the workpiece surface;  $\overline{V}_{tw}$  – is the vector of the velocity of the relative motion of the surface in the coordinate system of the tool.

The normal can be found as a vector product of vectors tangent to the surface. To find the normal, it is necessary to differentiate the radius vector of the workpiece surface by both angular parameters.

During the one-parametric rounding (Kalchenko et al., 2018) relationship between the parameters  $\varphi_w$  and  $\theta_w$  equal to zero of a mixed product of three vectors that are derived of the vector  $\bar{r}_t$ .

$$\left( \frac{\partial \bar{r}_t}{\partial \varphi_w} \times \frac{\partial \bar{r}_t}{\partial \theta_w} \right) \cdot \frac{\partial \bar{r}_t}{\partial \tau_w} = 0, \quad (17)$$

where:  $\left( \frac{\partial \bar{r}_t}{\partial \varphi_w} \times \frac{\partial \bar{r}_t}{\partial \theta_w} \right) = \overline{n}_w$  – is the vector normal to the surface of the workpiece at the point with curvilinear coordinates  $\varphi_w$ ,  $\theta_w$ .  $\frac{\partial \bar{r}_t}{\partial \tau_w} = \overline{V}_w$  – is the vector of velocity of relative motion of the workpiece relative to the wheel;  $\tau_w$  – is the time of moving the workpiece, while turning it at the angle  $\theta_t$  in the opposite motion an axis  $O_t Z_t$  of the wheel.

The velocity of the workpiece regarding the wheel is determined by a matrix of transition from the workpiece coordinate system in the tool coordinate system:

$$\frac{\partial \bar{r}_t}{\partial \tau_w} = \frac{\partial M_6(\theta_t)}{\partial \theta_t} \cdot \frac{\partial \theta_t}{\partial \tau_w} \cdot M_{tw}, \quad (18)$$

where:  $\frac{\partial \theta_t}{\partial \tau_w} = \overline{\omega}_{tw}$  is the angular velocity of the workpiece rotation relative to the axis of the wheel.



We find the scalar product of vectors  $\overline{n_w}$  and  $\overline{V_{tw}}$  by writing down the determinant

$$\overline{V_{tw}} \cdot \overline{n_w} = \begin{vmatrix} X_{V_{tw}} & Y_{V_{tw}} & Z_{V_{tw}} \\ X_{\varphi_w} & Y_{\varphi_w} & Z_{\varphi_w} \\ X_{\theta_w} & Y_{\theta_w} & Z_{\theta_w} \end{vmatrix} = 0, \quad (19)$$

where  $X_{V_{tw}}, Y_{V_{tw}}, Z_{V_{tw}}$  – vector coordinates  $\overline{V_{tw}}$ ;  $X_{\varphi_w}, Y_{\varphi_w}, Z_{\varphi_w}$  – coordinates of the tangent  $\overline{A_w} = \frac{\partial \overline{r_t}}{\partial \varphi_w}$ ;  $X_{\theta_w}, Y_{\theta_w}, Z_{\theta_w}$  – coordinates of the tangent  $\overline{B_w} = \frac{\partial \overline{r_t}}{\partial \theta_w}$ .

The radius vector  $\overline{r_t}$  describes the plurality of tool surfaces. The choice of rational is made on the basis of the analysis of geometrical parameters of the outer surface of the workpiece and the allowance removal  $\delta$ .

#### 4. GENERAL MODEL OF THE REAL SURFACE OF THE TOOL AND WORKPIECE

Having determined the radius vector, we find that it is described by a spherical (torus) module, which is similar to the module of workpiece (1), but with own parameters, as follows:

$$\overline{r_t} = S_{\theta_t \cdot y_t \cdot \varphi_t \cdot y_p}^t \cdot e^{-4}, \quad (20)$$

$$S_{\theta_t \cdot y_t \cdot \varphi_t \cdot y_p}^t = M_6(\theta_t) \cdot M_2(y_t) \cdot M_4(\varphi_t) \cdot M_2(y_p) \quad (21)$$

where:  $\overline{r_t}$  – is the radius vector of the tool surface points;  $S_{\theta_t \cdot y_t \cdot \varphi_t \cdot y_p}^t$  – is the spherical module, that is a matrix of transition from the starting point to the coordinate system of the tool;  $\theta_t$  – is the angle of turning around the axis  $O_i Z_i$  of rotation of the tool;  $y_t = R_t$  – is the distance from the center of the profile of the tool to its axis of rotation;  $\varphi_t$  – is angle of rotation around the axis  $O_i Y_i$ ;  $y_p = \rho_t$  – is the radius wheel profile.

Creating a three-dimensional surface of the wheel is a very common way of learning the shaping processes (Uhlmann et al., 2016; Yan et al., 2011; Yanlong et al., 2013). Modelling in the MathCAD system allowed the determination of the maximum angle of the circle during processing (Fig. 2). Modelling was performed for the case of processing of constant trough profile  $Dw = 2Rw = 80$  mm, radius profile  $\rho_w = 20$  mm and central angle  $\xi = 140^\circ$ . Circle parameters: diameter 150 mm, height of circle 20 mm and ligament ceramic. As a result of the simulation, it was determined that for the selected conditions the contact line exists at  $\psi_t < 22^\circ$ . When the circle is tilted at  $22^\circ$ , the contact line disappears and contact occurs at the edges of the profile.

Thus, three spherical modules describe the radius vector of the workpiece surface:

$$\overline{r_{wt}} = S_{z_w \theta_w y}^\varphi \cdot S_{\varphi_t \psi_t x_t}^o \cdot \overline{r_t}, \quad (22)$$

where:  $S_{z_w \theta_w y}^\varphi = M_3(z_w) \cdot M_6(\theta_w) \cdot M_2(y_c + a \cdot \theta_w - \delta)$  – is the shaping module of details;  $\theta_w$  – is the angle of rotation coordinate system of the tool around the axis of rotation of the workpiece;  $y = y_c + a \cdot \theta_w - \delta$  – the current coordinate interaxial distance of the tool and workpieces;  $y_c$  – the distance between the axis of the wheel and the workpiece in the position of the residual molding of the workpiece surface;  $a = \frac{t}{2\pi}$  – is the constant of Archimedean spiral, which moves in relative motion wheel when removing of the allowance  $\delta$ ;  $S_{\varphi_t \psi_t x_t}^o = M_4(\varphi_t) \cdot$

$M_5(\pm \psi_t) \cdot M_1(x_t)$  – is the module of the angular orientation of the tool relative to the workpiece.

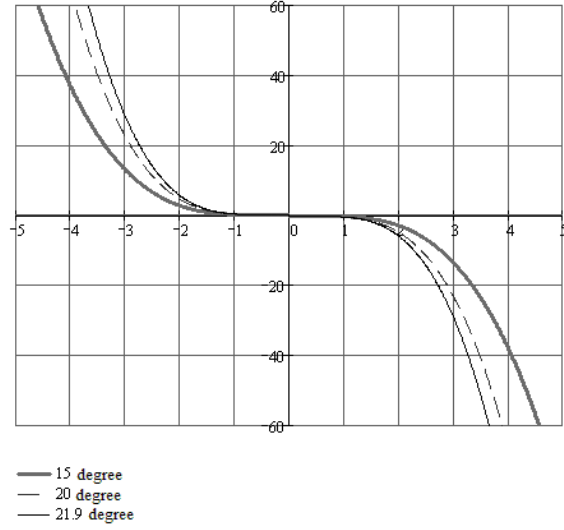


Fig. 2. The contact line of the wheel and the workpiece at different angles of a wheel

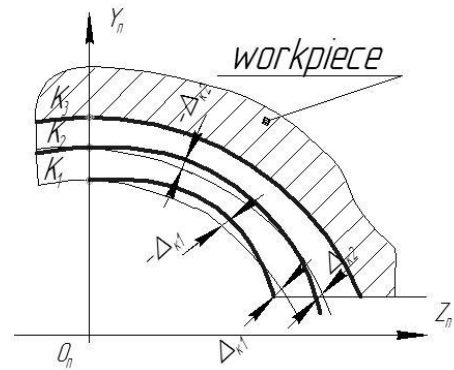


Fig. 3. The process of removing the allowance

When the allowance is removed,  $\delta = 0$  and  $y = y_c$ , the contact line which is rotating about the axis of the workpiece without

lateral movement describes the shape of the machined surface with radius  $\rho_w$ . Fig. 3 shows the allowance removal process. When inserting a wheel into the workpiece, we observe that at the same time its inclination will appear as errors ( $\Delta_{kj}$ , the value of which will decrease during the removal of the allowance. The final profile will be forming without error, since the wheel is straightening at the maximum angle of inclination at which the formation process is taking place. In this case, the radius of projection of the contact line of the wheel and the part on the axial plane will be equal to the radius of the groove profile  $\rho_w$ . The magnitude of the errors ( $\Delta_{kj}$  is determined by the least squares method and should not exceed the tolerances on the shape of the groove profile.

Model (22) describes a plurality of surfaces. To determine the real surface of the workpiece, it is necessary to make an equation describing the contact line.

$$\overline{V_{wt}} \cdot \overline{n_t} = 0, \quad (23)$$

where:  $\overline{n}_t$  – is the unit vector of normal line to the tool surface;  
 $\overline{V}_{wt}$  – is the vector of the velocity of the relative motion of the  
 surface in the coordinate system of the workpiece.

By rotating the contact line around the axis of the workpiece with axial displacement  $z_w$ , we get a real contour of the workpiece surface.

## 5. GRINDING PROCESS WITH CROSSED AXES OF THE TOOL AND WORKPIECE

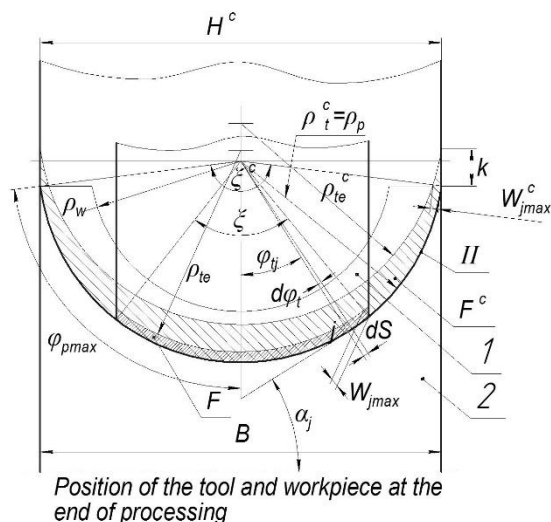
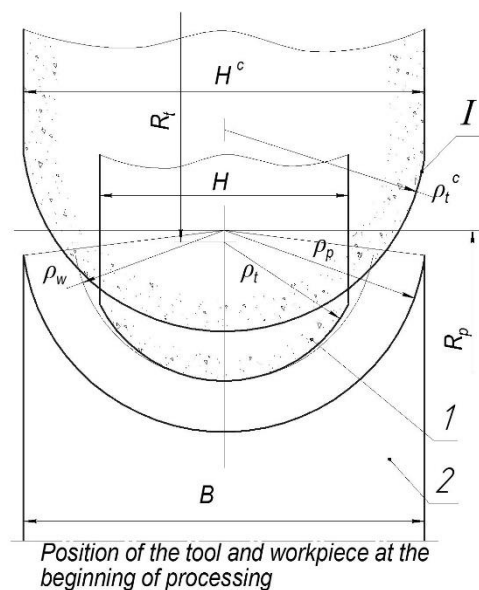
The method of processing workpiece with a profile in the form of an arc of a circle by the method of copying involves grinding by abrasive wheel, the height of which  $H^c$  is equal to the width  $B$  of the treated surface (Fig. 4). In this case, the radius of the wheel profile  $\rho_\xi^c$  is equal to the radius of the part profile  $\rho_p$  and, accordingly, greater than the radius of the workpiece profile  $\rho_w$ . When machining in this way, we removed just the variable allowance, because at the beginning of machining (pos. I) the wheel is cut by side sections of the profile and only at the end of machining (pos. II) the central point of the tool profile enters into the cutting process. At this time, the side sections of the wheel profile are not removed from the allowance, but create additional friction and increase the temperature in the cutting zone.

Grinding with the crossed axes of the tool and workpiece involves machining a narrow wheel, the height of which  $H$  is less than the width  $B$  of the work surface. The radius of the wheel profile  $\rho_t$  in the initial position is less than the radius of the part  $\rho_p$  and the radius of the workpiece profile  $\rho_w$ . The wheel is correction in an inclined position, the angle of inclination of which  $\psi_t$  corresponds to the maximum inclination of the wheel during processing, thereby achieving the equality of the radius of the contact line projection in the axial plane and the radius of the profile of the part  $\rho_p$ .

All parameters in figure 4 with index  $c$  – refer to the copy method. Parameters without index – the method of grinding with crossed axes.  $\rho_{te}$  and  $\rho_{te}^c$  – tool profile after editing for appropriate grinding methods.

One of the advantages of this method of processing over the traditional method of copying is the more efficient use of tool abrasives. In the traditional processing, the wear of the side part of the wheel by the value of  $k$  leads to the removal of a large part of the abrasive material  $F^c$  (Fig. 4). Since the centre angle of the tool profile in the proposed method is much less than the angle  $\xi^c$

in traditional method, the volume of abrasive  $F$  removed when editing a narrow wheel is much smaller (Fig. 4).



**Fig. 4. Tool wear during machining**

To restore the original shape of a circle in radius  $\rho_i^E$ , it is necessary to cut it in the direction perpendicular to the axis of rotation, by the value of  $k^C$ , which can be found from the relation (Kalchenko et al., 2020):

$$k^c = -(\rho_t^c - W_j) \cdot \sin \alpha_j + \sqrt{(\rho_t^c - W_j)^2 \cdot \sin^2 \alpha_j - W_j^2 + 2 \cdot \rho_t^c \cdot W_j} \quad (24)$$

The maximum wear  $W_{jmax}$  occurs at the  $j$ -th point of the wheel profile where  $\alpha_j = \varphi_{pmax}$ , on the side parts of the wheel profile. This causes frequent editing of the abrasive wheel with the removal of the abrasive array  $F^c$ . For example, with limited wear  $W_{jmax} = 0.05$  mm, it is necessary to cut a 3.16 mm of the wheel at the center point of the profile (Kalchenko et al., 2020). When editing a narrow wheel, it is necessary to remove the array  $F$ , which is much smaller.

To determine the limited wear of  $W_{jmax}$  for a narrow wheel, it is necessary to determine the performance of the grinding pro-

cess. The ways to solve of boundary-value problem discussed in detail in the works (Mikhailets V. 2015, 2018). The general model of removal of allowance and formation  $Q$  for machining surface of a workpiece with a circular profile, given in the form of a spherical module, has the form (Kalchenko et al., 2020):

$$Q = \int_0^T \left( \int_{-\varphi_{tmax}}^{+\varphi_{tmax}} \left( \int_{\theta_{1kj}}^{\theta_{2kj}} (\overline{V}_j \cdot \overline{n}_j - y_{sc}) \cdot (R_t + (\rho_t - W_j) \cdot \cos \varphi_{tj} \cdot d\theta_k) \cdot \sqrt{\left( \frac{dR_{\varphi_{tj}}}{dj} \right)^2 + \left( \frac{d\varphi_{tj}}{dj} \right)^2} \cdot d\varphi_t \right) \cdot dT \quad (25)$$

where  $T$  – is the contact time of the part with the wheel;  $\pm \varphi_{tmax}$  – limit values of the angular position  $\varphi_{tj}$  of point  $j$  on the wheel profile;  $\theta_{1kj}$ ,  $\theta_{2kj}$  are the angular coordinates of a contact spot on a radius  $R_t + (\rho_t - W_j) \cdot \cos \varphi_{tj}$  (Fig.4);  $\overline{V}_j$ ,  $\overline{n}_j$  – vectors of cutting speed and normal at  $j$ -th point of a wheel;  $y_{sc} = f(\varphi_{tj}, K_{sc})$  – compliance of the processed system;  $K_{sc}$  – the value of static compliance;  $R_t$  – is the distance from the axis of rotation of the wheel to the center of its profile with radius  $\rho_t$ ;  $R_{\varphi_{tj}} = R_t + \rho_t \cdot \cos \varphi_{tj}$  – is the radius of rotation of the  $j$ -th point.

When moving from one cutting edge to an elementary part of the wheel  $dS$ , it is necessary to take into account the heterogeneity of the surface of the abrasive tool. It is possible to take into account the discontinuity of the surface of the wheel using the coefficient (Kalchenko et al., 2018):

$$\left[ 1 - \exp \left( - \frac{\sum_{i=1}^m b_i(t, \theta)}{b_0} \right) \right].$$

Model (25) describes the grinding performance for a single workpiece. To determine performance when processing a batch of workpieces  $Q$  must be multiplied at the number of workpieces in the batch.

The general 3D model (25) of the allowance removal and the formation makes it possible to determine the local productivity  $Q_l$  at each elementary section  $dS$  (Fig. 4) of the contact spot  $S$  of wheel 1 and workpiece 2. In model (25)  $R_t + (\rho_t - W_j) \cdot \cos \varphi_{tj} \cdot d\theta_k$  – the length of the elementary section is measured along the arc of a circle with radius  $R_t + (\rho_t - W_j) \cdot \cos \varphi_{tj}$ . The width of the elementary section in the axial section of the

circle is determined by the differential  $\sqrt{\left( \frac{dR_{\varphi_{tj}}}{dj} \right)^2 + \left( \frac{d\varphi_{tj}}{dj} \right)^2}$ .

The specific productivity  $Q_{sj}$  is determined by the internal integral of the model (25). It shows how much metal is cut by a wheel within the  $j$ -th point of the profile.

The instantaneous grinding performance  $Q_i$  is described by the surface integral of model (25). It allows the determination of the instantaneous volume of metal that cuts into the contact spot of the wheel and the workpiece.

The average grinding performance  $Q_a$  is determined by the ratio:

$Q_a$  is determined by the ratio:

$$Q_a = \frac{Q \cdot n}{t} \quad (26)$$

where  $Q \cdot n$  – is the volume of metal removed from  $n$  parts over time  $t$ .

The analysis of model (25) shows that when  $\overline{V}_j \cdot \overline{n}_j > 0$  the allowance is removed from the workpiece. This takes place when  $\overline{V}_j \cdot \overline{n}_j = 0$  metal is not cutting and we have the process of form-

ing the surface of the workpiece  $\overline{r}_{pi}$ . Productivity increases with the increase of scalar product vectors  $\overline{V}_j \cdot \overline{n}_j$  and the rigidity of the machined system, the contact area  $S$  of the wheel and the details of the processing coordinate, the angle  $\psi_t$  and the decrease in the wear profile  $W_j$  of the wheel (Mamalis et al., 2016; Grabchenko et al., 2014; Shakhbazov et al., 2019).

The amount of worn abrasive per unit time is calculated for the section of the wheel profile  $dS$  from equation (Mamalis et al., 2016; Grabchenko et al., 2014)

$$Q_a = k_a \cdot 2\pi \cdot (R_t + \rho_t \cdot \cos \varphi_{tj}) \cdot J_j, \quad (27)$$

where  $J_j$  – abrasive wear at a certain grinding speed in the direction normal to the tool profile per unit time;  $k_a$  – is the coefficient that takes into account the overlapping of the cutting edges.

The value of the elemental wear rate of a circle  $J_j$  over time  $dt$  has the form

$$J_j = \frac{C_{sj} \cdot Q_{sj}^{m_j} + C_{dj} \cdot Q_{dj}^{b_j}}{k_a \cdot 2\pi \cdot R_{\varphi_{tj}}} \quad (28)$$

where  $C_{sj}$ ,  $C_{dj}$  – are the coefficients of specific wear at the  $j$ -th point of the wheel profile at  $Q_{sj} = 1$  and  $Q_{dj} = 1$ , which are determined experimentally for each  $j$ -th point of the wheel profile;  $Q_{sj}$  – the specific volume of the metal being removed by the  $j$ -th point of the wheel profile, determined from the expression (25) at  $\overline{V}_j \cdot \overline{n}_j \cdot \tau_j \geq a_{zmin}$ ;  $\tau_j$  – the time between the contacts of the cutting grains;  $a_{zmin}$  – the minimum thickness of the layer which cut off by the cutting edge;  $Q_{dj}$  – the specific volume of metal deformed by abrasive grains of the  $j$ -th point of the wheel profile, determined from expression (25) at  $\overline{V}_j \cdot \overline{n}_j \cdot \tau_j \leq a_{zmin}$ ;  $m_j$  – the coefficient that takes into account the intensity of the grinding mode and the state of the cutting surface of the wheel; and  $b_j$  – the coefficient that takes into account the intensity of the deformation mode of the metal without its removal.

The linear wear of  $W_j$  at the  $j$ -th point of the wheel profile during the machining process is determined by the equation (Mamalis et al., 2016; Grabchenko et al., 2014)

$$W_j = \int_{T_0}^{T_0} \frac{C_{sj} \cdot Q_{sj}^{m_j} + C_{dj} \cdot Q_{dj}^{b_j}}{k_a \cdot 2\pi \cdot (R_t + \rho_t \cdot \cos \varphi_{tj})} dT_0 \quad (29)$$

where  $T_0$  – is the processing time of the workpiece for part of its rotation, one revolution or the number of revolutions required to process the workpiece by a section of a wheel within the  $j$ -th point of its profile.

## 6. CONCLUSIONS

The general model was developed and on its basis special models of process of grinding with the crossed axes of the tool and workpiece with a profile in the form of a circle arc were formulated.

A new method of control of the grinding process is proposed, which will provide processing by equidistant curves, and the value of cutting of a wheel equal to the allowance. This will increase the productivity and quality of grinding. Based on the developed method, it is necessary to develop a package of applications that would allow programming of CNC machine tools by programmers

who do not have special training.

The presented method of grinding implements the processing with the spatial contact line of the tool and workpiece. When the axes are crossed, the contact line is stretched, which leads to an increase of the contact area and, accordingly, to decrease of the temperature in the processing area. This allows processing of the workpiece with more efficient cutting modes. The developed mathematical models are the basis for experimental research.

## REFERENCES

1. **Anderson D., Warkentin A., Bauer R.** (2011), Experimental and numerical investigations of single abrasive-grain cutting, *International Journal of Machine Tools & Manufacture*, 51, 898-910.
2. **Chi Y., Li H.** (2012), Simulation and analysis of grinding wheel based on Gaussian mixture model, *Frontiers of Mechanical Engineering*, 7(4), 427-432.
3. **Cong S., Yansheng D., Dongxue L., Shichao X.** (2018), Modeling and predicting ground surface topography on grinding chatter, *Procedia CIRP*, 71, 364-369.
4. **Grabchenko A., Fedorovich V., Pyzhov I., Kunderák J.** (2014), 3D simulation of vibrating diamond grinding. *Manufacturing Technology*, 14(2), p. 153-160.
5. **Kacalak W., Lipiński D., Szafraniec F., Tandecka K.** (2018), The methodology of the grinding wheel active surface evaluation in the aspect of their machining potential, *Mechanik*, 91 (8-9), 690-697.
6. **Kacalak W., Szafraniec F., Lipiński D.** (2018), Methods for modeling the active surface of grinding wheels, *Mechanik*, 91 (10), 907-914.
7. **Kalchenko V., Kalchenko V., Sira N., Yeroshenko A., Kalchenko D.** (2020) Three-Dimensional Simulation of Machined, Tool Surfaces and Shaping Process with Two-Side Grinding of Cylindrical Parts Ends. In: Tonkonogiy V. et al. (eds) *Advanced Manufacturing Processes. InterPartner 2019. Lecture Notes in Mechanical Engineering*. Springer, Cham, 2020, p. 118-127.
8. **Kalchenko V., Yeroshenko A., Boyko S.** (2018), Crossing axes of work-piece and tool at grind-ing of the circular trough with variable profile, *Acta Mechanica et Automatica*, 12(4), 281-285.
9. **Kalpana K., Arunachalam N.** (2018), Grinding wheel redress life estimation using force and surface texture analysis. *Procedia CIRP*, 72, 1439-1444.
10. **Mamalis A.G., Grabchenko A.I., Fedorovich V.A., Romashov D.V.** (2016), Improving the design of diamond wheel for high-speed grinding. *Journal of Machining and Forming Technologies*. Nova Science Publishers, Inc. Volume 8, Number 1-2, 12 p.
11. **Mikhailiets V.A., Chekhanova G.A.** (2015), Limit theorems for general one-dimensional boundary-value problems. *Journal of Mathematical Sciences*, Vol. 204, No. 3, p. 333-342.
12. **Mikhailiets V.A., Pelekhat O.B.** (2018), Limit theorems for the solutions of boundary-value problems. *Ukrainian Mathematical Journal*, Vol. 70, p. 216-223.
13. **Shakhbazov Y., Shyrokov V., Fedorovych V.** (2019), Specifying the Process Parameters for Diamond Dressing of Grinding Wheels. *Journal of Superhard Materials*, Volume 41, p. 272-277.
14. **Uhlmann E., Koprowski S., Weingaertner W.L., Rolon D.A.** (2016), Modelling and Simulation of Grinding Processes with Mounted Points: Part II of II - Fast Modelling Method for Workpiece Surface Prediction. *Procedia CIRP*, 46, 603-606.
15. **Yan L., Rong Y.M., Jiang F., Zhou Z.X.** (2011), Three-dimension surface characterization of grinding wheel using white light interferometer. *International Journal of Advanced Manufacturing Technology*, 55, 133-141.
16. **Yanlong C., Jiayan G., Bo L., Xiaolong C., Jiangxin Y., Chunbiao G.** (2013), Modeling and simulation of grinding surface topography considering wheel vibration. *The International Journal of Advanced Manufacturing Technology*, 66(5-8), 937-945.

# AN EXPERIMENTAL STUDY OF THE VIBRATIONAL CHARACTERISTICS OF A DIAMOND CIRCULAR BLADE USING ELECTRONIC SPECKLE-PATTERN INTERFEROMETRY AND FEM

Mykhaylo TKACH\*, Yurii HALYNKIN\*, Arkadii PROSKURIN\*, Irina ZHUK\*\*, Volodymyr KLUCHNYK\*, Igor BOBYLEV\*

\* Department of Engineering Mechanics and Technology of Marine Engineering, Engineering and Research Institute of Engineering, Admiral Makarov National University of Shipbuilding, Mykolaiv, 9 Heroes of Ukraine Avenue, Ukraine

\*\*Department of Automation and Computer-Integrated Technologies, Faculty of Computer Science, Petro Mohyla Black Sea National University, Mykolaiv, street 68 Desantnikov 10, Ukraine

[mykhaylo.tkach@nuos.edu.ua](mailto:mykhaylo.tkach@nuos.edu.ua), [yurii.galynkin@nuos.edu.ua](mailto:yurii.galynkin@nuos.edu.ua), [arkadii.proskurin@nuos.edu.ua](mailto:arkadii.proskurin@nuos.edu.ua), [iryna.zhuk@chmnu.edu.ua](mailto:iryna.zhuk@chmnu.edu.ua),  
[vladimir.kluchnyk@gmail.com](mailto:vladimir.kluchnyk@gmail.com), [igor.bobylev.nuk@gmail.com](mailto:igor.bobylev.nuk@gmail.com)

received 13 March 2020, revised 10 March 2021, accepted 13 March 2021

**Abstract:** The compact installation and technology for determining vibration characteristics by the ESPI method has been created. The experimental determination of the dynamic characteristics of a diamond circular blade with a diameter of 203.4 mm and a thickness of 1.19 mm using real-time electronic speckle interferometry is presented. 15 mode shapes of vibration were detected in the range from 100 to 5000 Hz. The program calculation of the natural frequencies and mode shapes is carried out for three values of the clamping inner diameter (42 mm, 44 mm, 46 mm). The options for calculating a disk with a rim and without a rim are considered. It is shown that the minimum mean squared error of the calculation is achieved for the values of the diameter of the disk 46 mm, 42 mm and 44 mm for the number of nodal circles 0, 1 and 2, respectively. To verify the accuracy of the interferometer, experimental, computational and analytical studies of console steel rod 200 x 22.25 x 3.78 mm in size were carried out.

**Key words:** interferometry, speckle pattern, correlation fringes, vibrational analysis

## 1. INTRODUCTION

Modern engineering is characterized by an increase in the specific capacities of machines and devices. During operation, cutting wheels and circular saws rotate at high frequencies and are subject to significant dynamic loads. The resulting resonant vibration significantly increases the loads on them and on the bearings. This is one of the main reasons for the breakdown of such a tool. Also, the roughness of the processed surface increases and the service life of the equipment decreases.

The solution to the problems of the strength of parts under dynamic loads is one of the most complex and time-consuming. These conditions determine the relevance of studies of vibrational characteristics of disk structural elements both at the stage of design and development of products, and in the analysis of emergency situations.

The creation of structures operating under vibrational loads and the implementation of measures for detuning from resonance involves, first of all, determining the spectrum of resonant frequencies and vibration mode shapes. Moreover, the results of the study of the dynamic parameters of a homogeneous disk clamped in the center (on the shaft) are of independent importance and can serve as a reference point in the study of oscillations of the disks of turbomachines (Levin, 1953).

Determination of natural frequencies and vibration modes of solids can be carried out by a theoretical, experimental or theoretical-experimental method. The first practical method for visualizing vibration modes on plates and, therefore, for conducting an exper-

imental analysis of vibration, was invented by Chladni in the 1780s (Chladni and Beyer, 2015). The method includes spraying a fine powder, such as sand, onto the surface of the plate, so it is not a non-contact method. In the book Wailer (1961), studies of round, elliptical, rectangular and other polygonal plates are presented, as well as practical and historical notes. The results include extensive graphical tables of observed mode forms, a method for classifying mode forms, and a discussion of how these forms arise. The ESPI method was used to experimentally test analytical and numerical models of applied mechanics in Halama et al., (2016), vibration theory in Chi-Hung et al., (2004), in the automotive industry by Beeck and Hentschel (2000) as well as Van der Auweraer et al., (2002), materials science in Richardson et al., (1998), biomedical field by Yang et al., (2014), microelectromechanical systems in an article by Foitzik et al., (2003) and in many other areas of science and technology. A detailed study of the frequencies and modes of vibrations of a solid homogeneous disk fixed in the center was carried out by Makaeva et al., (2008a), (2008b). Experimental studies were carried out by the method of holographic interferometry (Makaeva et al. 2008a).

The Rayleigh – Ritz method provides numerical determination of approximate values of frequencies and natural forms of resonant vibrations (Babakov, 1965). Therefore, in engineering practice, the theoretical calculation of the resonant parameters of structures is mainly performed numerically by the finite element method (Mrozek et al. 2018), implemented in modern software systems ANSYS, NASTRAN, COSMOS, FEMAP, etc.

But the errors in modelling the boundary conditions, the mis-

match of the calculation model with the object of study reduce the reliability of the calculated data and almost always require their experimental verification.

To study the vibration characteristics of the disk, the method of electronic speckle-pattern interferometry was used. With a good quality of interferograms, it ensures the automation of experimental research reduces the requirements for vibration isolation of stands and eliminates the need for photochemical processing.

In addition, a highly accurate experimental determination of vibration parameters is crucial for the implementation of the combined calculation and experimental method, when the experimental data are used to form boundary conditions, and the numerical method is used for a detailed analysis of the distribution of amplitudes, deformations, and stresses in the entire volume of the studied object. It allows to increase the accuracy and reduce the complexity of determining the dynamic parameters of disk-shaped parts of machines and mechanisms (Careva and Tupoleva, 2006).

Therefore, this work devoted to the creation of an experimental stand and the conduct of a comprehensive experimental and numerical study of the natural frequencies and modes of vibration clamped in the center of the disk is relevant.

## 2. THEORETICAL PART

### 2.1. Description of the interferometric stand

In experimental mechanics, non-contact optical methods are used to study the vibrations of solids, which use the coherent properties of laser radiation.

The most informative is the method of holographic interferometry (HI) (Vest, 1982). It makes it possible in real time to visualize the dislocation of nodal lines i.e. determine the mode shapes and the value of the resonant frequency. The resolution of holographic interferograms makes it possible to estimate with high accuracy the distribution of vibration amplitudes over the surface of an object. But the technique for obtaining holographic interferograms is rather complicated, involves the use of photographic plates with the need for their accurate positioning and photochemical processing, good vibration protection of the optical stand and highly coherent laser radiation. Almost the same completeness of information about the vibrational process, but lower resolution of interference fringes, has the electron speckle-pattern interferometry (ESPI) method (Jones and Wykes, 1989).

With less stringent requirements for the experimental technique and less laboriousness, it allows you to quickly determine the resonant frequency and observe the form of vibrations on a computer screen in real time without using the photochemical process. It is indispensable in the case of serial control of products, if necessary, an express analysis. This determined our choice of research method.

The contrast of the bands on speckle interferograms obtained using an interferometer with a speckle-modulated reference wave is, other things being equal, lower than on interferograms with a smooth reference wave (Yelenevsky and Shaposhnikov, 2001) (Zhuzhukin, 2011). But the optical design of such an interferometer is rather cumbersome, extremely difficult to align and requires periodic monitoring due to its low resistance to external disturbances. In this work, an extremely simple optical scheme of a digital speckle interferometer with combined beams was proposed, which has increased noise immunity. But the use of a large-sized transmitting diffuser with precision movement, which is

larger than the object of study in size, does not allow creating a compact portable device (Zhuzhukin, 2011).

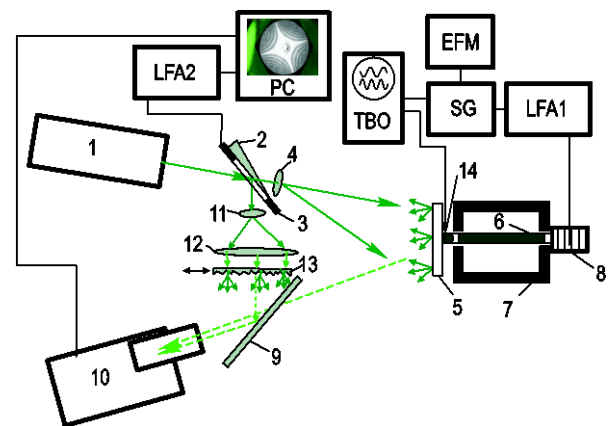


Fig. 1. Optical design and hardware of the ESPI stand: 1 - laser, 2 - optical wedge, 3 - piezoceramic ring, 4,11 - micro lens, 5 - test disk, 6 - mounting pin, 7 - clamp case, 8 - piezoceramic vibrator, 9 - beam splitter, 10 - video camera, 12 - collecting lens, 13 - diffuser, 14 - bimorph vibration sensor, SG - sound generator, TBO - two-beam oscilloscope, EFM - electronic frequency meter, PC - personal computer, LFA 1, LFA 2 - low frequency amplifiers

In our studies, we used an interferometer with a diffuse reference wave and separated branches. Such a compromise solution made it possible to create a mobile compact electronic speckle-pattern interferometer with satisfactory noise immunity, sufficient to conduct vibration diagnostics of products outside the bench environment (Petrov and Lau, 1995).

The optical design and hardware of the created digital signal center are presented in Fig. 1. A coherent light source is a solid-state DPSS laser 1 with a radiation power of 50 mW and a wavelength of  $\lambda = 0.532 \mu\text{m}$ . The laser beam by an optical wedge 2 is divided into transmitted and reflected, forming channels of the subject and reference beams. The transmitted beam is expanded by a micro lens 4, scattered by the matte surface of the investigated disk 5, and creates a diffuse object wave. Passing through the beam splitter 9, it is focused by the lens of the video camera 10 on the plane of the charge-coupled device (CCD) as an object speckle field.

The beam reflected from the beamsplitting wedge is expanded by the micro-lens 11, collimated by the lens 12 and scattered by the transmitting diffuser 13, forming a diffuse reference wave. On the beam splitter 9, it is combined with the subject and, after refraction in the camera lens, forms a speckle reference field on the matrix surface (Mihaylova et al. 2004), (Mihaylova et al. 2006). The contrast of the resulting speckle pattern will be maximum at the same average intensities and consistent polarizations of the interfering beams. To avoid depolarization of radiation, the diffuser 13 is thin surface etched (Vest, 1982), and aluminum powder is used to paint the disk. The intensity equalization is carried out by changing the intensity of the reference wave when moving the lens 12.

Due to the compact arrangement of the interferometer, the optical path lengths of the reference and subject speckles differ by an order of magnitude. The mismatch in the curvature of the interfering wave fronts leads to a certain decrease in the amplitude of the useful signal (Gorbatenko et al. 2001). But the operating experience of the installation showed that a noticeable deterioration in the quality of the interferogram is not observed.



Video camera 10 operates in the webcam mode and real-time transmits a video stream of 25 frames per second to a computer with a resolution of 720x576 pixels with a brightness division into 256 gradations. To match the spatial frequency of the resulting speckles with the resolution of the CCD matrix, aperture the lens aperture to the value  $F = 16 \dots 22$ . At the same time, the frame registration time  $\tau$  was in the range 0.01 - 0.02 s. A detailed description of the methods for obtaining and processing holographic information is given by the authors in (Tkach et al. 2020), (Tkach et al. 2021).

In this work, we used a diamond circular blade 5 (Fig. 2) with a diameter of  $203.4 \pm 0.05$  mm and a thickness of  $1.19 \pm 0.05$  mm; in addition, there is a rim with a width of  $5 \pm 0.05$  mm and an outer edge of the diamond circular blade  $1.57 \pm 0.05$  mm thick. The diamond circular blade is clamped using two faceplates with a diameter of 46 mm mounted on a threaded rod 6 with a diameter of 27 mm, which is an analog of the shaft. To simulate the operational boundary conditions for mounting the shaft, the pin is clamped at two points in the massive casing 7 (Fig. 3) with an internal cavity. The second end of the stud abuts against the pusher of the piezoceramic vibro-column 8, to which a sinusoidal signal of the sound generator (SG) is fed, previously amplified by the amplifier LFA 1. The elastic wave from the vibrator is transmitted to the stud and excites vibration of the disk under study. Such a wave excitation method eliminates the influence of the attached mass of the vibrator on the disk vibrations.

generator signal is compared with the vibration sensor signal by a two-beam TBO oscilloscope.

## 2.2. ESPI method basics

Electronic speckle interferometry refers to non-contact laser measuring instruments and, like holographic interferometry, allows for resonant vibration of a part to determine the dislocation of nodal lines along its entire surface (Levin, 1953). The experimental technique and the method for producing interferograms are described in more detail in the original sources: (Mrozek et al. 2018); (Jones and Wykes, 1989); (Yelenevsky and Shaposhnikov, 2001); (Zhuzhukin and Solyannikov, 2014); (Komarov, 2004); (Bystrov and Zhuzhukin, 2017); (Tkach et al. 2012); (Tkach et al. 2015).

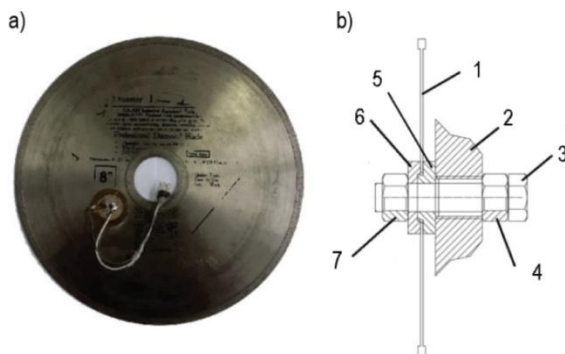
When performing these studies, the method for determining the resonance frequencies of a disk by speckle interferometry is to place the disk in a clamping device, excite oscillations of the disk at resonant frequencies, register the speckle interferogram in real time, by analyzing the signal from the camera, and determine vibrating speckles based on this information (Babakov, 1965).

This allows you to fundamentally reduce the time of research of the dynamic parameters of the object and improve the visualization and image of the waveform using computer processing.

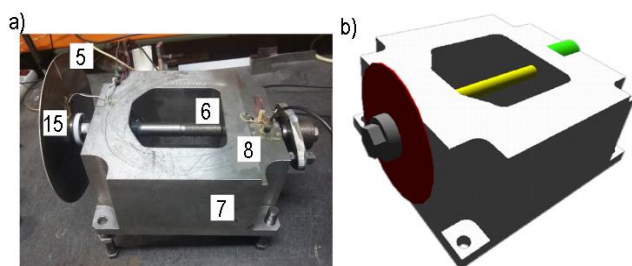
## 3. EXPERIMENTAL PART

### 3.1. Experimental determination of natural frequencies and mode shapes of a diamond circular blade

The resonant frequencies and the corresponding lateral vibrations of the diamond circular blade were obtained using the laboratory bench described in Section 2.1. The thickness of the diamond circular blade with a diameter of  $203.4 \pm 0.05$  mm was measured at twenty different points (Fig. 4). The measurement results are shown in Tab. 1. According to these measurements, the average circle thickness was calculated, which amounted to  $1.19 \pm 0.05$  mm, as well as the average rim thickness of  $1.57 \pm 0.05$  mm. In the experiment, the circle was clamped using two faceplates.

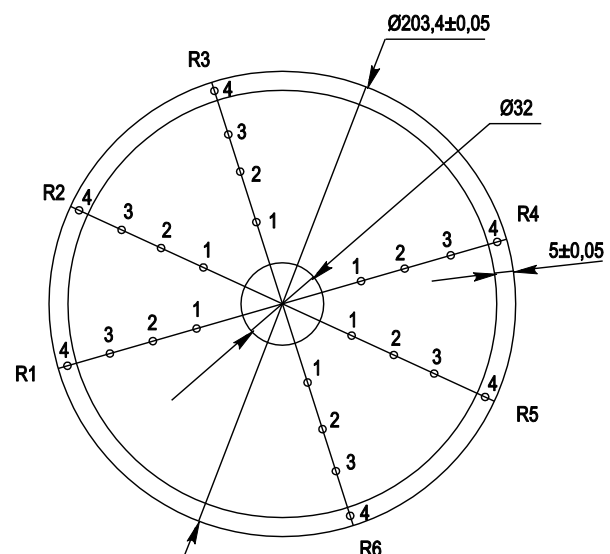


**Fig. 2.** a) Test diamond circular blade, b) Drawing of the diamond circular blade in the fixture. 1 - diamond circular blade, 2 - clamping case, 3 - threaded rod, 4, 7 - bolts, 5, 6 - pressure washer



**Fig. 3.** a) Test drive clamping pattern, b) 3D Test drive clamping model: the disc is highlighted in red, the stud is yellow, the ceramic piezo washers are green

The frequency multiplicity of the disk oscillation frequency relative to the frequency of the SG signal was controlled using a small-sized bimorph vibration sensor 15 glued to the disk at the pinch boundary. The frequency of the vibration excitation signal is measured by the electronic frequency counter of the EFM, and the



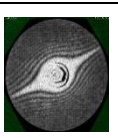
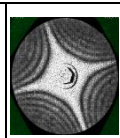
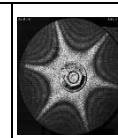
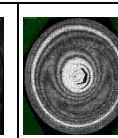
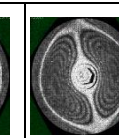
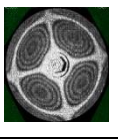

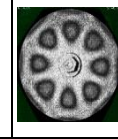
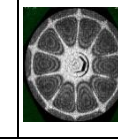
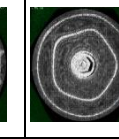

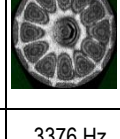



**Fig. 4.** Diamond circular blade measurement circuit

Tab. 1. Diamond circular blade thickness measurement results

Diameter (mm)	Point	R1	R2	R3	R4	R5	R6
50	1	1.22	1.21	1.22	1.19	1.22	1.22
100	2	1.16	1.17	1.16	1.16	1.17	1.16
150	3	1.20	1.18	1.17	1.21	1.21	1.22
200	4	1.59	1.57	1.56	1.54	1.59	1.56

A number of characteristic forms of vibrations obtained as a result of the experiment are presented in Tab. 2 and Fig. 5.

Tab. 2. Experimental mode shapes and natural frequencies of a diamond circular blade

				
153 Hz	200 Hz	377 Hz	944 Hz	980 Hz
				
1184 Hz	1543 Hz	2049 Hz	2669 Hz	2851 Hz
				
3026 Hz	3376 Hz	3471 Hz	4120 Hz	4932 Hz

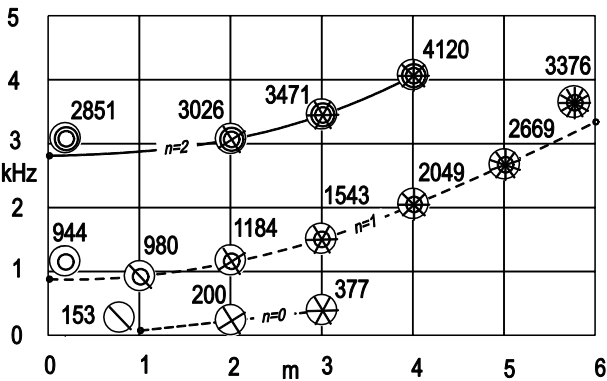


Fig. 5. Experimental values of the natural frequencies of the diamond circular blade;  $n$  - the number of nodal circles,  $m$  - the number of nodal diameters

In addition, we revealed mode shapes (Fig. 6), similar to those found in the work of E. Chladni Treatise on Acoustics (Chladni and Beyer, 2015) under number 109b.

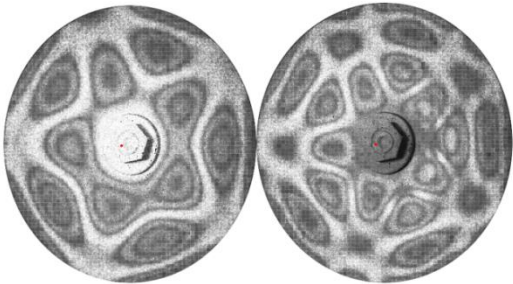


Fig. 6. Mode shapes similar to form 109b (Chladni and Beyer, 2015)

### 3.2. Calculation of natural frequencies and mode shapes of a diamond circular blade by the finite element method

Using the ANSYS Workbench software, we obtained resonant frequencies and the corresponding lateral vibrations of the circular blade. For this, a 3D model of a circular blade was created, the measurements of which are described in section 3.1. The boundary conditions in the calculation were: the disk was clamped along the inner diameter and free at its outer diameter. This corresponds to the fastening of the disk on the experimental stand in Fig. 2 (b).

For the calculation, a SOLID 186 finite element (tetrahedron) with a size of 0.595 mm was used. The total number of elements was about 400 thousand as shown in Fig. 7. Calculations performed with a twofold decrease in the size of the finite element did not reveal a significant change in the frequencies and vibration modes of the disk under study.

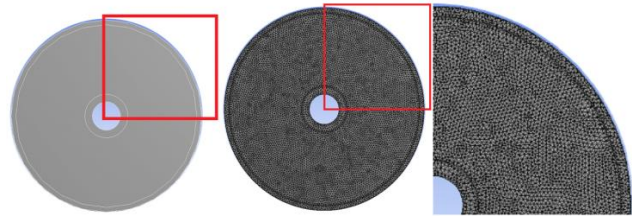
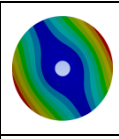
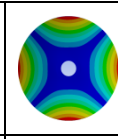
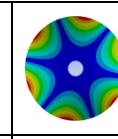
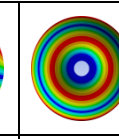
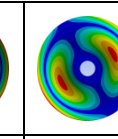
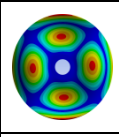
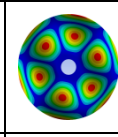
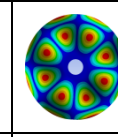
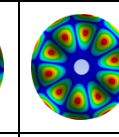
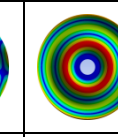
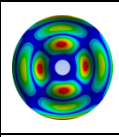
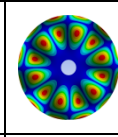
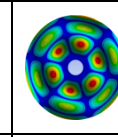
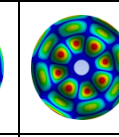
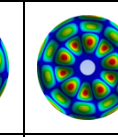


Fig. 7. 3D model of a diamond circular blade and its breakdown into tetrahedra

Tab. 3. Mode shapes and natural frequencies of a diamond circular blade obtained by calculation

				
139 Hz	187 Hz	364 Hz	931 Hz	994 Hz
				
1204 Hz	1583 Hz	2113 Hz	2756 Hz	2713 Hz
				
3049 Hz	3484 Hz	3508 Hz	4178 Hz	5033 Hz

The type of material chosen for the calculation is structural steel. Material properties: density - 7.81 g / cm<sup>3</sup>, Young's modulus - 200 GPa, Poisson's ratio - 0.28. A number of characteristic forms of oscillations obtained as a result of program calculation are presented in Tab. 3.

In addition, using the ANSYS Workbench software, a calculation was made of the natural frequencies and vibration modes for different clamping diameters of the diamond circular blade. For greater accuracy, the calculation was carried out taking into account the rim of the diamond circular blade, as well as without it. The results are presented in Tab. 4 and Tab. 5.

Tab. 4. Experimental and calculated values of the natural frequencies of the diamond circular blade without taking into account the rim

Experiment, Hz	Calculation of fixing diameter 42mm, Hz	Calculation of fixing diameter 44mm, Hz	Calculation of fixing diameter 46mm, Hz
153.0	139.0	143.0	148.0
200.0	187.0	191.0	194.0
377.0	364.0	365.0	366.0
944.0	931.0	956.0	981.0
980.0	994.0	1019.0	1044.0
1184.0	1204.0	1225.0	1246.0
1543.0	1583.0	1596.0	1610.0
2049.0	2113.0	2119.0	2125.0
2669.0	2756.0	2757.0	2760.0
2851.0	2713.0	2785.0	2857.0
3026.0	3049.0	3113.0	3177.0
3376.0	3484.0	3485.0	3485.0
3471.0	3508.0	3558.0	3610.0
4120.0	4178.0	4209.0	4244.0

Tab. 5. Experimental and calculated values of the natural frequencies of the diamond circular blade, taking into account the rim

Experiment, Hz	Calculation for clamping diameter 42mm, Hz	Calculation for clamping diameter 44mm, Hz	Calculation for clamping diameter 46mm, Hz
153.0	134.0	139.0	143.0
200.0	186.0	189.0	192.0
377.0	373.0	374.0	375.0
944.0	911.0	935.0	959.0
980.0	977.0	1000.0	1023.0
1184.0	1192.0	1212.0	1231.0
1543.0	1577.0	1590.0	1602.0
2049.0	2117.0	2123.0	2126.0
2669.0	2773.0	2775.0	2773.0
2851.0	2667.0	2735.0	2802.0
3026.0	3016.0	3076.0	3134.0
3376.0	3519.0	3519.0	3515.0
3471.0	3488.0	3536.0	3581.0
4120.0	4173.0	4204.0	4231.0

## 4. RESULTS

A graph of the results of the experiment is given (Fig. 5), as well as graphs of the errors in calculating various diameters of fastening the diamond circular blade (Fig. 8).

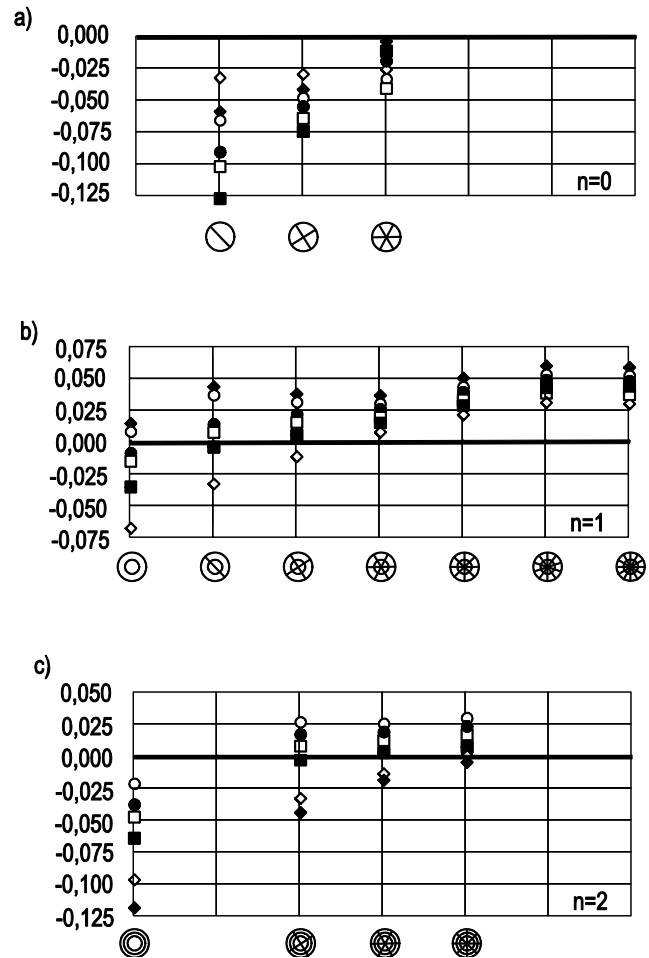


Fig. 8. The relative error of the calculated for clamping diameters of the diamond circular blade relative to the experiment; where number of modal circles is, a)  $n = 0$ , b)  $n = 1$ , c)  $n = 2$ ; ● - Ø44 with a rim, ○ - Ø44 without a rim, ◆ - Ø46 with a rim, ◇ - Ø46 without a rim, ■ - Ø42 with a rim, □ - Ø42 without a rim.

The ratios of the experimental and calculated program frequencies are relatively equal (Table 5), therefore, the difference between them is caused by the difference in geometry between the analytical and real circular blades (Joenathan et al. 1995), (Qin et al. 2016) and the incorrectly selected material property for program calculation.

The value of the mean squared error of the program calculation of frequencies for different clamping diameters of the diamond circular blade, as well as for a different number of nodal circles, is presented in Tab. 6.

**Tab. 6** The root mean squared error of the calculation of frequencies, for the n=0, n=1 and n=2 respectively

n=0	ø42	ø44	ø46
With rim	0,0825	0,0619	0,0444
Without rim	0,0678	0,0493	0,0311

n=1	ø42	ø44	ø46
With rim	0,0295	0,0309	0,0375
Without rim	0,0253	0,0327	0,0447

n=2	ø42	ø44	ø46
With rim	0,0331	0,0265	0,0287
Without rim	0,026	0,0245	0,0353

5. VERIFICATION OF EXPERIMENTAL STAND


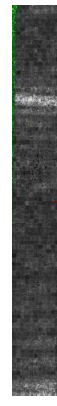
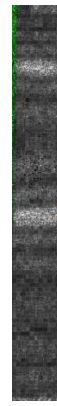
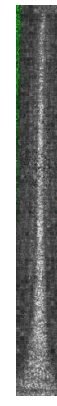
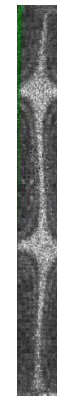

5.1. Experimental determination of natural frequencies and mode shapes of a rectangular rod

To test the operability, as well as the serviceability of the experimental bench, tests were carried out in advance of a rectangular steel rod. The rod material is carbon steel 45. Rod dimensions: length - 240 mm, width -  $22.25 \pm 0.21$  mm, thickness -  $3.78 \pm 0.03$  mm.

To carry out the experiment, the lower part of the rod clamped by two plates in the clamp; the upper part is free. The length of the free oscillating console part of the rod is 200 mm and clamped part is 40 mm. The size of the plates used for clamping the rod is: length - 50 mm, width - 50 mm, thickness – 20 mm.

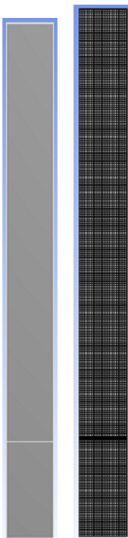
A number of characteristic waveforms obtained from the tests are presented in Tab. 7.

**Tab. 7.** Experimental natural frequencies and mode shapes of a rectangular rod

					
71 Hz	447 Hz	1209 Hz	1246 Hz	6392 Hz	9051 Hz

5.2. Calculation of natural frequencies and mode shapes of a rod of rectangular cross section by the finite element method

Using the ANSYS Workbench software, we obtained resonant frequencies and the corresponding vibration modes of a rectangular rod. For this, a 3D model of the rod was created, the properties, type, and clamping scheme of which are described in Section 5.1. For calculation, the 3D model was divided into individual cubic elements, (about 400 thousand) and is shown in Fig. 9. The element type used in the calculation is SOLID186; the element size is 1 mm. The boundary conditions: clamping for down side and free at three sides.


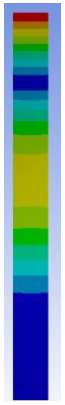
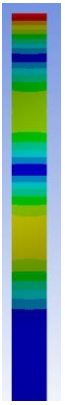
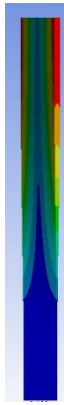
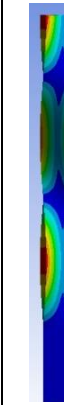
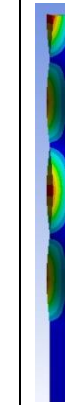


**Fig. 9.** 3D model of the rod and its division into finite elements

The type of material chosen for the calculation is structural steel. Material properties used in the calculation: density -  $7.81 \text{ g / cm}^3$ , Young's modulus - 200 GPa, Poisson's ratio - 0.28.

A number of characteristic forms of oscillations obtained as a result of program calculation are presented in Tab. 8

**Tab. 8.** Natural frequencies and mode shapes of the rod obtained in the ANSYS program

					
77,5 Hz	485,2 Hz	1356,1 Hz	1274,7 Hz	6480,5 Hz	9217,4 Hz



### 5.3. Comparison of the results of calculating the natural frequencies and mode shapes of a rod of rectangular cross section

A comparison of the frequencies of the resonant vibrations of the rod obtained experimentally, analytically and using the finite element method is shown in table. 9. The analytical calculation was carried out using the Euler–Bernoulli beam theory (Babakov, 1965).

**Tab. 9.** Comparison of the results of an experimental study and calculation of a rod

Mode shape		The experimental frequency, Hz	Calculation, Hz	
Torsional	Flexural		FEM	Analytical
0	1	71	77	77.8
0	2	447	485	482.5
0	3	1209	1356	1370.5
1	0	1246	1274	1244.7
1	2	6392	6480	6223.4
1	3	9051	9217	8712.7

## 6. CONCLUSIONS

A stand has been created to determine the natural frequencies and mode shapes using real-time electronic speckle-pattern interferometry.

An experimental study of the natural frequencies and mode shapes of a diamond circular blade was carried out using real-time electronic speckle-pattern interferometry. 15 mode shapes of the diamond circular blade were revealed in the frequency range from 100 to 5000 Hz.

A programmatic calculation of the natural frequencies and mode shapes by the finite element method for three diameters of fastening the diamond circular blade was made.

The experimental results are compared with the calculated ones, the mean squared error and an error analysis is also carried out.

To test the operability, as well as the serviceability of the experimental bench, tests and calculations of a rectangular steel rod were carried out.

## REFERENCES

1. Babakov I.M. (1965), *Theory of vibrations* [Teoriya kolebaniy], Science [Nauka]. [In Russian]
2. Beeck M.A., Hentschel W. (2000), Laser metrology - a diagnostic tool in automotive development processes, *Optics and Lasers in Engineering*, 34(2), 101–120.
3. Bystrov, N. D., Zhuzhukin, A. I. (2017), Speckle Interferometry in the Investigation of Large-Size Turbine Engine Structures Vibration, *Procedia Engineering*, 176: 471–475.
4. Careva A.M., Tupoleva A.N. (2006), *Application of an experimental calculation method for determining resonant frequencies and vibration modes of a disk of constant thickness* [Primenenie eksperimentalno-raschetnogo metoda dlya opredeleniya rezonansnykh chastot i form kolebaniy diska postoyannoy tolshiny], Kama State Academy of Engineering and Economics [Kamskaya gosudarstvennaya inzhenerno-ekonomicheskaya akademiya]. [In Russian]
5. Chi-Hung H., Yu-Chih L., Chien-Ching M. (2004) Theoretical analysis and experimental measurement for resonant vibration of piezoceramic circular plates, *IEEE Transactions On Ultrasonics, Ferroelectrics, And Frequency Control*, 51(1), 12–24.
6. Chladni. E., Beyer T. (2015), *Treatise on Acoustics*, Springer International Publishing Switzerland.
7. Foitzik A.H., Kaese W., Vogt T., Sommerer M., Arkhipov S. (2003), Static and Dynamic Characterization of MEMS via ESPI, *International Journal Of Computational Engineering Science*, 4(3), 467–470.
8. Gorbatenko B.B., Lyakin D.V., Perepelitsyna O.A., Ryabukho V.P. (2001), Optical schemes and statistical properties of displacement speckle interferometer signal [Opticheskie shemi i statisticheskie harakteristiki signala spekl-interferometrov peremesheniy], *Computer optics* [Kompyuternaya optika], tom 33, №3. [In Russian]
9. Halama R., Hornacek L., Pecenk L., Krejsa M., Smach J. (2016), 3-D ESPI Measurements Applied to Selected Engineering Problems, *Applied Mechanics and Materials*, 827, 65–68.
10. Joenathan C., Sohmer A., Burkle L. (1995), Increased sensitivity to in-plane displacements in electronic speckle pattern interferometry, *Appl. Opt.*, Vol. 34, No.16, 2880–2885
11. Jones R., Wykes C. (1989), *Holographic and Speckle Interferometry*. 2 edition, Cambridge University Press.
12. Komarov Yu.S. (2004), *Noise-resistant digital speckle interferometer for vibrometry of objects based on the method of averaging over time* [Pomehoustoichiviy cifrovoy spekl-interferometr dlya vibrometrii obektov na osnove metoda usredneniya vo vremeni], Abstract of dissertation for the degree of candidate of technical sciences [Avtoreferat dissertatsii na soiskanie uchenoj stepeni k.t.n.]. [In Russian]
13. Levin A.V. (1953), *Working Blades and Disks of Steam Turbines* [Rabochije lopatki i diski parovykh turbin], Gosenergoizdat [Gosenergoizdat]. [In Russian]
14. Makaeva R.Kh., Tsareva A.M., Karimov A.Kh. (2008), Determination of natural frequencies and forms of vibrations of the disk of constant thickness, fixed in the center // *Izv. vuzov. Aviation technique*, No 1 - C. 41 - 45.
15. Makaeva R.Kh., Tsareva A.M., Karimov A.Kh. (2008), Determination of natural frequencies and vibration modes of a constant thickness centrally secured disk. *Russ. Aeronaut.* 51, 53–59 (2008).
16. Mihaylova E., Naydenova I., Martin S., Toal V. (2004), Electronic speckle pattern shearing interferometer with a photopolymer holographic grating, *Appl. Opt.*, Vol. 43, No. 12, 2439–2442.
17. Mihaylova E., Naydenova I., Martin S., Toal V. (2006), Photopolymer diffractive optical elements in electronic speckle pattern shearing interferometry, *Opt. Lasers Eng.*, Vol. 44, No. 9, 965–974.
18. Mrozek P., Mrozek E., Werner A. (2018), Electronic speckle pattern interferometry for vibrational analysis of cutting tools, *Acta Mechanica et Automatica*, vol 12, no.2.
19. Petrov V., Lau B. (1996), Electronic speckle pattern interferometry with a holographically generated reference wave, *Opt. Eng.* Vol. 35, No. 8, 2363–2370.
20. Qin J., Gao Z., Wang X., Yang S. (2016), Three-Dimensional Continuous Displacement Measurement with Temporal Speckle Pattern Interferometry, *Sensors*, (Basel, Switzerland).
21. Richardson M.O.W., Zhang Z.Y., Wisheart M., Tyrer J.R. Petzing J. (1998), ESPI non-destructive testing of GRP composite materials containing impact damage, *Composites Part A*, 29A, 721–729.
22. Tkach M. et al. (2021) Improving the Noise Immunity of the Measuring and Computing Coherent-Optical Vibrodiagnostic Complex, In: Nechiporuk M., Pavlikov V., Kritskiy D. (eds) *Integrated Computer Technologies in Mechanical Engineering* - 2020.

- ICTM 2020, *Lecture Notes in Networks and Systems*, vol 188. Springer, Cham.
23. **Tkach M.R., Zolotiy Yu.G., Dovgan D.V., Guk I.Yu.** (2012), Determination of the natural vibration forms of gas turbine engine elements in real time by electron speckle interferometry [Opredelenie form sobstvennih kolebanij elementov GTD v realnom vremeni metodom elektronnoj spekl-interferometrii], *Aerospace technic and technology* [Aviacionno-kosmicheskaya tehnika i tehnologiya] № 8 (95). [In Russian]
  24. **Tkach M.R., Zolotiy Yu.G., Dovgan D.V., Guk I.Yu.** (2015), *Patent: Method of determining of forms of resonant vibrations shapes of blades of gas turbine engine by speckle interferogram*, UA 103068. [In Ukrainian]
  25. **Tkach, M., Morhun, S., Zolotoy, Y., Zhuk, I.** (2020), Modal analysis of the axial compressor blade: advanced time-dependent electronic interferometry and finite element method, *Int. J. Turbo Jet-Eng.*
  26. **Van der Auweraer H., Steinbichler H., Vanlanduit S., Haberstok C., Freymann R., Storer D., Linet V.** (2002), Application of stroboscopic and pulsed-laser electronic speckle pattern interferometry (ESPI) to modal analysis problems, *Measurements Science and Technology*, 13, 451–463.
  27. **Vest. C. M.** (1982), *Holographic Interferometry*, John Wiley and Sons, New York.
  28. **Wailer, M.D.**, (1961), *Chladni Figures: a Study in Symmetry*, G. Beil & Sons (London).
  29. **Yang L., Xie X., Zhu L., Wu S., Wang Y.** (2014), Review of Electronic Speckle Pattern Interferometry (ESPI) for Three Dimensional Displacement Measurement, *Chinese Journal Of Mechanical Engineering*, 27(1), 1–13.
  30. **Yelenevsky D.S., Shaposhnikov Yu.N.** (2001), *Investigation of acoustic emission procession of the structures through electronic speckle interferometry methods* [Issledovanie processov zvukoizluchenia konstrukcij metodami elektronnoj spekl-interferometrii], *Izvestiya of the Samara Science Centre of the Russian Academy of Sciences* [Izvestiya Samarskogo Nauchnogo Centra Rossijskoj Akademii Nauk]. [In Russian]
  31. **Zhuzhukin A.I.** (2011), A mobile speckle interferometer for studying vibration modes of vibrating objects outside bench conditions [Mobilnyj spekl-interferometr dlya issledovaniya form kolebanij vibriruyushih obektov vo vne stendovyh usloviyah], *Electronic journal «Trudy MAI»* [Elektronnyj zhurnal «Trudy MAI»] № 48. [In Russian]
  32. **Zhuzhukin A.I., Solyannikov V.A.** (2014), *Method of reducing speckle-interferometer sensitivity for the study of turbomachine elements vibration* [Metod umensheniya chuvstvitelnosti spekl-interferometra pri issledovanii vibratsii detalej turbomashin], *Vestnik of Samara University: Aerospace and Mechanical Engineering* [Vestnik Samarskogo gosudarstvennogo aerokosmicheskogo universiteta] № 1(43). [In Russian]



# EFFICIENT NON-ODOMETRY METHOD FOR ENVIRONMENT MAPPING AND LOCALISATION OF MOBILE ROBOTS

Mateusz ADAMOWICZ\*, Leszek AMBROZIAK\*, Mirosław KONDRATIUK\*

\*Department of Robotics and Mechatronics, Faculty of Mechanical Engineering, Białystok University of Technology,  
 ul. Wiejska 45C, 15-351 Białystok, Poland

[mateusz.adamowicz.1994@gmail.com](mailto:mateusz.adamowicz.1994@gmail.com), [l.ambroziak@pb.edu.pl](mailto:l.ambroziak@pb.edu.pl), [m.kondratiuk@pb.edu.pl](mailto:m.kondratiuk@pb.edu.pl)

received 13 October 2020, revised 14 April 2021, accepted 19 April 2021

**Abstract:** The paper presents the simple algorithm of simultaneous localisation and mapping (SLAM) without odometry information. The proposed algorithm is based only on scanning laser range finder. The theoretical foundations of the proposed method are presented. The most important element of the work is the experimental research. The research underlying the paper encompasses several tests, which were carried out to build the environment map to be navigated by the mobile robot in conjunction with the trajectory planning algorithm and obstacle avoidance.

**Key words:** mobile robot, mapping, navigation, obstacle detection, obstacle avoidance

## 1. INTRODUCTION

In recent years, robotics researchers have shown an increasing interest in autonomy of mobile vehicles. The autonomy of robots is mainly associated with obstacle detection and avoidance systems (Gao et al., 2019; Rulin, 2017), precise navigation systems (Romaniuk et al., 2016; Bakkali et al., 2007), new control methods allowing adaptation to failures (Ambroziak et al., 2019; Lanzon et al., 2014), cooperation of a few objects, and formation and swarm motion (Ambroziak et al., 2015; Kownacki et al., 2019). Mentioned topics relate to tasks carried out by mobile robots in indoor and outdoor conditions. In both cases the problem of navigating a robot in an unknown environment without the possibility of global positioning system (GPS), real-time localisation system (RTLS), etc. usage is a current topic. Frequently, the task of navigating a mobile robot is based on a map built during a mission, which is at the same time used to try to localise the robot. This is known as the Simultaneous Localisation and Mapping (SLAM) technique, and has been discussed in the works of Disanayake et al. (2000) and Dissanayake et al. (1999). SLAM is one of the key enabling technologies of mobile robot autonomy and is regarded as one of most important problems in the pursuit of building fully autonomous objects. Despite a significant progress in this topic, it is still a great challenge and an open case (Chen et al., 2017). Currently available SLAM methods provide good solutions for mapping static, structured environments with limited volume-size. However, facilitating a robot to autonomously navigate a map of unstructured, dynamic and large-size environment continues to remain an emerging and open research problem. In many different SLAM techniques we can distinguish full (Guivant et al., 2002) and online (Dubbelman et al., 2015) ones. Other common distinctions are volumetric and feature-based (Li et al., 2019), topological and metric (Li et al., 2010), active and passive (Soragna et al., 2019), and single- and multi-robot (Xiaolin

et al., 2012). All SLAM techniques use different methods of filtration and position estimation. The most popular one is the usage of Extended Kalman Filters (EKF SLAM). EKF SLAM was introduced in Smith et al. (1990) and Moutarlier et al. (1989); these were single state vectors used to estimate robot locations. A second set of algorithms solving the SLAM are the graph-based optimisation techniques. Graph-based approach was first described in Lu et al. (1997) and Dellaert (2005). The third group of SLAM techniques is based on particle filters, which is a kind of nonparametric statistical filtering technique. This method was introduced in Zhu et al. (2019) and mostly popular in online SLAM because of grooving availability of cheap and efficient computers on module.

SLAM techniques and all previously listed methods require the use of appropriate sensors and are using odometry information. Methods that do not use odometry are not found in the literature and we can mention a few papers such as Klecka et al. (2014), where authors propose non-odometry feature based approach to SLAM.

This paper addresses the problem of SLAM without any additional odometry measurement sensor such as inertial measurement unit (IMU) or encoders for movements' calculations. The theoretical foundations of the proposed method are presented. The most important element of the work is the experimental research: a number of tests were carried out to build the environment map to be navigated by the mobile robot in conjunction with the trajectory planning algorithm and obstacle avoidance.

## 2. SENSOR SYSTEM USED IN STUDIES

Different SLAM methods use different types of sensors such as CCD cameras, rangefinders, lidars, and RGBD sensors. In this work, scanning laser range finder UTM30-LX (Fig. 1) was used. This kind of sensor emits a pulse every quarter, half or one de-

gree over an angular range of 270° and returns a planar cross-section of the observed scene in polar coordinate form. The use of a specific type of sensor requires checking its measurement quality. The quality of the measurement depends on the following stages.



Fig. 1. Laser range finder UTM30-LX

Laser rangefinder UTM30-LX allows to measure distances in the range of 0.1–30.0 m. An important parameter is the standard deviation of the measurement from the actual value, because it determines the resolution of the environment map (it is not possible to make an environment map with an accuracy of 1 mm if the standard deviation is, for example, 10 mm).

Fig. 2 shows standard deviation of the scanning laser rangefinder measurements at different angles of surface, which reflected the beam of radiation coming from the sensor. There is a relatively large increase in the standard deviation for position of the reflecting surface other than perpendicular to the laser beam, but these are still quite small values (Nakamura et al., 2014).

On the basis of the results shown in the Fig. 2, it can be stated that it is possible to make the environment map with the accuracy of 1 cm with using scanning laser rangefinder.

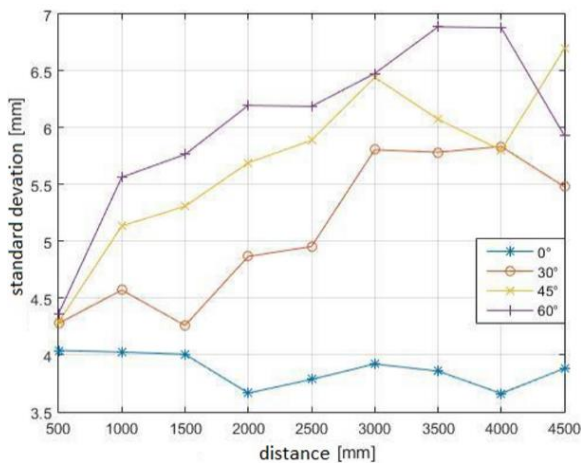


Fig. 2. Standard deviation of laser scanning range finder measurements

### 3. DESCRIPTION OF THE LOCALISATION AND MAPPING ALGORITHM

The main idea of the algorithm is the same as in the article (Janah et al., 2018). The localisation method is based on applying scan (cloud of points from one measurement taken with scanning laser rangefinder) to the environment map. Applying a scan con-

sists in performing a rotation and displacement of it such that the greatest number of points overlaps the map of the environment – the more points imposed, the better the scan fits and thus more accurate the position and orientation relative to the surroundings.

The difference between the presented approach and the approach from work (Janah et al., 2018) is the way of moving and rotating the scan in order to match it with the map. In Janah et al. (2018) the Particle Swarm Optimisation (PSO) algorithm was used, while in this work a brute force algorithm was chosen (description shown below).

Firstly, measurements from one scan are collected and stored. If the first scan is done, the collected points are saved on the map. In case of other scans, calculations are made to determine the location. If the location has changed, the points collected in this scan are placed on the map. After mapping, if the scan was the last one, the program ends. In any other case, the next measuring cycle starts. Fig. 3 presents the flowchart of the proposed localisation and mapping method.

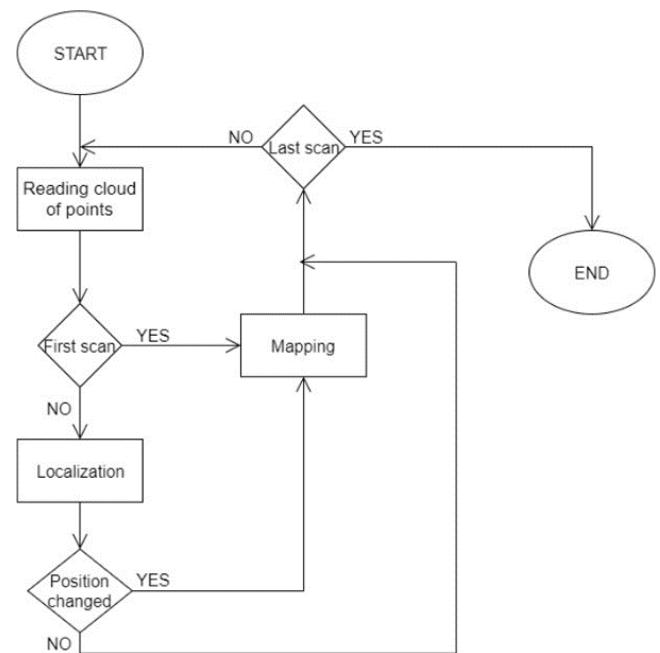


Fig. 3. Flowchart of localisation and mapping method

Fig. 4 shows the location and orientation of the laser range finder relative to the global coordinate system. The map of environment shows the points at which obstacles in the global coordinate system were detected. The transfer of measured points to the global coordinate system is based on the formula:

$$\begin{bmatrix} {}^mX_i \\ {}^mY_i \end{bmatrix} = \begin{bmatrix} \cos(\varphi_r) & -\sin(\varphi_r) \\ \sin(\varphi_r) & \cos(\varphi_r) \end{bmatrix} \begin{bmatrix} {}^sX_i \\ {}^sY_i \end{bmatrix} + \begin{bmatrix} x_r \\ y_r \end{bmatrix} \quad (1)$$

where  $x_r$ ,  $y_r$ ,  $\varphi_r$  – are coordinates informing about the linear and angular position of the laser range finder relative to the global coordinate system;  $P_i$  –  $i$ -th point of the scan;  ${}^sX_i$ ,  ${}^sY_i$  – the coordinates of the  $i$ -th point in the coordinate system associated with the laser range finder; and  ${}^mX_i$ ,  ${}^mY_i$  – the coordinate of the  $i$ -th point in the global coordinate system.

The location system searches for relevant shifting and rotation changes to minimise the function  $f(z)$ , which is shown below:

$$f(z) = 1 - \frac{Data_{fit}(z)}{Data_{valid}} \quad (2)$$

where  $z = [\delta_x, \delta_y, \delta_\varphi]^T$  is shift and rotation of the sensor coordinate system relative to the coordinate system in the previous measurement cycle, which is elucidated in Nakamura et al. (2014) and Janah et al. (2018).

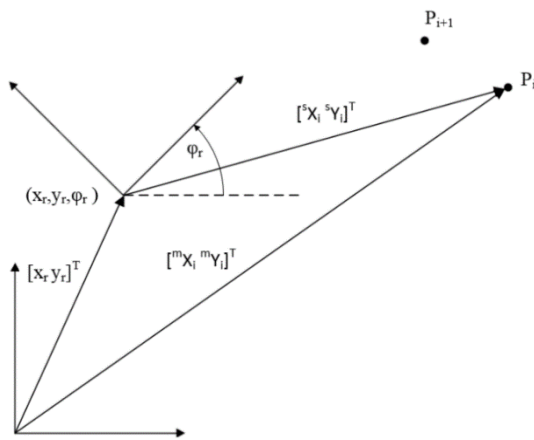


Fig. 4. Coordinate system

$Data_{valid}$  is the number of points collected in the current scan that are suitable for determining the location. Points are rejected whose distance from laser range finder is less than 15 cm, and those that are the result of the mixed pixels effect.

$$Data_{fit}(z) = \sum_{i=1}^N g(i) \quad (3)$$

$Data_{fit}(z)$  is the number of points that were taken into account when calculating  $Data_{valid}$  and coincide with the map. The  $g(i)$  function assumes a value of 0 if the  $i$ -th point is not reflected on the map and 1 in the other cases. The affiliation of a given point to the map is checked after the earlier appropriate rotation and moving this point to the global coordinate system.

Minimising the  $f(z)$  function consists in searching for such  $z$ , for which this function assumes the smallest value. Ideally, this means finding a relative shift and rotation for which  $f(z)$  assumes a value of 0. This would mean that all points taken into account are reflected in the environment map.

Fig. 5 shows how the search algorithm for relative displacement and rotation works. The relative displacement in the coordinate axes is limited on the range from  $-5$  cm to  $5$  cm every  $1$  cm (map resolution) and relative rotation from  $-5^\circ$  to  $5^\circ$  every  $0.2^\circ$  (appropriate relative displacement is shown as gray cells, current position of the sensor as a black cell). From the given area, the  $z$  for which the  $f(z)$  function has the smallest value is selected.

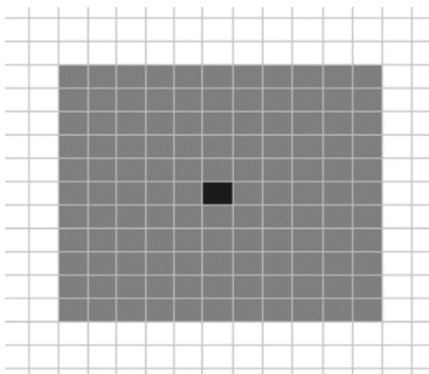


Fig. 5. Search area around the sensor position in the previous cycle

## 4. OBSTACLES DETECTION

In order for the robot to get from the start point to the target point, it must detect objects that stand in its way and prevent it from travelling between these points in a straight line. To this end, the so-called occupancy matrix determines the places where, due to the existence of obstacles, the robot is not able to physically find itself (as the robot is understood as the centre of the sensor in the plan view).

For ease of use, the area where the robot will move will be limited to the surface of a square with  $2 \text{ m} \times 2 \text{ m}$  sides. The occupancy matrix will take the form of a  $200 \times 200$  array, each element corresponding to a square with sides of  $1 \text{ cm} \times 1 \text{ cm}$ . The element assumes a value of 1 if the robot cannot be found in the given square with sides of  $1 \text{ cm} \times 1 \text{ cm}$ . Fig. 6 shows how the cells that the surface is divided into are assigned to the occupancy matrix  $T$ .

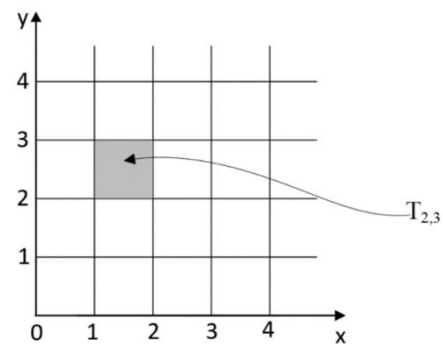


Fig. 6. Division of operational environment into elementary cells

The obstacle detection and avoidance method assume a safe area around each obstacle (larger than the nominal dimensions of the object). Fig. 7 presents the way of representing obstacles and the obstacle-free area. Obstacles are shown in black colour. The gray area indicates the area where the robot cannot be found due to its dimensions – safety area (zone). The area in which the robot can move is marked in white.

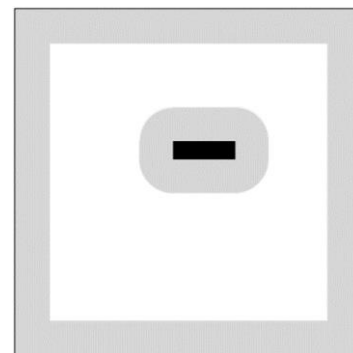


Fig. 7. Obstacle and safety zone scheme

## 5. PATH PLANNING

Robot path planning is an important element of the mobile robot navigation process. In this case, Rapidly Exploring Random Trees (RRT) algorithm was used due to the fact that it can be

used as an online planning method and does not need large computing resources. Furthermore, RRT method is quite simple approach to planning paths through an obstacle field from a start node to an end node.

Fig. 8 shows the principle and the result of track search using the RRT algorithm. A graph is created to which nodes and edges are added randomly. A random  $q_{rand}$  point is created. The graph is searched for the node closest to the  $q_{rand}$  point. This node is called  $q_{near}$ . An episode with  $q_{rand}$  and  $q_{near}$  ends is created. On this segment,  $q_{new}$  is placed at a distance equal to the length of the step (if the segment length is less than the length of the step,  $q_{rand}$  becomes the point of  $q_{new}$ ) from the point  $q_{near}$ . A new node is added to the graph, which is the point  $q_{new}$  and a new edge, i.e. a segment with ends at points  $q_{near}$  and  $q_{new}$ .

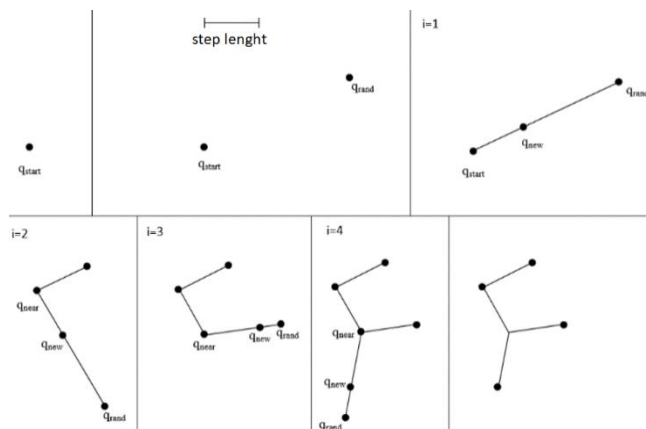


Fig. 8. Obstacle and safety zone scheme

## 6. MOBILE PLATFORM

A mobile robot platform specially prepared for this purpose was used to conduct the experimental tests of mapping, localisation, obstacle detection, avoidance and path planning. It is a four-wheeled robot with each wheel separately driven by a DC motor (Fig. 9). Beagle Bone Black computer on module (COM) was used as a main computer responsible for all navigational tasks. COM collects data from scanning laser rangefinder, which was mounted on the top of the robot. The UTM-30LX laser scanner communicates with the computer via a USB port. This causes many difficulties related to the implementation of communication. The robot is using the Linux Debian 7.5 operating system. Libraries responsible for map building, location, obstacle avoidance and trajectory planning were developed.



Fig. 9. Mobile platform used in the experimental tests

## 7. TEST'S RESULTS

The mobile robot's navigation task was divided into three parts: mapping and localisation, obstacle detection and path planning. A special, structured test environment has been developed for the experimental verification of the algorithms (Fig. 10). The prepared environment was specially configured to be simplified and in the first stage of the algorithm, sufficient verification was carried out to check all parts of the navigation system. Scheme of the objects' placement located in the experimental environment is presented in the Fig. 11. The scheme shows the environment in which the localisation algorithm was tested. The black point at the bottom of the picture indicates the place where the sensor was placed when the program implementing this location method started.



Fig. 10. Experimental environment

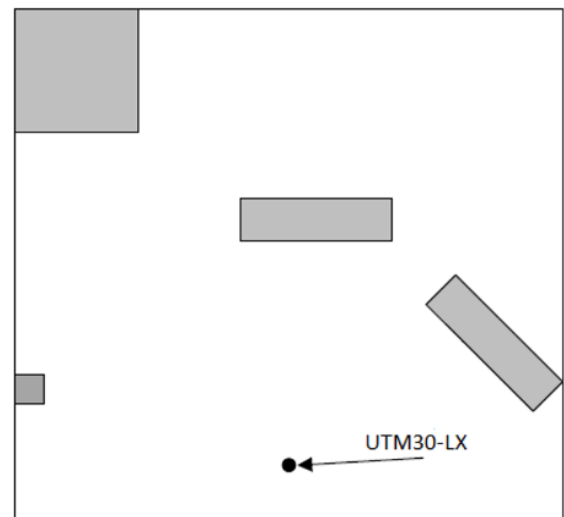
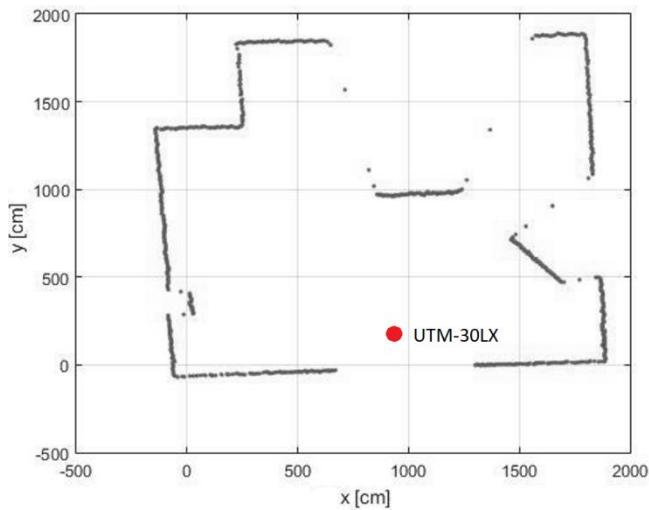


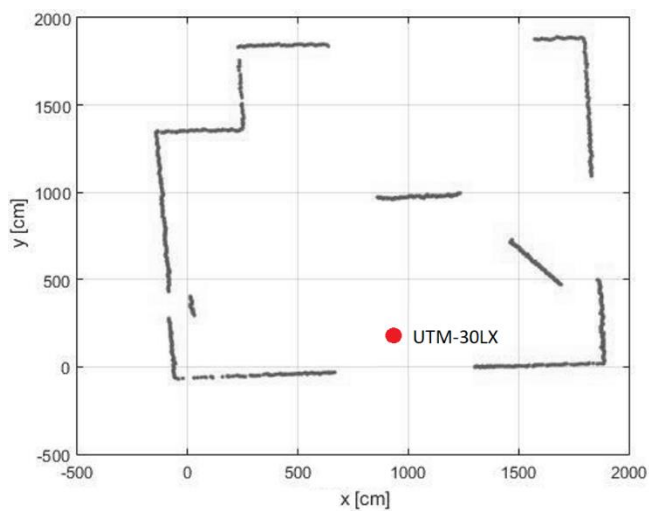
Fig. 11. Placement of objects in experimental environment

Figs 12–14 show how important it is to process data from the sensor. Using the data visible on Fig. 12, ascertainment of the correct location is possible but the map would be updated with incorrect points, which with each step would have an increasing impact on the correctness of location determination and would completely prevent the correct operation of the other systems, such as setting a path to avoid obstacles.

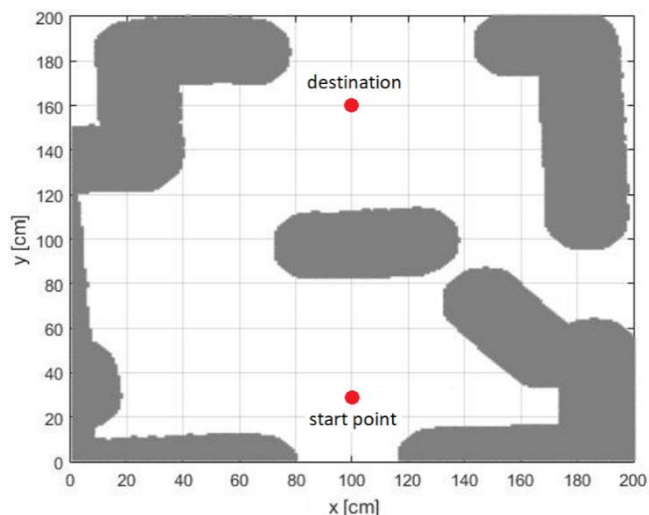




**Fig. 12.** Cloud of points from the raw data (Gao et al., 2019)



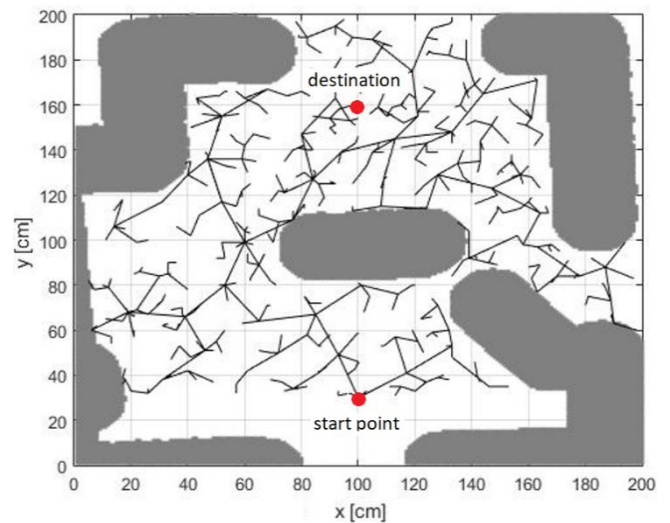
**Fig. 13.** Cloud of points after data filtration (Gao et al., 2019)



**Fig. 14.** Occupancy grid generated with using prepared map of the environment

After removing the error points (filtration was presented in Fig. 13), an occupancy matrix was created. Fig. 15 presents this matrix in a graphic form. The area in which the robot cannot be found

is highlighted in gray. The robot can move freely in the white area.

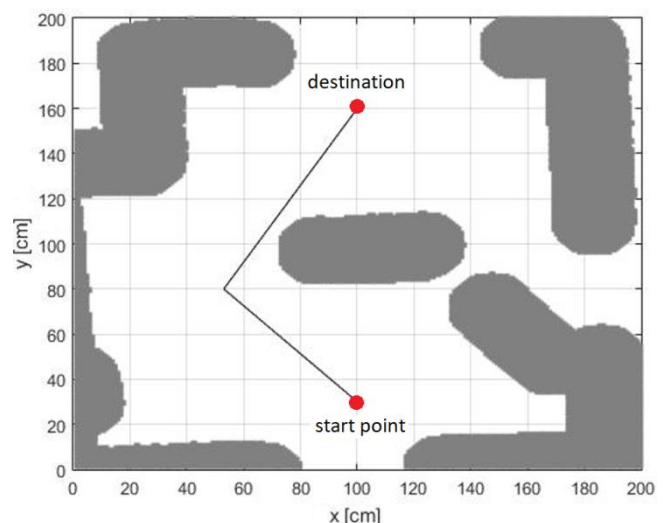


**Fig. 15.** Generated graph with RRT path planning method. RRT - rapidly exploring random trees

It is very clearly visible in Fig. 14 that some areas within which the robot cannot move are not included in the occupancy matrix. This is due to the fact that the sensor does not collect distance from objects behind other objects. Therefore, when the mobile robot performs the obstacle avoidance task, this matrix must be updated, and the RRT graph and path mapping ought to be created again.

To create the path that the robot should follow so that it can get from the start point to the target point, the RRT algorithm described was used. Fig. 15 shows the results of this algorithm for 500 iterations. The inaccessible area is marked in gray. The graph is black. The area of graph filling was limited from below by the coordinate of the position of the sensor. The graph fills the white area with the edges without crossing the gray area. The edges are therefore sections on which the robot can move without interfering with other objects.

After searching the graph and applying the smoothing and optimisation algorithm, the desired robot path was obtained and presented in Fig. 16.



**Fig. 16.** Found and optimised path

In the original implementation, the sensor location was determined every few seconds. Modification of the method was based on using every 20-th point of the scan to determine the location and updating the map with all points. This modification caused a significant increase in the speed of algorithm (200 iterations of the algorithm were made in 36.7 s).

## 8. CONCLUSIONS

The paper addresses the problem of SLAM without any additional odometry measurements sensor for movements' calculations. Only laser scanner rangefinder data were used to build the map and locate the robot. Whole navigation system of the robot includes mapping and localisation subsystem, obstacle detection and avoidance system based on a prepared map and path planning algorithm using RRT method. The next step should be testing of the system in an unstructured environment, which is crowded with more objects.

## REFERENCES

1. Ambroziak L., Gosiewski Z. (2015), Two stage switching control for autonomous formation flight of unmanned aerial vehicles, *Aerospace Science and Technology*, Vol. 46, 221–226.
2. Ambroziak L., Simha A., Pawluszewicz E., Kotta Ü., Bożko A., Kondratiuk M. (2019), Motor Failure Tolerant Control System With Self Diagnostics for Unmanned Multirotors, *24th International Conference on Methods and Models in Automation and Robotics (MMAR)*, Międzyzdroje, Poland, 422–427.
3. Bekkali A., Sanson H., Matsumoto M. (2007), RFID indoor positioning based on probabilistic RFID map and Kalman filtering, *Proc. of the 3rd IEEE International Conference on Wireless and Mobile Computing Networking and Communications*, 21.
4. Chen X, Zhang H, Lu H., Xiao J., Qiu Q., Li Y. (2017), Robust SLAM system based on monocular vision and LiDAR for robotic urban search and rescue, *IEEE International Symposium on Safety, Security and Rescue Robotics (SSRR)*, Shanghai, 41–47.
5. Dellaert F. (2005): *Square root SAM*, *Robotics Sci. Syst.*, ed. by S. Thrun, G. Sukhatme, S. Schaal, O. Brock, MIT Press, Cambridge.
6. Dissanayake G., Durrant-Whyte H., Bailey T. (2000), A computationally efficient solution to the simultaneous localisation and map building (SLAM) problem, *Proc. of the IEEE International Conference on Robotics and Automation (ICRA) - Millennium Conference, Symposia Proceedings (Cat. No.00CH37065)*, Vol. 2, San Francisco, CA, USA, 1009–1014.
7. Dissanayake G., Newman P., Durrant-Whyte H. F., Clark S., Csobor M. (1999), An experimental and theoretical investigation into simultaneous localisation and map building (SLAM), *Proc. of the 6th International Symposium on Experimental Robotics*, March, 171–180.
8. Dubbelman G., Browning B. (2015), COP-SLAM: Closed-Form Online Pose-Chain Optimization for Visual SLAM, *IEEE Transactions on Robotics*, Vol. 31, No. 5, Oct., 1194–1213.
9. Gao M., Tang J., Yang Y., He Z., Zeng Y. (2019) An Obstacle Detection and Avoidance System for Mobile Robot with a Laser Radar, *16th IEEE International Conference on Networking, Sensing and Control (ICNSC)*, Banff, AB, Canada, 63–68.
10. Guivant J., Nebot E. (2002), Improving computational and memory requirements of simultaneous localization and map building algorithms, *Proc. of the IEEE International Conference on Robotics and Automation (Cat. No.02CH37292)*, Vol. 3, Washington, DC, USA, 2731–2736.
11. Janah M., Fujimoto Y. (2018), Performance Analysis of an Indoor Localization and Mapping System Using 2D Laser Range Finder Sensor, *44th Annual Conference of the IEEE Industrial Electronics Society (IECON)*, 5463–5468.
12. Klecka J., Horak K., Novacek P., Davidek D. (2016), Non-odometry SLAM and Effect of Feature Space Parametrization on its Covariance Convergence, *IFAC-PapersOnLine*, Vol. 49, Issue 25, 139–144.
13. Kownacki, C., Ambroziak, L. (2019), Adaptation Mechanism of Asymmetrical Potential Field Improving Precision of Position Tracking in the Case of Nonholonomic UAVs, *Robotica* (DOI: 10.1017/S0263574719000286), Vol. 37, No.10, 1823–1834.
14. Lanzon A., Freddi A., Longhi S. (2014), Flight control of a quadrotor vehicle subsequent rotor failure, *Journal of Guidance Control and Dynamics*, Vol. 37, No. 2, 580–591.
15. Li H., Chen Q. (2010), Towards a non-probabilistic approach to hybrid geometry-topological SLAM, *8th World Congress on Intelligent Control and Automation*, Jinan, 1045–1050.
16. Li P., Ke Z. (2019), Feature-based SLAM for Dense Mapping, *International Conference on Advanced Mechatronic Systems (ICAMechS)*, Kusatsu, Shiga, Japan, 372–377.
17. Lu F., Milios E. (1997), Globally consistent range scan alignment for environmental mapping, *Auton. Robots* 4, 333–349.
18. Moutarlier P., Chatila R. (1989), Stochastic multisensory data fusion for mobile robot location and environment modeling, *5th Int. Symp. Robotics Res. (ISRR)*, 207–216.
19. Nakamura Y., Fujimoto Y. (2014), Validation of SLAM without odometry in outdoor environment, *13th IEEE International Workshop on Advanced Motion Control (AMC)*, Yokohama, 278–283.
20. Romaniuk S., Ambroziak L., Gosiewski Z., Isto P. (2016), Real time localization system with Extended Kalman Filter for indoor applications, *21st International Conference on Methods and Models in Automation and Robotics (MMAR)*, Międzyzdroje, Poland, 42–47.
21. Rulin H. (2017), *Research on Key Technologies of Dynamic Obstacle Avoidance in Driverless Vehicles*, University of Science and Technology of China.
22. Smith R., Self M., Cheeseman P. (1990), *Estimating uncertain spatial relationships in robotics*, *Autonomous Robot Vehicles*, ed. by I.J. Cox, G.T. Wilfong, Springer Verlag, Berlin, Heidelberg, 167–193.
23. Soragna A., Baldini M., Joho D., Kümmerle R., Grisetti G. (2019), Active SLAM using Connectivity Graphs as Priors, *IEEE/RSJ International Conference on Intelligent Robots and Systems (IROS)*, Macau, China, 340–346.
24. Xiaolin W., Jing Y., Fengchi S., Huan C., Shuzi H. (2012), An approach to multi-robot cooperative SLAM, *Proc. of the 31st Chinese Control Conference*, Hefei, 4904–4909.
25. Zhu D., Sun X., Wang L., Liu B., Ji K. (2019), Mobile Robot SLAM Algorithm Based on Improved Firefly Particle Filter, *International Conference on Robots & Intelligent System (ICRIS)*, Haikou, China, 35–38.

Acknowledgements: The research work has been carried out within the framework of work No. WZ/WM-IIM/1/2019 and financed from the funds allocated for science by the Polish Ministry of Science and Higher Education.



## NEAR-RESONANT REGIMES OF A MOVING LOAD ON A PRE-STRESSED INCOMPRESSIBLE ELASTIC HALF-SPACE

Askar KUDAIBERGENOV\*, Askat KUDAIBERGENOV\*, Danila PRIKAZCHIKOV\*\*,\*\*\*

\*Department of Mathematical and Computer Modelling, Faculty of Mechanics and Mathematics,  
 Al-Farabi Kazakh National University, 71 Al-Farabi Ave., 050040, Almaty, Kazakhstan

\*\*School of Computing and Mathematics, Keele University, Keele, Staffordshire, ST5 5BG, UK

\*\*\*Institute for Problems in Mechanical Engineering RAS, 61 Bolshoy Pr., Saint-Petersburg, 199178, Russia

[askar.kudaibergenov@kaznu.kz](mailto:askar.kudaibergenov@kaznu.kz), [askat.kudaibergenov@kaznu.kz](mailto:askat.kudaibergenov@kaznu.kz), [d.prikazchikov@keele.ac.uk](mailto:d.prikazchikov@keele.ac.uk)

received 15 October 2020, revised 14 April 2021, accepted 19 April 2021

**Abstract:** The article is concerned with the analysis of the problem for a concentrated line load moving at a constant speed along the surface of a pre-stressed, incompressible, isotropic elastic half-space, within the framework of the plane-strain assumption. The focus is on the near-critical regimes, when the speed of the load is close to that of the surface wave. Both steady-state and transient regimes are considered. Implementation of the hyperbolic–elliptic asymptotic formulation for the surface wave field allows explicit approximate solution for displacement components expressed in terms of the elementary functions, highlighting the resonant nature of the surface wave. Numerical illustrations of the solutions are presented for several material models.

**Key words:** moving load, incompressible, pre-stress, asymptotic

### 1. INTRODUCTION

Moving loads on an elastic half-space have been the subject of numerous investigations, motivated by important engineering applications related to ground vibrations caused by moving transport vehicles; for example, refer to studies by Krylov (1996) and Cao et al. (2012). In the classical contribution of Cole and Huth (1958), a steady-state solution for an elastic half-plane subject to a moving load was obtained. It is worth mentioning that the resonant nature of the Rayleigh wave may have been noticed in this early article, see also the study by Goldstein (1965). A substantial part of consideration for moving loads is focused on steady-state regimes, refer e.g., recent results for porous anisotropic half-space by Wang et al. (2021) and the study for a thermoelastic half-space with double porosity by Kumar and Vohra (2020). We also note the articles dealing with time-harmonic moving loads; refer to studies by Lefeuve-Mesgouez et al. (2000) and Sun et al. (2019), and interesting aspects of transition when surface load moves over the interface of two elastic materials; refer to the study by van Dalen et al. (2015). There are relatively few treatments of transient modes in moving load problems, including early works (Payton, 1967; Gakenheimer and Miklowitz, 1969) and also more recent contributions (de Hoop, 2002; Kaplunov et al., 2010b). It is known that an analysis of transient dynamics is generally non-trivial, often requiring a numerical approach; refer to studies by Bratov (2011) and Smirnov et al. (2012). We also mention active studies of moving loads on elastic structures, for example refer to a textbook (Fryba, 1999) and references therein, as well as recent works in studies by Dimetrovová (2017), Wang et al. (2020) and Lu et al. (2020).

This article relies on a recent approach to near-resonant regimes of the moving load on an elastic half-space, originating from

the hyperbolic–elliptic models for surface waves; refer to the study by Kaplunov and Prikazchikov (2017). Models consist of elliptic equations associated with decay into the interior, along with hyperbolic equations on the surface governing wave propagation. This methodology has allowed a number of explicit approximate solutions of moving load problems; refer to studies by Kaplunov et al. (2010a), Kaplunov et al. (2013), Erbaş et al. (2017), and Ege et al. (2017). The advantage of this approach is related to the representation of the surface wave field in terms of a single harmonic function, providing reduction of the vector problem of elastodynamics to a scalar formulation. Recent developments in this area include the incorporation of effects of anisotropy (Fu et al., 2020), a refined second-order model (Wootton et al., 2020), explicit formulations for seismic meta-surfaces in the form of an array of resonators attached to the surface (Ege et al., 2018; Wootton et al., 2019) and formulations for surface wave on a coated half-space with non-classical boundary conditions (Kaplunov et al., 2019).

The hyperbolic–elliptic plane-strain model for surface wave on a pre-stressed incompressible elastic half-space has been derived in the study by Khajiyeva et al. (2018), allowing a scalar formulation for the surface wave field induced by prescribed surface stresses. In this work, we implement these results to analyse the near-critical regimes for the line force moving at a constant speed along the surface. Both steady-state and transient problems are considered. As a result, explicit expressions for the displacement field are obtained in terms of elementary functions, confirming the resonant nature of surface wave speed. In case of transient displacements, distinction between the sub-critical, super-critical and resonant regimes follows immediately from the analysis on the surface. Then, using Poisson's formula, solution is restored over the interior. Consideration of large time limit allows approxima-

tions for the components of rigid body motion. The obtained results are illustrated numerically for several material models, including the neo-Hookean, Gent, and Gent–Gent strain–energy functions.

## 2. STATEMENT OF THE PROBLEM

Consider a homogeneous incompressible elastic body with an initial state  $B_0$  in the domain  $X_2 \geq 0$ . Under the action of a homogeneous static deformation  $x_i = x_i(X_A)$ , the body transforms to a finitely deformed equilibrium state  $B_e$ , which corresponds to a half-space  $X_2 \geq 0$ , and after superimposing infinitesimal time-dependent motion  $u_i(x_j, t)$ , it moves to the current state  $B_t$  with the position vector  $\bar{x}_i(X_A, t)$  given by:

$$\bar{x}_i(X_A, t) = x_i(X_A) + u_i(x_j, t). \quad (1)$$

The equations provided below address the plane-strain problem, for which  $u_3 = 0$  and  $u_1 = u_1(x_1, x_2, t)$ ,  $u_2 = u_2(x_1, x_2, t)$ , giving the following coupled equations of incremental motion:

$$\begin{aligned} A_{1111} \frac{\partial^2 u_1}{\partial x_1^2} + (A_{1122} + A_{1221}) \frac{\partial^2 u_2}{\partial x_1 \partial x_2} + A_{2121} \frac{\partial^2 u_1}{\partial x_2^2} - \frac{\partial p_t}{\partial x_1} &= \rho \frac{\partial^2 u_1}{\partial t^2}, \\ A_{1212} \frac{\partial^2 u_2}{\partial x_1^2} + (A_{1122} + A_{1221}) \frac{\partial^2 u_1}{\partial x_1 \partial x_2} + A_{2222} \frac{\partial^2 u_2}{\partial x_2^2} - \frac{\partial p_t}{\partial x_2} &= \rho \frac{\partial^2 u_2}{\partial t^2}, \end{aligned} \quad (2)$$

where  $A_{ijkl}$  are the components of the fourth-order elasticity tensor (Ogden, 1984),  $\rho$  is mass density and  $p_t$  is the time-dependent incremental component of pressure associated with the incompressibility constraint whose linearised measure is given by:

$$\frac{\partial u_1}{\partial x_1} + \frac{\partial u_2}{\partial x_2} = 0. \quad (3)$$

In this article, we focus on studying the effect of a vertical load, represented as a concentrated line force moving at a constant speed  $v$ , on the pre-stressed elastic half-space (refer Fig. 1). Then, the boundary conditions on the surface  $x_2 = 0$  are given in the following form:

$$\begin{aligned} A_{2121} \frac{\partial u_1}{\partial x_2} + (A_{1221} + \bar{p}) \frac{\partial u_2}{\partial x_1} &= 0, \\ A_{1122} \frac{\partial u_1}{\partial x_1} + (A_{2222} + \bar{p}) \frac{\partial u_2}{\partial x_2} - p_t &= P_0 \delta(x_1 - vt), \end{aligned} \quad (4)$$

where  $\bar{p} = A_{2121} - A_{1221} - \sigma_2$  is static pressure in the equilibrium state  $B_e$ ,  $\sigma_2$  is the normal Cauchy stress component,  $\delta$  is the Dirac delta function and  $P_0$  is the amplitude.

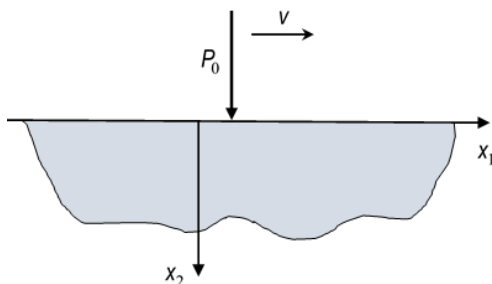


Fig. 1. Pre-stressed elastic half-space under the effect of a moving load

We consider the near-resonant regime, when the speed of the moving load is close to surface wave speed, thus the contribution of surface wave dominates over that of the bulk waves.

Introducing the auxiliary harmonic function  $\psi_1$  [see Khajiyeva et al. (2018) for details], the displacements may be expressed as follows:

$$\begin{aligned} u_1(x_1, x_2, t) &= \frac{\partial \psi_1(x_1, k_1 x_2, t)}{\partial x_2} + \vartheta \frac{\partial \psi_1(x_1, k_2 x_2, t)}{\partial x_2}, \\ u_2(x_1, x_2, t) &= -\frac{\partial \psi_1(x_1, k_1 x_2, t)}{\partial x_1} - \vartheta \frac{\partial \psi_1(x_1, k_2 x_2, t)}{\partial x_1}, \end{aligned} \quad (5)$$

where  $\vartheta = \frac{\gamma(k_1^2 + 1) - \sigma_2}{\gamma(k_2^2 + 1) - \sigma_2}$ , and  $k_1, k_2$  are related by:

$$k_1^2 + k_2^2 = \frac{2\beta - \rho c_R^2}{\gamma}, \quad k_1^2 k_2^2 = \frac{\alpha - \rho c_R^2}{\gamma}, \quad (6)$$

With:

$$\begin{aligned} \alpha &= A_{1212}, \quad 2\beta = A_{1111} + A_{2222} - 2(A_{1122} + A_{1221}), \\ \gamma &= A_{2121}, \end{aligned}$$

and  $c_R$  denoting surface wave speed, being the solution of

$$\gamma(\alpha - \rho c_R^2) + (2\beta + 2\gamma - 2\sigma_2 - \rho c_R^2) \sqrt{\gamma(\alpha - \rho c_R^2)} = (\gamma - \sigma_2)^2,$$

refer to the study by Dowaikh and Ogden (1990).

The approximate formulation of the original problem in elasticity as defined in Eqs (2)–(4), oriented towards the surface wave field, has been developed in the study by Khajiyeva et al. (2018), reducing the vector problem in elasticity to a scalar problem for the elliptic equation in respect of the potential  $\psi_1$ . The methodology of the derivation relies on the slow-time perturbation procedure, extending the previous results for isotropic elasticity; see Kaplunov and Prikazchikov (2017). The resulting hyperbolic–elliptic model for surface wave field in a pre-stressed incompressible elastic half-space excited by the vertical surface loading  $f_2 = f_2(x_1, t)$  is formulated in terms of the potential  $\psi_1$  as an elliptic equation:

$$\frac{\partial^2 \psi_1}{\partial x_2^2} + k_1^2 \frac{\partial^2 \psi_1}{\partial x_1^2} = 0, \quad (7)$$

which is subject to the boundary condition on the surface, given by a hyperbolic equation [compare with formula (39) in the study by Khajiyeva et al. (2018)]

$$\frac{\partial^2 \psi_1}{\partial x_1^2} - \frac{1}{c_R^2} \frac{\partial^2 \psi_1}{\partial t^2} = -\frac{2a_{11}f_2^*}{c_R(a_{21}b_1 - a_{11}b_2)} \quad \text{at } x_2 = 0, \quad (8)$$

where:

$$\begin{aligned} a_{11} &= \gamma(k_1^2 + 1) - \sigma_2, \quad a_{21} \\ &= k_1(2\beta - \rho c_R^2 - \sigma_2 - \gamma(k_1^2 - 1)), \end{aligned}$$

$$f_2 = P_0 \delta(x_1 - vt), \quad b_1 = \frac{2\rho c_R}{k_2^2 - k_1^2} (k_1^2 - 1 - \vartheta(k_2^2 - 1)),$$

$$b_2 = g_1 + \vartheta g_2,$$

$$\begin{aligned} g_j &= \frac{\rho c_R(k_j^2 - 1)}{\gamma k_j(k_m^2 - k_j^2)} (2\beta - \rho c_R^2 - \sigma_2 + \gamma(1 - 3k_j^2)) \\ &\quad - 2k_j \rho c_R, \end{aligned}$$

$j, m = 1, 2$ ;  $j \neq m$  and the asterisk denotes the Hilbert integral transform. In the forthcoming section, we adapt this asymptotic formulation (7) and (8) to the considered moving load problem.

### 3. EXPLICIT STEADY-STATE SOLUTION FOR THE NEAR-RESONANT REGIME

For the sake of convenience, the asymptotic models (7) and (8) can be expressed in terms of the harmonic conjugate of  $\psi_1$ . The elliptic Eq. (7) becomes:

$$\frac{\partial^2 \psi_1^*}{\partial x_2^2} + k_1^2 \frac{\partial^2 \psi_1^*}{\partial x_1^2} = 0, \quad (9)$$

and the hyperbolic Eq. (8) is rewritten as:

$$\frac{\partial^2 \psi_1^*}{\partial x_1^2} - \frac{1}{c_R^2} \frac{\partial^2 \psi_1^*}{\partial t^2} = P_1 \delta(x_1 - vt) \quad \text{at } x_2 = 0, \quad (10)$$

$$\text{where } P_1 = \frac{2a_{11}P_0}{c_R(a_{21}b_1 - a_{11}b_2)}.$$

Now we consider the steady-state regime and introduce a moving coordinate, which can be represented as follows:

$$\xi = x_1 - vt. \quad (11)$$

Then, Eq. (10) takes the form—

$$\left(1 - \frac{v^2}{c_R^2}\right) \frac{\partial^2 \psi_1^*}{\partial \xi^2} = P_1 \delta(\xi). \quad (12)$$

On integrating the latter, we have—

$$\frac{\partial \psi_1^*}{\partial \xi} = -\frac{c_R^2 P_1}{v - v_+} \left(H(\xi) - \frac{1}{2}\right), \quad (13)$$

where the constant of integration is chosen according to the symmetry rule as it cannot be determined by considering the steady-state regime (Kaplunov and Prikazchikov, 2017), and  $v_{\pm} = v \pm c_R$ .

Hence, restoring the solution into the interior, we obtain—

$$\frac{\partial \psi_1^*(\xi, k_1 x_2)}{\partial \xi} = -\frac{c_R^2 P_1}{\pi v - v_+} \tan^{-1} \frac{\xi}{k_1 x_2}, \quad (14)$$

from which the harmonic conjugate function can be found as—

$$\frac{\partial \psi_1(\xi, k_1 x_2)}{\partial \xi} = \frac{c_R^2 P_1}{2\pi v - v_+} \ln(\xi^2 + k_1^2 x_2^2). \quad (15)$$

Thus, on substituting (14) and (15) into (5), the displacements  $u_1$  and  $u_2$  are given explicitly by:

$$u_1 = \frac{c_R^2 P_1}{\pi v - v_+} \left[ k_1 \tan^{-1} \frac{\xi}{k_1 x_2} + \vartheta k_2 \tan^{-1} \frac{\xi}{k_2 x_2} \right],$$

$$u_2 = -\frac{c_R^2 P_1}{2\pi v - v_+} [\ln(\xi^2 + k_1^2 x_2^2) + \vartheta \ln(\xi^2 + k_2^2 x_2^2)] \quad (16)$$

The resonant nature of surface wave speed is clearly observed from the solution available in Eq. (16).

### 4. TRANSIENT MOVING LOAD PROBLEM

Now let us consider a transient problem. Within this article, we rely on the approach presented in the study by Kaplunov et al. (2010a), with the solution of the hyperbolic Eq. (10) written as a convolution of the right-hand side with the fundamental solution, namely:

$$\psi_1^*(\xi, 0, t) = \frac{c_R P_1}{2} \int_0^t (H(\xi + v_- r) - H(\xi + v_+ r)) dr, \quad (17)$$

where  $H$  is the Heaviside function.

The form of the integral in (17) motivates separate study of

three regimes, including the sub-Rayleigh ( $v < c_R$ ), super-Rayleigh ( $v > c_R$ ) and the resonant one ( $v = c_R$ ).

Introducing  $\varphi = -\frac{2}{c_R P_1} \psi_1^*$  for convenience, we obtain for

a) sub-Rayleigh regime ( $v < c_R$ ):

$$\varphi(\xi, 0, t) = \begin{cases} \frac{\xi}{v_-} + t, & 0 \leq \xi < -v_- t, \\ \frac{\xi}{v_+} + t, & -v_+ t < \xi < 0, \\ 0, & \text{otherwise} \end{cases} \quad (18)$$

b) super-Rayleigh regime ( $v > c_R$ ):

$$\varphi(\xi, 0, t) = \begin{cases} \xi \left( \frac{1}{v_+} - \frac{1}{v_-} \right), & -v_- t \leq \xi \leq 0, \\ \frac{\xi}{v_+} + t, & -v_+ t < \xi < -v_- t, \\ 0, & \text{otherwise} \end{cases} \quad (19)$$

c) resonant regime ( $v = c_R$ ):

$$\varphi(\xi, 0, t) = \begin{cases} \frac{\xi}{2c_R} + t, & -2c_R t \leq \xi \leq 0, \\ 0, & \text{otherwise} \end{cases} \quad (20)$$

Now, once the solution has been found on the surface  $x_2 = 0$  in terms of the function  $\varphi$ , we can conduct the analysis with depth, i.e. restore the solution over the interior of the half-space  $x_2 > 0$ . Using the elliptic Eq. (9) and applying Poisson's formula, the potential  $\psi_1^*$  is expressed as

$$\psi_1^*(\xi, k_1 x_2, t) = \frac{1}{\pi} \int_{-\infty}^{+\infty} \frac{k_1 x_2}{(r - \xi)^2 + k_1^2 x_2^2} \psi_1^*(r, 0, t) dr. \quad (21)$$

Let us once again present the results in sequence for all three considered regimes.

#### 4.1. Sub-Rayleigh regime

On substituting Eq. (18) into Eq. (21), after integration we get

$$\psi_1^*(\xi, k_1 x_2, t) = \frac{1}{\pi} \int_{-\infty}^{+\infty} \frac{k_1 x_2}{(r - \xi)^2 + k_1^2 x_2^2} \psi_1^*(r, 0, t) dr. \quad (21)$$

where

$$h(\xi, k_1 x_2, \xi_i) = \frac{k_1 x_2}{2} \ln \frac{(\xi - \xi_i)^2 + k_1^2 x_2^2}{\xi^2 + k_1^2 x_2^2} + \xi \tan^{-1} \frac{\xi}{k_1 x_2} - (\xi - \xi_i) \tan^{-1} \frac{\xi - \xi_i}{k_1 x_2} \quad (i = 1, 2),$$

$$\text{and } \xi_1 = -v_- t, \quad \xi_2 = -v_+ t.$$

Displacements (5) in terms of  $\psi_1^*$  take the following form

$$u_1 = -k_1 \frac{\partial \psi_1^*(\xi, k_1 x_2, t)}{\partial \xi} - \vartheta k_2 \frac{\partial \psi_1^*(\xi, k_2 x_2, t)}{\partial \xi},$$

$$u_2 = -\frac{1}{k_1} \frac{\partial \psi_1^*(\xi, k_1 x_2, t)}{\partial x_2} - \frac{\vartheta}{k_2} \frac{\partial \psi_1^*(\xi, k_2 x_2, t)}{\partial x_2}. \quad (23)$$

Then, on substituting Eq. (22) into Eq. (23), the transient displacements are written explicitly as:

$$u_1 = \frac{c_R^2 P_1}{\pi v - v_+} \left[ k_1 \tan^{-1} \frac{\xi}{k_1 x_2} + \vartheta k_2 \tan^{-1} \frac{\xi}{k_2 x_2} \right] + \frac{c_R P_1}{2\pi v_+} \left[ k_1 \tan^{-1} \frac{\xi - \xi_2}{k_1 x_2} + \vartheta k_2 \tan^{-1} \frac{\xi - \xi_2}{k_2 x_2} \right] - \frac{c_R P_1}{2\pi v_-} \left[ k_1 \tan^{-1} \frac{\xi - \xi_1}{k_1 x_2} + \vartheta k_2 \tan^{-1} \frac{\xi - \xi_1}{k_2 x_2} \right], \quad (24)$$

$$u_2 = -\frac{c_R P_1}{4\pi v_+} \left[ \ln \frac{(\xi - \xi_2)^2 + k_1^2 x_2^2}{\xi^2 + k_1^2 x_2^2} + \vartheta \ln \frac{(\xi - \xi_2)^2 + k_2^2 x_2^2}{\xi^2 + k_2^2 x_2^2} \right] + \frac{c_R P_1}{4\pi v_-} \left[ \ln \frac{(\xi - \xi_1)^2 + k_1^2 x_2^2}{\xi^2 + k_1^2 x_2^2} + \vartheta \ln \frac{(\xi - \xi_1)^2 + k_2^2 x_2^2}{\xi^2 + k_2^2 x_2^2} \right]. \quad (25)$$

We represent Eq. (24) as:

$$u_1 = u_1^{st}(\xi, x_2) + u_1^{r0}, \quad (26)$$

where  $u_1^{st}$  corresponds to the steady-state displacement (16<sub>1</sub>), and:

$$u_1^{r0} = \frac{c_R P_1 v(k_1 + \vartheta k_2)}{2v_- v_+} \quad (27)$$

is associated with the rigid body motion of the half-space, determined from the analysis of the limiting behaviour of displacements as  $t \rightarrow \infty$ .

Similarly, equation (25) can be reduced to

$$u_2 = u_2^{st}(\xi, x_2) + u_2^{r0} + u_2^{r1} \ln t, \quad (28)$$

where  $u_2^{st}$  corresponds to formula (16<sub>2</sub>), and

$$u_2^{r0} = -\frac{c_R P_1 (1 + \vartheta)}{2\pi} \left[ \frac{\ln v_+}{v_+} - \frac{\ln |v_-|}{v_-} \right],$$

$$u_2^{r1} = \frac{c_R^2 P_1 (1 + \vartheta)}{\pi v_- v_+}. \quad (29)$$

Thus, explicit expressions for rigid body motion have been obtained. It also follows from Eq. (29) that the vertical rigid body motion had a logarithmic growth in time, which is consistent with the previous results for isotropic elasticity in (Kaplunov et al., 2010a).

## 4.2. Super-Rayleigh regime

On substituting Eq. (19) into Eq. (21) and performing straightforward manipulations, we deduce the following equation:

$$\psi_1^*(\xi, k_1 x_2, t) = -\frac{c_R P_1}{2\pi} \left[ \frac{2c_R}{v_- v_+} \left( \frac{k_1 x_2}{2} \ln \frac{(\xi - \xi_1)^2 + k_1^2 x_2^2}{\xi^2 + k_1^2 x_2^2} + \xi \tan^{-1} \frac{\xi}{k_1 x_2} - \xi \tan^{-1} \frac{\xi - \xi_1}{k_1 x_2} \right) - \frac{1}{c_R + v} \left( \frac{k_1 x_2}{2} \ln \frac{(\xi - \xi_2)^2 + k_1^2 x_2^2}{(\xi - \xi_1)^2 + k_1^2 x_2^2} + (\xi - \xi_2) \tan^{-1} \frac{\xi - \xi_1}{k_1 x_2} - (\xi - \xi_2) \tan^{-1} \frac{\xi - \xi_2}{k_1 x_2} \right) \right]. \quad (30)$$

Then, from Eq. (23), the displacements  $u_1$  and  $u_2$  are obtained, coinciding with those for the sub-Rayleigh regime, namely Eqs (24) and (25). Study of the limiting behaviour of both displacements also gives the same structure as in Eqs (26)–(29), except for  $u_1^{r0}$  that now is determined by—

$$u_1^{r0} = -\frac{c_R^2 P_1 (k_1 + \vartheta k_2)}{2v_- v_+}. \quad (31)$$

## 4.3. Resonant regime

Here, we study the case when the speed of the moving load coincides with the surface wave speed. Taking into account Eq. (20), the potential  $\psi_1^*$  is found as:

$$\psi_1^*(\xi, k_1 x_2, t) = \frac{P_1}{4\pi} \left[ \frac{k_1 x_2}{2} \ln \frac{(\xi + 2c_R t)^2 + k_1^2 x_2^2}{\xi^2 + k_1^2 x_2^2} + (\xi + 2c_R t) \left( \tan^{-1} \frac{\xi}{k_1 x_2} - \tan^{-1} \frac{\xi + 2c_R t}{k_1 x_2} \right) \right]. \quad (32)$$

Substituting (32) into (23), we have:

$$u_1 = -\frac{c_R P_1 x_2 t}{2\pi} \left[ \frac{k_1^2}{\xi^2 + k_1^2 x_2^2} + \frac{\vartheta k_2^2}{\xi^2 + k_2^2 x_2^2} \right] - \frac{P_1 k_1}{4\pi} \left[ \tan^{-1} \frac{\xi}{k_1 x_2} - \tan^{-1} \frac{\xi + 2c_R t}{k_1 x_2} \right] - \frac{P_1 \vartheta k_2}{4\pi} \left[ \tan^{-1} \frac{\xi}{k_2 x_2} - \tan^{-1} \frac{\xi + 2c_R t}{k_2 x_2} \right], \quad (33)$$

$$u_2 = \frac{c_R P_1 \xi t}{2\pi} \left[ \frac{1}{\xi^2 + k_1^2 x_2^2} + \frac{\vartheta}{\xi^2 + k_2^2 x_2^2} \right] - \frac{P_1}{8\pi} \left[ \ln \frac{(\xi + 2c_R t)^2 + k_1^2 x_2^2}{\xi^2 + k_1^2 x_2^2} + \vartheta \ln \frac{(\xi + 2c_R t)^2 + k_2^2 x_2^2}{\xi^2 + k_2^2 x_2^2} \right]. \quad (34)$$

The limiting behavior of displacements as  $t \rightarrow \infty$  for resonant case gives

$$u_1 = -\frac{c_R P_1 x_2 t}{2\pi} \left[ \frac{k_1^2}{\xi^2 + k_1^2 x_2^2} + \frac{\vartheta k_2^2}{\xi^2 + k_2^2 x_2^2} \right], \quad (35)$$

and:

$$u_2 = \frac{c_R P_1 \xi t}{2\pi} \left[ \frac{1}{\xi^2 + k_1^2 x_2^2} + \frac{\vartheta}{\xi^2 + k_2^2 x_2^2} \right] - \frac{P_1 (1 + \vartheta)}{4\pi} \ln(2c_R t). \quad (36)$$

## 5. NUMERICAL ILLUSTRATIONS

First, let us illustrate the obtained steady-state solution available in Eq. (16). Three forms of the strain–energy function are considered in the following, namely the neo-Hookean, Gent, and Gent–Gent models, which are typically used for modelling rubber-like materials.

The well-known neo-Hookean strain–energy function is written as:

$$W = \frac{\mu}{2} (I_1 - 3), \quad (37)$$

where  $\mu$  is the ground-state shear modulus, and  $I_1$  is given by:

$$I_1 = \lambda_1^2 + \lambda_2^2 + \lambda_3^2, \quad (38)$$

where  $\lambda_i$  ( $i = \overline{1,3}$ ) are the principal stretches of the underlying deformation, related by an incompressibility condition  $\lambda_1 \lambda_2 \lambda_3 = 1$  [see Dowdikh and Ogden (1990) for more details].

Consider also extensions of the neo-Hookean model, including the Gent strain–energy function (Gent, 1996)

$$W = -\frac{\mu}{2} J_m \ln \left( 1 - \frac{I_1 - 3}{J_m} \right), \quad (39)$$

where  $J_m$  is a material constant characterising material extensibility and the shear modulus  $\mu = \mu_0 + \frac{2C_2}{3}$  with  $C_2$  denoting the material constant, along with its more advanced version usually referred to as the Gent–Gent material model (Pucci and Saccomandi, 2002) defined by

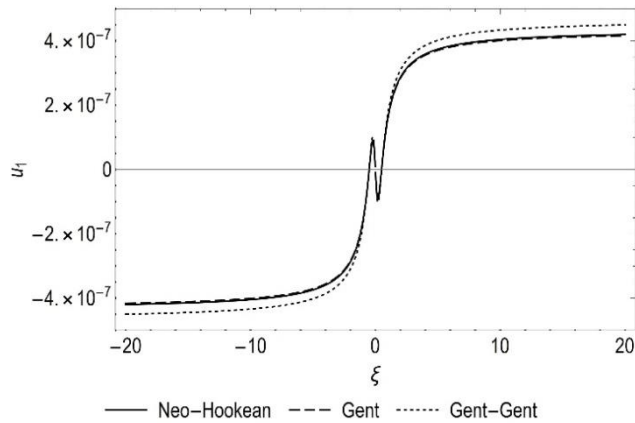
$$W = -\frac{\mu_0}{2} J_m \ln \left( 1 - \frac{I_1 - 3}{J_m} \right) + C_2 \ln \left( \frac{I_2}{3} \right), \quad (40)$$

where  $I_1$  is given by (38), and  $I_2 = \lambda_1^{-2} + \lambda_2^{-2} + \lambda_3^{-2}$ , see also a recent contribution by (Zhou et al., 2018).

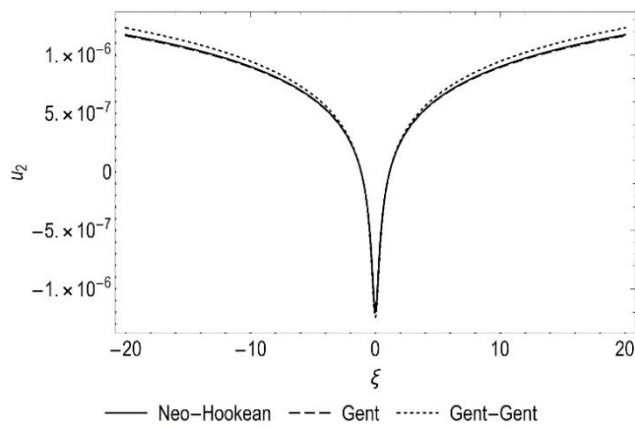
Figs. 2, 3 demonstrate the computation results for different forms of the strain–energy function at the depth  $x_2 = 0.5$ . The system parameters are chosen as follows:  $\mu_0 = 0.2853$  MPa,  $C_2 = 0.1898$  MPa,  $J_m = 88.43$  (according to (Zhou et al., 2018)),  $\rho = 1522$  kg/m<sup>3</sup>,  $v = 0.8 c_R$ ,  $P_0 = 1$ ,  $\lambda_1 = 1.25$ ,  $\lambda_2 = \lambda_1^{-1}$ ,  $\lambda_3 = 1$ . It is also assumed that a parameter  $Z = 0$ , which is used for calculating the normal Cauchy stress  $\sigma_2$  (Dowdikh and Ogden, 1990),

$$\sigma_2 = \gamma - \sqrt{\gamma \alpha} + Z \sqrt{2\sqrt{\gamma \alpha}(\beta + \sqrt{\gamma \alpha})}, \quad -1 \leq Z \leq 1, \quad (41)$$

Thus, the surface wave has a non-zero velocity and is localised.



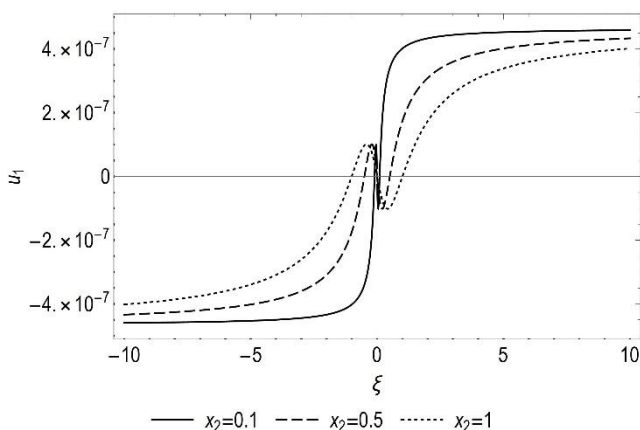
**Fig. 2.** Horizontal displacement  $u_1$  for the neo-Hookean, Gent and Gent-Gent material models



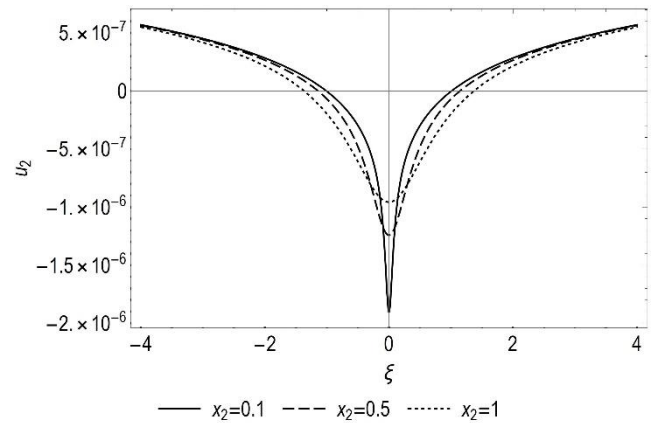
**Fig. 3.** Vertical displacement  $u_2$  for the neo-Hookean, Gent and Gent-Gent material models

As can be seen from Figs 2 and 3, the neo-Hookean and Gent material models give almost identical results for both displacements  $u_1$  and  $u_2$ , whereas using the Gent-Gent model results in higher values of the displacement amplitudes with increasing  $\xi$ . In what follows, we use the Gent-Gent model, since it seemingly provides a better agreement with experimental data, as demonstrated in a study by Zhou et al. (2018).

Variation of the amplitude of the surface displacements  $u_1$  and  $u_2$  on the moving coordinate is illustrated in Figs 4 and 5 for several values of the transverse variable  $x_2$ .



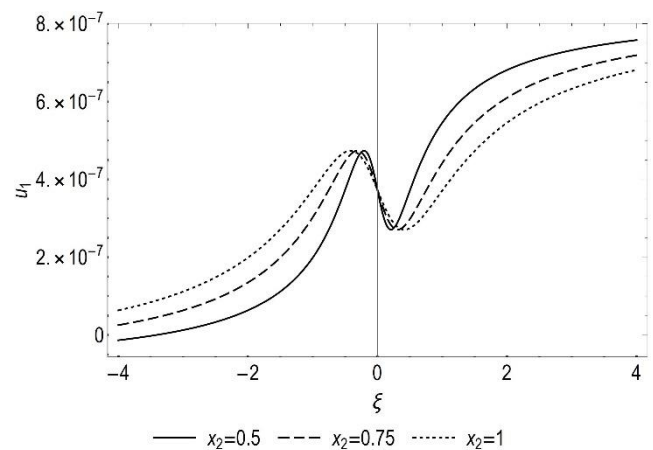
**Fig. 4.** Dependence of displacement  $u_1$  on the moving coordinate  $\xi$  for different values of  $x_2$



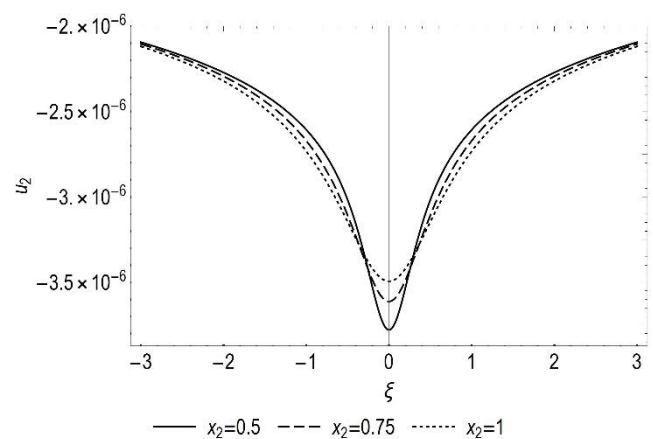
**Fig. 5.** Dependence of displacement  $u_2$  on the moving coordinate  $\xi$  for different values of  $x_2$

Predictably, the obtained graphs (Figs 4 and 5) indicate smoothing of displacement profiles under the moving load with increase in depth.

To present the numerical results for the transient moving load problem, the Gent-Gent model [Eq. (40)] is used for the same material parameters as before. The speed of the moving load for various regimes is taken as  $v = 0.8 c_R$ ,  $v = 1.2 c_R$  and  $v = c_R$  for the sub-Rayleigh, super-Rayleigh and resonant regimes, respectively (Figs 6–11).



**Fig. 6.** The sub-Rayleigh transient displacement  $u_1$  for different values of  $x_2$

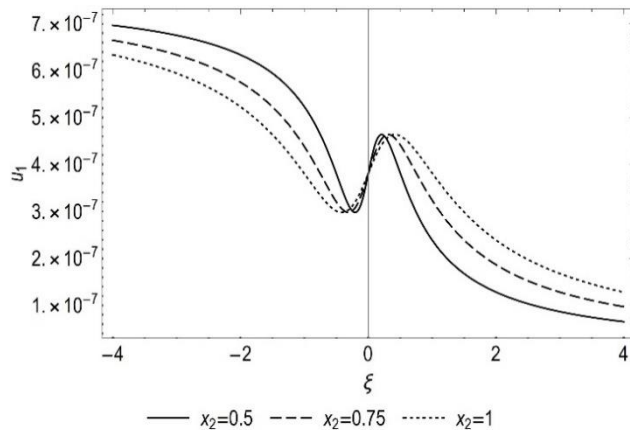


**Fig. 7.** The sub-Rayleigh transient displacement  $u_2$  for different values of  $x_2$

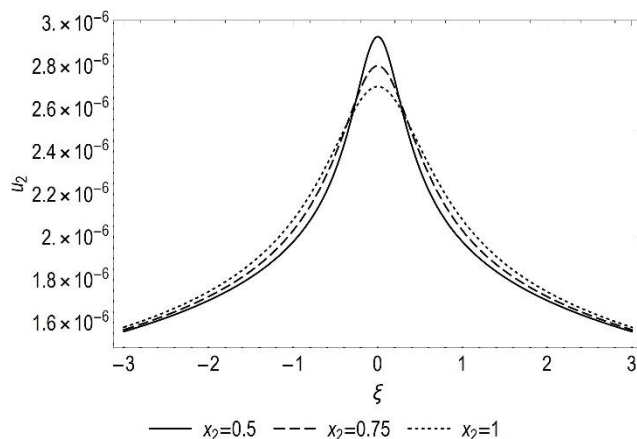


Figs 6 and 7 demonstrate the sub-Rayleigh transient displacements  $u_1$  and  $u_2$ ; Figs. 8 and 9 represent the super-Rayleigh transient displacements, see Eqs (24) and (25); and Figs. 10 and 11 correspond to the resonant transient displacements Eqs (33) and (34), depending on the values of the vertical coordinate  $x_2$ .

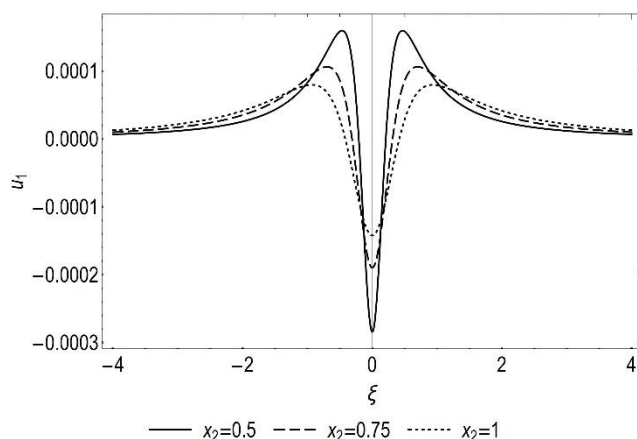
It is emphasised that the obtained shapes of displacements are typical for a broad range of deformations, with qualitatively similar behaviour occurring for the non-deformed linear isotropic case as well, when  $\lambda_1 = \lambda_2 = \lambda_3 = 1$ .



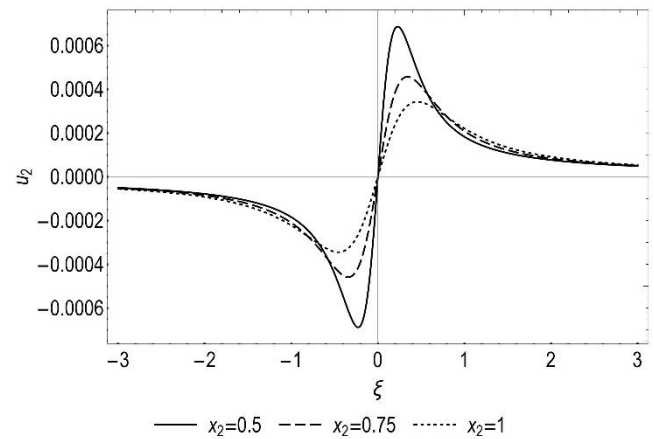
**Fig. 8.** The super-Rayleigh transient displacement  $u_1$  for different values of  $x_2$



**Fig. 9.** The super-Rayleigh transient displacement  $u_2$  for different values of  $x_2$



**Fig. 10.** The resonant transient displacement  $u_1$  for different values of  $x_2$



**Fig. 11.** The resonant transient displacement  $u_2$  for different values of  $x_2$

It should be noted that the accuracy of the approximate results within the model has been discussed in a study by (Kaplunov and Prikazhnikov, 2017; Sect. 4.3.1), where it was shown that for a wide class of loads, the asymptotic formulation captures the contribution of the Rayleigh poles. Moreover, in case of transient problem, as shown in a study by Kaplunov et al. (2010a), the near-resonant solution is valid for large times when the effect of the body waves becomes negligible. Moreover, comparison of exact and approximate solutions revealed a wide range of speeds, in which the approximation performs at a reasonable accuracy [Fig. 8 in Kaplunov et al. (2010a)].

## 6. CONCLUSION

The near-resonant regimes of the steady-state moving load problem on a pre-stressed, incompressible elastic half-space have been studied. Implementation of the hyperbolic-elliptic model for surface wave allowed explicit solutions for the displacement components. Illustrations in Figs. 2 and 3 revealed some possible similarities between the neo-Hookean, Gent, and Gent-Gent material models. The consideration has then been extended to transient problem, allowing an elegant approximate solution in terms of elementary functions, which makes it convenient for further analysis, including the limiting behaviour for large time, providing explicit results for the components of rigid body motion.

Various extensions of the approach include derivation of 3D asymptotic models in pre-stressed media. Although a straightforward explicit approach could be cumbersome algebraically, there is a chance of more elegant representation through Stroh formalism, in line with results reported recently in a study by Fu et al. (2020). It is worth noting that adding vertical inhomogeneity will lead to smoothing of surface discontinuities; for more details refer to a study by Erbaş et al. (2017). Finally, we note that it is also possible to extend the methodology to composite models for elastic layers (Erbaş et al., 2018; Erbaş et al., 2019), as well as to consider the dynamics of a pre-stressed half-space with cavities (Alekseeva and Ukrainets, 2009) and crack propagation (Mishuris et al., 2012; Gourgiotis and Piccolroaz, 2014).

## REFERENCES

1. **Alekseeva L.A., Ukrainets V.N.** (2009), Dynamics of an elastic half-space with a reinforced cylindrical cavity under moving loads, *Int. Appl. Mech.*, 45(9), 981-990.

2. **Bratov V.** (2011), Incubation time fracture criterion for FEM simulations, *Acta Mech. Sin.*, 27(4), 541.
3. **Cao Y., Xia H., Li Z.** (2012), A semi-analytical/FEM model for predicting ground vibrations induced by high-speed train through continuous girder bridge, *J. Mech. Sci. Technol.*, 26, 2485-2496.
4. **Cole J., Huth J.** (1958), Stresses produced in a half plane by moving loads, *J. Appl. Mech.*, 25, 433-436.
5. **de Hoop A.T.** (2002), The moving-load problem in soil dynamics – the vertical displacement approximation, *Wave Motion*, 36(4), 335-346.
6. **Dimitrovová Z.** (2017), Analysis of the critical velocity of a load moving on a beam supported by a finite depth foundation, *Int. J. Solids Struct.*, 122, 128-147.
7. **Dowaikh M.A., Ogden R.W.** (1990), On surface waves and deformations in a pre-stressed incompressible elastic solid, *IMA J. Appl. Math.*, 44, 261-284.
8. **Ege N., Erbaş B., Kaplunov J., Wootton P.** (2018), Approximate analysis of surface wave-structure interaction, *J. Mech. Mater. Struct.*, 13(3), 297-309.
9. **Ege N., Şahin O., Erbaş B.** (2017), Response of a 3D elastic half-space to a distributed moving load, *Hacet J. Math. Stat.*, 46(5), 817-828.
10. **Erbaş B., Kaplunov J., Nolde E., Palsü M.** (2018), Composite wave models for elastic plates, *P. Roy. Soc. A-Math. Phys.*, 474(2214), 1-16.
11. **Erbaş B., Kaplunov J., Palsü M.** (2019), A composite hyperbolic equation for plate extension, *Mech. Res. Commun.*, 99, 64-67.
12. **Erbaş B., Kaplunov J., Prikazchikov D.A., Şahin O.** (2017), The near-resonant regimes of a moving load in a three-dimensional problem for a coated elastic half-space, *Math. Mech. Solids*, 22(1), 89-100.
13. **Fryba L.** (1999), *Vibration of solids and structures under moving loads*, 3rd ed, Thomas Telford, London.
14. **Fu Y., Kaplunov J., Prikazchikov D.** (2020), Reduced model for the surface dynamics of a generally anisotropic elastic half-space, *P. Roy. Soc. A-Math. Phys.*, 476(2234), 1-19.
15. **Gakenheimer D.C., Miklowitz J.** (1969), Transient excitation of an elastic half space by a point load traveling on the surface, *J. Appl. Mech.*, 36(3), 505-515.
16. **Gent A.N.** (1996), A new constitutive relation for rubber, *Rubber Chem. Technol.*, 69(1), 59-61.
17. **Goldstein R.V.** (1965), Rayleigh waves and resonance phenomena in elastic bodies, *J. Appl. Math. Mech. (PMM)*, 29(3), 516-525.
18. **Gouriotis P.A., Piccolroaz A.** (2014), Steady-state propagation of a mode II crack in couple stress elasticity, *Int. J. Fract.*, 188(2), 119-145.
19. **Kaplunov J., Nolde E., Prikazchikov D.A.** (2010a), A revisit to the moving load problem using an asymptotic model for the Rayleigh wave, *Wave Motion*, 47, 440-451.
20. **Kaplunov J., Prikazchikov D., Sultanova L.** (2019), Rayleigh-type waves on a coated elastic half-space with a clamped surface, *Phil. Trans. Roy. Soc. A*, 377(2156), 1-15.
21. **Kaplunov J., Prikazchikov D.A.** (2017), Asymptotic theory for Rayleigh and Rayleigh-type waves, *Adv. Appl. Mech.*, 50, 1-106.
22. **Kaplunov J., Prikazchikov D.A., Erbaş B., Şahin O.** (2013), On a 3D moving load problem for an elastic half space, *Wave Motion*, 50(8), 1229-1238.
23. **Kaplunov J., Voloshin V., Rawlins A.D.** (2010b), Uniform asymptotic behaviour of integrals of Bessel functions with a large parameter in the argument, *Quart. J. Mech. Appl. Math.*, 63(1), 57-72.
24. **Khajiyeva L.A., Prikazchikov D.A., Prikazchikova L.A.** (2018), Hyperbolic-elliptic model for surface wave in a pre-stressed incompressible elastic half-space, *Mech. Res. Commun.*, 92, 49-53.
25. **Krylov V.V.** (1996), Vibrational impact of high-speed trains. I. Effect of track dynamics, *J. Acoust. Soc. Am.*, 100(5), 3121-3134.
26. **Kumar R., Vohra R.** (2020), Steady state response due to moving load in thermoelastic material with double porosity, *Mater. Phys. Mech.*, 44(2), 172-185.
27. **Lefeuvre-Mesgouez G., Le Houédec D., Peplow A.T.** (2000), Ground vibration in the vicinity of a high-speed moving harmonic strip load, *J. Sound Vib.*, 231(5), 1289-1309.
28. **Lu T., Metrikine A.V., Steenbergen M.J.M.M.** (2020), The equivalent dynamic stiffness of a visco-elastic half-space in interaction with a periodically supported beam under a moving load, *Europ. J. Mech.-A/Solids*, 84, 104065.
29. **Mishuris G., Piccolroaz A., Radi E.** (2012), Steady-state propagation of a Mode III crack in couple stress elastic materials, *Int. J. Eng. Sci.*, 61, 112-128.
30. **Ogden R.W.** (1984), *Non-linear elastic deformations*, Dover, New York.
31. **Payton R.G.** (1967), Transient motion of an elastic half-space due to a moving surface line load, *Int. J. Eng. Sci.*, 5(1), 49-79.
32. **Pucci E., Saccomandi G.** (2002), A note on the Gent model for rubber-like materials, *Rubber Chem. Technol.*, 75(5), 839-852.
33. **Smirnov V., Petrov Yu.V., Bratov V.** (2012), Incubation time approach in rock fracture dynamics, *Sci. China Phys., Mech. Astr.*, 55(1), 78-85.
34. **Sun Z., Kasbergen C., Skarpas A., Anupam K., van Dalen K.N., Erkens S.M.** (2019), Dynamic analysis of layered systems under a moving harmonic rectangular load based on the spectral element method, *Int. J. Solids Struct.*, 180, 45-61.
35. **van Dalen K.N., Tsouvalas A., Metrikine A.V., Hoving J.S.** (2015), Transition radiation excited by a surface load that moves over the interface of two elastic layers, *Int. J. Solids Struct.*, 73, 99-112.
36. **Wang F., Han X., Ding T.** (2021), An anisotropic layered poroelastic half-space subjected to a moving point load, *Soil Dyn. Earth. Eng.*, 140, 106427.
37. **Wang Y., Zhou A., Fu T., Zhang W.** (2020), Transient response of a sandwich beam with functionally graded porous core traversed by a non-uniformly distributed moving mass, *Int. J. Mech. Mater. Design*, 16(3), 519-540.
38. **Wootton P.T., Kaplunov J., Colquitt D.J.** (2019), An asymptotic hyperbolic-elliptic model for flexural-seismic metasurfaces, *P. Roy. Soc. A-Math. Phys.*, 475(2227), 1-18.
39. **Wootton P.T., Kaplunov J., Prikazchikov D.** (2020), A second-order asymptotic model for Rayleigh waves on a linearly elastic half plane, *IMA J. Appl. Math.*, 85, 113-131.
40. **Zhou L., Wang S., Li L., Fu Y.** (2018), An evaluation of the Gent and Gent-Gent material models using inflation of a plane membrane, *Int. J. Mech. Sci.*, 146-147, 39-48.

Acknowledgements: Askar K and Askat K acknowledge support from the Ministry of Science and Education of the Republic of Kazakhstan (Grant No. AP05132743, 2018-2020). DP was supported by the Russian Science Foundation, Grant No. 20-11-20133 in the part on "Explicit steady-state solution for the near-resonant regime".

# SELF-ADAPTIVE ASYMMETRICAL ARTIFICIAL POTENTIAL FIELD APPROACH DEDICATED TO THE PROBLEM OF POSITION TRACKING BY NONHOLONOMIC UAVS IN WINDY ENVIRONMENTS

Cezary KOWNACKI\*

\*Department of Robotics and Mechatronics, Faculty of Mechanical Engineering, Białystok University of Technology,  
ul. Wiejska 45C, 15-351 Białystok, Poland

[c.kownacki@pb.edu.pl](mailto:c.kownacki@pb.edu.pl)

received 26 May 2020, revised 27 April 2021, accepted 30 April 2021

**Abstract:** Artificial potential fields (APFs) are a popular method of planning and controlling the path of robot movement, including unmanned aerial vehicles (UAVs). However, in the case of nonholonomic robots such as fixed-wing UAVs, the distribution of velocity vectors should be adapted to their limited manoeuvrability to ensure stable and precise position tracking. The previously proposed local asymmetrical potential field resolves this issue, but it is not effective in the case of windy environments, where the UAV is unable to maintain the desired position and drifts due to the wind drift effect. This is reflected in the growth of position error, which, similar to the steady-state error in the best case, is constant. To compensate for it, the asymmetrical potential field approach is modified by extending definitions of potential function gradient and velocity vector field (VVF) with elements based on the integral of position tracking error. In the case of wind drift, the value of this integral increases over time, and lengths and orientations of velocity vectors will also be changed. The work proves that redefining gradient and velocity vector as a function of position tracking error integrals allows for minimisation of the position tracking error caused by wind drift.

**Key words:** artificial potential field, asymmetrical potential field, position tracking, UAV, self-adaptive potential field

## 1. INTRODUCTION

The field of unmanned aerial vehicles (UAVs) is one of the most rapidly developing ones in the field of robotics. Intensive research on technology and algorithms applied in UAVs is making them more and more autonomous. However, there remains much work to be done on core topics such as obstacle avoidance, path planning or formation flight to make them fully autonomous. The major contribution of UAVs to military or civil applications belongs to unmanned multirotor vehicles, their main advantage being their capability of hovering. This makes it easier to control a flight path, especially in an urban environment with plenty of obstacles. Unfortunately, the endurance of multi-rotor flights is limited as a result of their low power efficiency. Missions of fixed-wing UAVs are longer, but due to their limited manoeuvrability as nonholonomic vehicles, it is more difficult to precisely control the flight path. This particularly concerns such applications as obstacle avoidance, path planning or formation flight under windy conditions.

Artificial potential field (APF) methods are a convenient way to implement precise and stable position control in applications of position guidance or obstacle avoidance, and this also applies in the case of UAVs (Frew et al., 2007). The main advantage of APF comes from the fact that potential functions are Lyapunov functions with local minimums. This ensures asymptotically stable control of robot position to achieve the desired shape of the path. Therefore, various approaches to APF are widely applied in algorithms dedicated to problems of obstacle avoidance discussed in Budiyo et al. (2015) and Nieuwenhuisen et al. (2013), path

planning methods with movement among obstacles described in Chen et al. (2016), Hatton and Choset (2011), Khuswendi et al. (2011), Mukherjee and Anderson (1993) and Nelson et al. (2007), formation flights presented in Barnes et al. (2007), Bennet and McInnes (2011), Bennet and McInnes (2008), Kokume and Uchiyama (2010), Kownacki and Ambroziak (2017), Nagao and Uchiyama (2014), Tobias et al. (2008), Suzuki and Uchiyama (2011) and Suzuki and Uchiyama (2010) or their combinations given in Cetin and Yilmaz (2016), Chen et al. (2015) and Mukherjee and Anderson (1993). Even the rules of birds flocking, i.e. repulsion and cohesion, which are applied in formation flights, can be considered implementations of APF (Kownacki and Oldziej, 2016; Viragh et al., 2014). APF precisely and clearly defines a relation between the velocity vector designating a specific guidance route and the actual position relative to other UAVs, obstacles or mission targets (Frew et al., 2007). As mentioned in Nagao and Uchiyama (2014), known APFs applied in the majority of articles concerning APF, also in those referred above, fail in the case of position tracking by nonholonomic vehicles. Typically, APF's definitions provide a symmetrical distribution of velocity vectors around their minimums. This, combined with nonholonomic constraints, leads to instability that manifests as violent changes of airspeed and heading angle (Frew et al., 2007; Kownacki and Ambroziak, 2017). This happens when a UAV is just near the point of tracked position and position tracking error decreases towards zero. Then, even small unintentional displacement produces a violent change of the desired heading. Violent changes of heading can be explained by the fact that it is usually calculated from the ratio of position differences on the x and y axes of a navigational coordinate frame and the arctangent

function. The varying ratio of distances on the x and y axes, from low values to high, occurring when both distance values oscillate around zero, results in significantly different values of angle according to the curve of arctangent.

The circular potential function based on a sigmoid function is one of the ideas meant to prevent these violent changes of heading values and achieve a circular loiter pattern tracked by the UAV. Its effectiveness is the result of the symmetrical gradient distribution on both sides of the circular flight pattern, attracting the UAV to its line (Frew et al., 2007; Nagao and Uchiyama, 2014). The flight pattern is a local minimum of the attractive potential function created as a combination of circular sigmoid functions. In turn, in work of Kownacki and Ambroziak (2017), the novel approach based on an asymmetrical artificial potential function (AAPF), defined in a local coordinate system, provides position tracking stability in the case of formation flights of nonholonomic fixed-wing UAVs. The definition of the asymmetrical potential function is used to create a velocity vector field (VVF), which guides a fixed-wing UAV in a way that smoothly aligns its heading and airspeed to the heading angle and airspeed of the tracked point. In the subsequent work (Kownacki and Ambroziak, 2019), the approach is modified by expanding it by a rotation mechanism of the VVF. It counteracts increments of tracking error during manoeuvres as the result of formation rotation when a UAV is behind the leader and the tracked position.

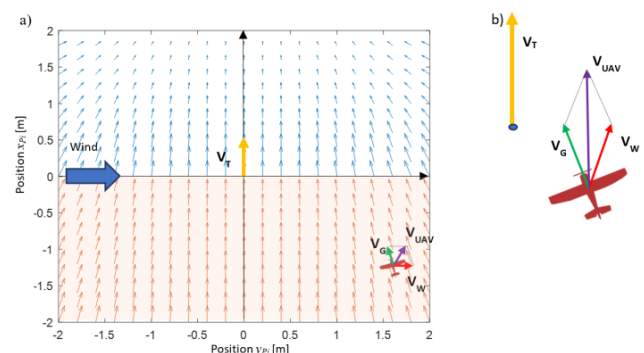
Unfortunately, none of the examples of application of artificial potential functions that are available in the literature account for external disturbances such as wind drift. A VVF is a geometrical representation of the relation between the expected direction of a UAV's movement and its positions relative to a reference point. In turn, wind treated as the movement of air mass with a constant velocity can be represented by a homogeneous VVF. Thus, combining the guidance VVF with the wind velocity vector field (WVVF) causes a UAV to drift from the desired position and its desired path of flight. The issue is especially important for nonholonomic UAVs. Therefore, this work proposes a self-adaptive asymmetrical potential function mechanism which prevents such drift error, having the meaning of the steady-state error. The effectiveness of the presented adaptation mechanism is proven by the numerical simulation results discussed in Section 5. The idea of the mechanism is to consider integrals of tracking errors in definitions of potential function gradient and VVF only if there is any constant movement of air mass causing wind drift. The slope of the potential function, spatial orientation and lengths of gradients and velocity vectors will be changing depending on wind drift incrementing the integrals' values. Therefore, the main contribution of this work is defining a new approach to the asymmetrical potential function from works of Kownacki and Ambroziak (2017) and Kownacki and Ambroziak (2019), which considers integrals of position tracking errors so as to minimise them in the case of wind drift effect.

The next part of the article is divided into four sections. The first one formulates the problem of wind drift increasing position tracking error and producing a steady-state error. The second section presents new definitions of potential function gradient and VVF, which are based on the asymmetrical potential function approach modified by a self-adaptive mechanism applying integrals of tracking error. In the third section, the results of numerical simulations compare responses to a step change of wind velocity in the cases of the proposed novel self-adaptive asymmetrical potential function approach and the previous approach from

Kownacki and Ambroziak (2019). The conclusions and discussion are in the final section.

## 2. PROBLEM FORMULATION

Flight control based on artificial potential functions is convenient as it transforms geometrical relations between a UAV's position and characteristic mission points into a VVF which accomplishes predefined rules of guidance, e.g. obstacle avoidance. Velocity vectors implementing guidance rules are used to calculate navigational parameters such as desired heading and pitch angles and desired airspeed. These parameters are mostly controlled by traditional PID (Proportional–Integral–Derivative) control loops with a two-level structure (Kownacki and Ambroziak, 2017; Kownacki and Ambroziak, 2019). Unfortunately, reaching the desired values of heading and pitch angles and airspeed by a UAV does not guarantee that flight will be controlled stably in the steady state. In windy environments, where there is a constant wind treated as the flow of air mass, the flight guidance of nonholonomic UAVs can be disturbed, especially if it is a crosswind. What results is that the ground speed of fixed-wing UAVs is the sum of True Air Speed (TAS) and wind speed, and in aviation, this is called the wind drift effect. The problem of wind drift is presented in Fig. 1a, where the asymmetrical artificial potential field (AAPF) approach is applied to track a moving point associated with the origin of a local coordinate system  $Ox_{Pi}y_{Pi}z_{Pi}$ . Arrows labelled with symbols  $V_T$ ,  $V_W$ ,  $V_G$ , and  $V_{UAV}$  represent, respectively, the velocity vector of the frame  $Ox_{Pi}y_{Pi}z_{Pi}$  (the velocity of the tracked point), the velocity vector of wind, the airspeed vector of the UAV obtained from the AAPF and the ground speed vector, which is the sum of the last two. Thus, the final flight path will be determined by the velocity vector  $V_{UAV}$ , not by the velocity vector field  $V_G$ .



**Fig. 1.** A flight scenario when wind drift disturbs flight guidance based on the artificial asymmetrical potential field: (a) control of position tracking based on AAPF in the case of constant wind presence. There is an angle between the reference velocity vector  $V_G$  given by AAPF and the ground speed vector  $V_{UAV}$ , which is called the drift angle. (b) the UAV is unable to reach a tracked position due to its resultant ground speed vector  $V_{UAV}$  being parallel to the velocity vector of the tracked position  $V_T$ . AAPF - asymmetrical artificial potential field, UAV - unmanned aerial vehicle

In Fig. 1b, there is a case where the UAV is unable to reach its desired position due to the fact that ground speed vector  $V_{UAV}$  is parallel to the velocity vector of the tracked position  $V_T$ . Therefore, the relative positions, i.e. the position tracking error, will be

constant in the steady-state. For this and similar cases, constant wind can be considered as a homogenous VVF that modifies the tracking guidance, accordingly to the superposition of both fields of the velocity vector (Fig. 2). The superposition of these two fields makes it impossible for a fixed-wing UAV to achieve precise position tracking. Therefore, the VVF constructed on AAPF should not be constant over time, but should change automatically in a way that minimises any position error in the steady-state caused by

wind drift. The most convenient and simplest way to minimise errors in the steady state is to include integrals of these errors in the definitions of the VVF. The novel definition of the VVF based on the AAPF approach for fixed-wing UAVs is given in the next section. The method, which utilises this novel definition, is called the self-adaptive AAPF approach, and it is addressed to the problem of wind drift for nonholonomic UAVs.

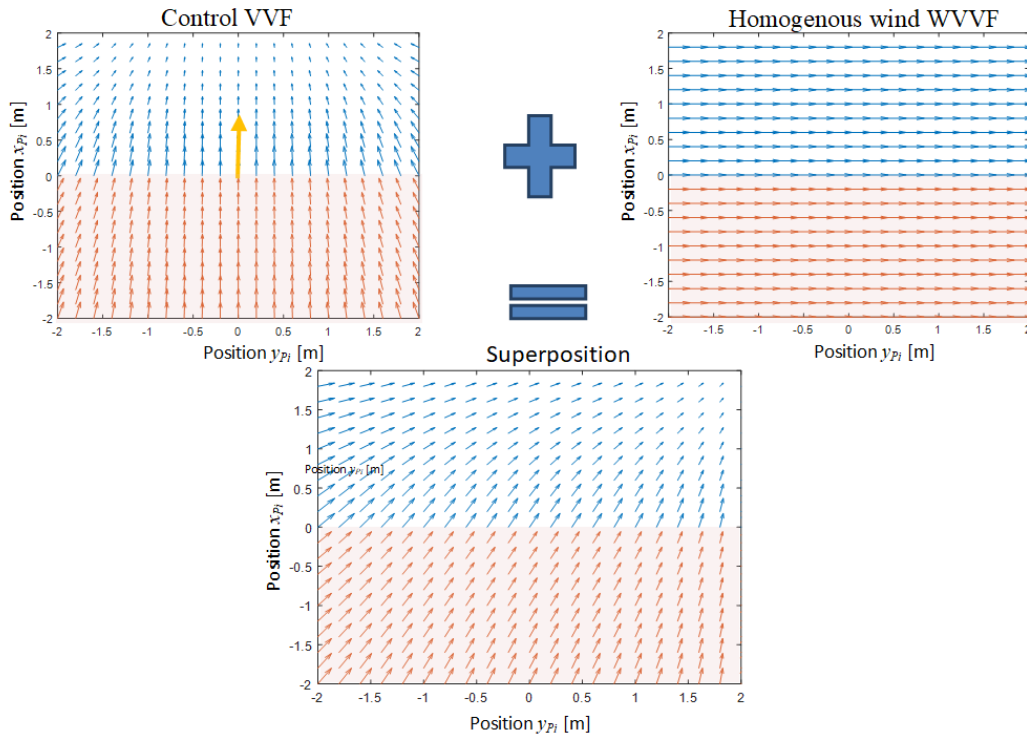


Fig. 2. A superposition of the VVF given by AAPF and the WVVF, modifying guidance and disabling the possibility of precise position tracking. AAPF - asymmetrical artificial potential field; VVF - velocity vector field; WVVF - wind velocity vector field.

### 3. SELF-ADAPTIVE ASYMMETRICAL POTENTIAL FIELD

The AAPF ensures stable position tracking in the case of nonholonomic UAVs, which is proven in Kownacki and Ambroziak (2017). In turn, the rotation mechanism described in Kownacki and Ambroziak (2019) minimises tracking error during manoeuvres when nonholonomic UAVs fly in a rigid formation. The novel approach proposed in this work is also dedicated to nonholonomic vehicles; hence, the definition of AAPF from Kownacki and Ambroziak (2017) and Kownacki and Ambroziak (2019) will be the

starting point. Let us consider a scenario where a UAV tracks a virtual point which is simultaneously the origin of a local coordinate system  $Ox_{Pi}y_{Pi}z_{Pi}$ . Spatial orientations of axes  $x_{Pi}$ ,  $y_{Pi}$  and  $z_{Pi}$  are determined by vertical and horizontal movements of that point in the global coordinate system  $Ox_{GyG}z_{G}$ . UAV coordinates given in the frame  $Ox_{Pi}y_{Pi}z_{Pi}$  are values of tracking errors. The proposed novel approach aims to minimise values of those coordinates when a fixed-wing UAV flies under windy conditions.

The definition of AAPF  $U_i^S$  will be the same as in Kownacki and Ambroziak (2017) and Kownacki and Ambroziak (2019):

$$U_i^S(x_{Pi}, y_{Pi}, z_{Pi}) = \begin{cases} V_L \cdot \arctan(\alpha \cdot x_{Pi}) + \frac{1}{3} \cdot \gamma \cdot |y_{Pi}|^3 + \frac{1}{3} \cdot \gamma \cdot |z_{Pi}|^3, & x_{Pi} \geq 0 \\ V_L \cdot |\alpha \cdot x_{Pi}| + \frac{1}{3} \cdot \beta \cdot |x_{Pi}|^3 + \frac{1}{3} \cdot \gamma \cdot |y_{Pi}|^3 + \frac{1}{3} \cdot \gamma \cdot |z_{Pi}|^3, & x_{Pi} < 0 \end{cases} \quad (1)$$

where  $V_L$  – is the airspeed of the tracked virtual point,  $\alpha$ ,  $\beta$ ,  $\gamma$  – coefficients regulating the slope of the potential function, i.e. in the forward longitudinal direction; ( $x_{Pi} > 0$ ) – rate of deceleration, in backward direction; ( $x_{Pi} < 0$ ) – rate of acceleration, and in both

perpendicular directions, lateral and vertical; ( $y_{Pi}$  and  $z_{Pi}$ ) – respectively, rate of heading and pitch.

According to Kownacki and Ambroziak (2017) and Kownacki and Ambroziak (2019), the gradient of the potential function  $U_i^S$  is as follows:

$$\nabla U_i^S(x_{Pi}, y_{Pi}, z_{Pi}) = \begin{cases} \left[ \frac{\alpha \cdot V_L}{1 + (\alpha \cdot x_{Pi})^2}, \gamma \cdot \text{sgn}(y_{Pi}) \cdot y_{Pi}^2, \gamma \cdot \text{sgn}(z_{Pi}) \cdot z_{Pi}^2 \right], & x_{Pi} \geq 0 \\ \left[ \text{sgn}(x_{Pi}) \cdot (\alpha \cdot V_L + \beta \cdot x_{Pi}^2), \gamma \cdot \text{sgn}(y_{Pi}) \cdot y_{Pi}^2, \gamma \cdot \text{sgn}(z_{Pi}) \cdot z_{Pi}^2 \right], & x_{Pi} < 0 \end{cases} \quad (2)$$



The gradient  $\nabla U_i^S$  is only a function of the relative position given in the local frame  $Ox_{Pi}y_{Pi}z_{Pi}$ . As shown in Fig. 1b, it can be insensitive to position tracking error at the steady state as a result of wind drift. Therefore, gradient definition (2) must be modified in a way that relates gradient components to cumulative tracking error expressed by its integral. According to Kownacki and Ambroziak (2017) and Kownacki and Ambroziak (2019), gradient  $\nabla U_i^S$  is the basis for creating the VVF that is used to calculate the desired heading, pitch and airspeed. Therefore, if the integral of tracking error modifies elements of gradient  $\nabla U_i^S$ , it will affect UAV guidance.

Modifications of gradient definition (2) on the longitudinal axis  $x_{Pi}$  will first be discussed. To minimise the steady-state tracking error on axis  $x_{Pi}$ , the length of gradient  $\nabla U_i^S$  and the length of the related velocity vector  $V_i^S$  on this axis should be changed according to the increasing integral of tracking error. For  $x_{Pi} \geq 0$ , the lengths should be decreased, and for  $x_{Pi} < 0$ , increased.

$$\nabla U_i^{AD}(x_{Pi}, y_{Pi}, z_{Pi}) = \begin{cases} \left[ \frac{\alpha \cdot V_L}{1 + (\alpha + \delta_{x1} \cdot |I_X|)^2 \cdot x_{Pi}^2}, \gamma \cdot \text{sgn}(y_{Pi}) \cdot y_{Pi}^2, \gamma \cdot \text{sgn}(z_{Pi}) \cdot z_{Pi}^2 \right], & x_{Pi} \geq 0 \\ [\text{sgn}(x_{Pi}) \cdot (\alpha \cdot V_L + (\beta + \delta_{x2} \cdot |I_X|) \cdot x_{Pi}^2), \gamma \cdot \text{sgn}(y_{Pi}) \cdot y_{Pi}^2, \gamma \cdot \text{sgn}(z_{Pi}) \cdot z_{Pi}^2], & x_{Pi} < 0 \end{cases} \quad (3)$$

where  $I_X$  – is the value of the integral (Eq. 3) on axis  $x_{Pi}$ ,  $\delta_{x1}$ ,  $\delta_{x2}$  – gains of  $I_X$ .

$$I_X = \begin{cases} \int_0^t x_{Pi} d\tau, & (x_{Pi} \geq 0 \cap \int_0^t x_{Pi} d\tau \geq 0) \cup (x_{Pi} < 0 \cap \int_0^t x_{Pi} d\tau \leq 0) \\ 0 & \end{cases} \quad (4)$$

$$V_i^S(x_{Pi}, y_{Pi}, z_{Pi}) = \begin{bmatrix} \nabla U_i^S(x_{Pi}) \\ -\nabla U_i^S(y_{Pi}) \\ -\nabla U_i^S(z_{Pi}) \end{bmatrix} \cdot D(\psi_L) \quad (5)$$

These integrals have the same role as integral  $I_X$  in Eq. (3), but they are used to compensate wind drift on axes  $y_{Pi}$  and  $z_{Pi}$  by changing the direction of flight defined by heading and pitch angles. The value of integral  $I_X$  has an impact on the  $x_{Pi}$ -axis component of gradient  $\nabla U_i^{AD}$  only when the sign of integral  $\int_0^t x_{Pi} d\tau$  is the same as the sign of  $x_{Pi}$ . Otherwise, the value of  $I_X$  equals zero, and the definition of the gradient  $\nabla U_i^{AD}$  is identical to that of  $\nabla U_i^S$ . This rule is necessary, because integral  $I_X$  should compensate for wind drift as follows: its negative value should only accel-

Therefore, the definition of the potential function gradient (2) must be modified by inserting coefficients dependent on the current value of the integral  $I_X$ . It adapts the gradient length on axis  $x_{Pi}$  with a strength depending on the values of gains  $\delta_{x1}$ ,  $\delta_{x2}$ . The modified gradient  $\nabla U_i^{AD}$  is defined by Eq. (3), and differences between definitions (2) and (3) are highlighted by bold font. In Eq. (2), coefficients on  $x_{Pi}$ , i.e.  $\alpha$  and  $\beta$ , are constant over time. In Eq. (3), these coefficients are, respectively, the sum of  $\alpha$  and  $\delta_{x1} \cdot |I_X|$  and the sum of  $\beta$  and  $\delta_{x2} \cdot |I_X|$ ; therefore, they are time-variant and depend on the constant tracking error caused by wind drift.

To formulate a new definition of velocity vector field  $V_i^S$ , gradient  $\nabla U_i^S$  must be replaced with  $\nabla U_i^{AD}$ . However, for the  $y_{Pi}$  and  $z_{Pi}$  axes, both definitions (2) and (3) are identical. To change values of desired heading and pitch angles, it is necessary to introduce compensation vector  $I$ , which is a function of integrals  $I_Y$  and  $I_Z$ .

erate the UAV when  $x_{Pi} < 0$  and its positive value should decelerate the UAV only when  $x_{Pi} \geq 0$  (Fig. 3). For other cases, gradient  $\nabla U_i^{AD}$  must be the same as gradient  $\nabla U_i^S$  to prevent oscillations. Therefore, the sign of integral  $I_X$  must be correlated with the sign of  $x_{Pi}$ , and its change switches guidance rules on axis  $x_{Pi}$  between  $\nabla U_i^{AD}$  and  $\nabla U_i^S$  (Fig. 3). This happens when the UAV crosses the  $y$ - $z$  plane.

The next modifications related to the novelty of the self-adaptive asymmetrical potential function are addressed directly to velocity vector field  $V_i^S$  from Kownacki and Ambroziak (2019). Velocity vector field  $V_i^S$  based on gradient  $\nabla U_i^S$  is given by Eq. (5) (Kownacki and Ambroziak, 2019).

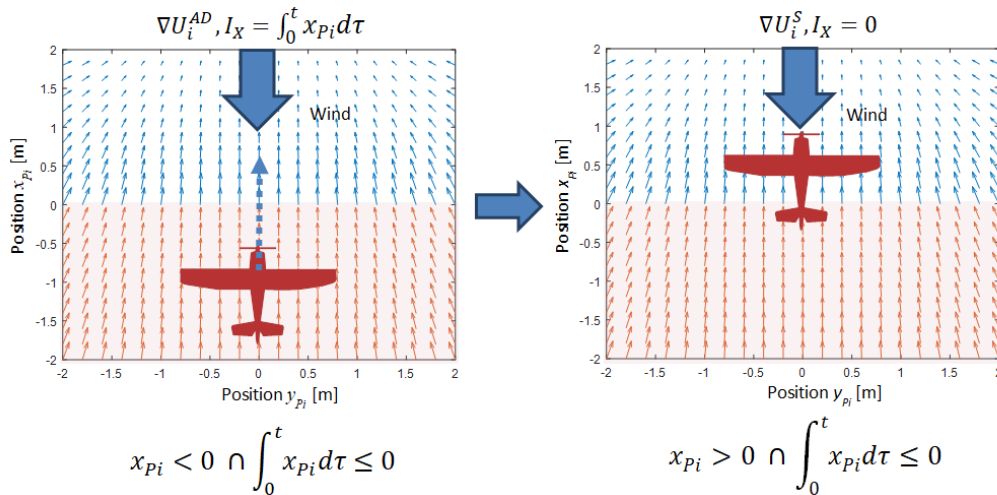


Fig. 3. Switching between gradient  $\nabla U_i^{AD}$  and  $\nabla U_i^S$  when the UAV flies behind the tracked position and then crosses the  $y$ - $z$  plane. UAV, unmanned aerial vehicles

The definition of velocity vector field  $V_i^{AD}$  applied in the self-adaptive approach is as follows:

$$V_i^{AD}(x_{Pi}, y_{Pi}, z_{Pi}) = \left[ \begin{array}{c} \nabla U_i^{AD}(x_{Pi}) \\ -\nabla U_i^{AD}(y_{Pi}) \\ -\nabla U_i^{AD}(z_{Pi}) \end{array} \right] + I \cdot D(\Psi_L) =$$

$$\left( \left[ \begin{array}{c} |\nabla U_i^{AD}(x_{Pi})| \\ -\nabla U_i^{AD}(y_{Pi}) \\ -\nabla U_i^{AD}(z_{Pi}) \end{array} \right] - \left[ \begin{array}{c} 0 \\ \delta_y \cdot |I_y| \cdot \text{sgn}(y_{Pi}) \cdot y_{Pi}^2 \\ \delta_z \cdot |I_z| \cdot \text{sgn}(z_{Pi}) \cdot z_{Pi}^2 \end{array} \right] \right) \cdot \left[ \begin{array}{ccc} \cos(\varepsilon \cdot \Psi_L) & \sin(\varepsilon \cdot \Psi_L) & 0 \\ -\sin(\varepsilon \cdot \Psi_L) & \cos(\varepsilon \cdot \Psi_L) & 0 \\ 0 & 0 & 1 \end{array} \right] \quad (6)$$

where  $\Psi_L$  – is the rate of heading angle of the tracked virtual point;  $\varepsilon$  – gain coefficient having the meaning of the time constant related to inertia of response to tracked point turns;  $I$  – compensation vector dependent on integrals of tracking errors on the  $y$ -axis

( $I_y$ ) and  $z$ -axis ( $I_z$ ); and  $\delta_y, \delta_z$  – gains of integrals  $I_y$  and  $I_z$ , respectively.

Definitions of the integral values  $I_y$  and  $I_z$  are given below:

$$I_y = \begin{cases} \int_0^t y_{Pi} d\tau, & (y_{Pi} \geq 0 \cap \int_0^t y_{Pi} d\tau \geq 0) \cup (y_{Pi} < 0 \cap \int_0^t y_{Pi} d\tau \leq 0) \\ 0 & \end{cases} \quad (7)$$

$$I_z = \begin{cases} \int_0^t z_{Pi} d\tau, & (z_{Pi} \geq 0 \cap \int_0^t z_{Pi} d\tau \geq 0) \cup (z_{Pi} < 0 \cap \int_0^t z_{Pi} d\tau \leq 0) \\ 0 & \end{cases} \quad (8)$$

where  $z_{Pi}, y_{Pi}$  – are UAV coordinates (tracking errors) on axes  $z_{Pi}$  and  $y_{Pi}$  of frame  $Ox_{Pi}y_{Pi}z_{Pi}$ .

Integrals  $I_y$  and  $I_z$  modify lengths of velocity vectors  $V_i^{AD}$  on the  $z_{Pi}$  and  $y_{Pi}$  axes, which changes both lengths and spatial orientations of velocity vectors. Also, in this case, the signs of integrals  $I_y$  and  $I_z$  must be the same as the signs of tracking errors on the  $y_{Pi}$  and  $z_{Pi}$  axes. Otherwise, values of these integrals should equal zero, and Eq. (6) becomes the same as Eq. (5), or almost the same when  $\nabla U_i^{AD}$  is identical to  $\nabla U_i^S$  for  $I_x$  different from zero. This switching prevents situations when the UAV crosses planes defined by axes  $x_{Pi}-z_{Pi}$  or  $x_{Pi}-y_{Pi}$ , and the sign of the corresponding tracking error on the  $y_{Pi}$  or  $z_{Pi}$  axis is reversed. If the integrals  $I_y$  or

$I_z$  are non-zero values with signs opposite to tracking errors, velocity vector field  $V_i^{AD}$  will guide the UAV in the same direction as the wind, and the wind drift effect will be amplified. This could cause position oscillations on the  $y_{Pi}$  or  $z_{Pi}$  axis. Therefore, the compensation should work only in the direction opposite to the wind (Fig. 4).

In the next section, results of numerical simulations prove that the novel self-adaptive potential field approach, which uses integrals  $I_x, I_y$  and  $I_z$  to modify gradient  $\nabla U_i^{AD}$  and velocity vector field  $V_i^{AD}$ , effectively minimises the steady-state tracking error caused by the wind.

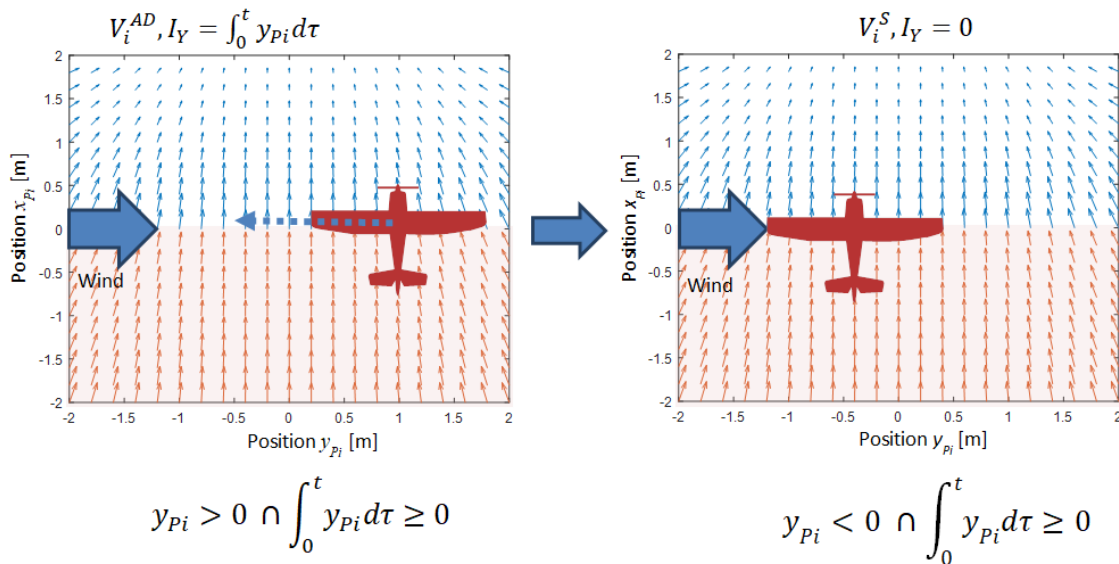


Fig. 4. Switching between  $V_i^{AD}$  and  $V_i^S$  when the UAV flies to the left of the tracked position and then crosses the  $x$ - $z$  plane.  
UAV - unmanned aerial vehicles

#### 4. NUMERICAL SIMULATIONS

In numerical simulations, the same dynamical model of a fixed-wing UAV was utilised as in works of Kownacki and Ambroziak (2017) and Kownacki and Ambroziak (2019). The UAV's dynamics are defined by a set of six differential equations, namely

Eqs (9) and (10):

$$\begin{bmatrix} \dot{u} \\ \dot{v} \\ \dot{w} \end{bmatrix} = \begin{bmatrix} r \cdot v - q \cdot w \\ p \cdot w - r \cdot u \\ q \cdot u - p \cdot v \end{bmatrix} + \frac{1}{m} \cdot \begin{bmatrix} F_x \\ F_y \\ F_z \end{bmatrix} \quad (9)$$

$$\begin{bmatrix} \ddot{p} \\ \ddot{q} \\ \ddot{r} \end{bmatrix} = \begin{bmatrix} \frac{I_{xz}(I_x - I_y + I_z)}{I_x \cdot I_z - I_{xz}^2} \cdot p \cdot q - \frac{I_z(I_z - I_y) + I_{xz}^2}{I_x \cdot I_z - I_{xz}^2} \cdot q \cdot r + \frac{I_z}{I_x \cdot I_z - I_{xz}^2} \cdot L + \frac{I_{xy}}{I_x \cdot I_z - I_{xz}^2} \cdot N \\ \frac{I_z - I_x}{I_y} \cdot p \cdot r - \frac{I_{xz}}{I_y} (p^2 - r^2) + \frac{1}{I_y} \cdot M \\ \frac{I_{xz}(I_x - I_y) + I_{xz}^2}{I_x \cdot I_z - I_{xz}^2} \cdot p \cdot q - \frac{I_{xz}(I_z - I_y + I_z)}{I_x \cdot I_z - I_{xz}^2} \cdot q \cdot r + \frac{I_{xz}}{I_x \cdot I_z - I_{xz}^2} \cdot L + \frac{I_x}{I_x \cdot I_z - I_{xz}^2} \cdot N \end{bmatrix} \quad (10)$$

where  $F_x, F_y, F_z$  – are components of the total force vector applied to the UAV i.e. the sum of aerodynamic forces, force of gravity, and the force of the propulsion system;  $L, M, N$  – moments on the  $x, y$  and  $z$  axis, respectively;  $I_x, I_y, I_z$  – mass moments of inertia around the  $x, y, z$  axes, respectively, of the UAV body frame;  $I_{xz}$  – product of inertia for the  $x - z$  symmetry plane;  $p, q, r$  – angular

velocities of banking, tilt, deflection;  $u, v, w$  – linear velocities; and  $m$  – mass of the vehicle.

Equations of the related kinematic model describing both position and orientation in the global frame  $G$  are given by Ambroziak and Gosiewski (2015) and Kownacki and Ambroziak (2017):

$$\begin{bmatrix} \dot{x}_G \\ \dot{y}_G \\ \dot{z}_G \end{bmatrix} = \begin{bmatrix} \cos(\Theta) \cdot \cos(\Psi) & \sin(\phi) \cdot \sin(\Theta) \cdot \cos(\Psi) & \cos(\phi) \cdot \sin(\Theta) \cdot \cos(\Psi) \\ & -\cos(\phi) \cdot \sin(\Psi) & +\sin(\phi) \cdot \sin(\Psi) \\ \cos(\Theta) \cdot \sin(\Psi) & \sin(\phi) \cdot \sin(\Theta) \cdot \sin(\Psi) & \cos(\phi) \cdot \sin(\Theta) \cdot \sin(\Psi) \\ & +\cos(\phi) \cdot \cos(\Psi) & -\sin(\phi) \cdot \sin(\Psi) \\ -\sin(\Theta) & \sin(\phi) \cdot \cos(\Theta) & \cos(\phi) \cdot \cos(\Theta) \end{bmatrix} \cdot \begin{bmatrix} u \\ v \\ w \end{bmatrix} \quad (11)$$

$$\begin{bmatrix} \dot{\phi} \\ \dot{\Theta} \\ \dot{\Psi} \end{bmatrix} = \begin{bmatrix} 1 & \sin(\phi) \cdot \tan(\Theta) & \cos(\phi) \cdot \tan(\Theta) \\ 0 & \cos(\phi) & -\sin(\phi) \\ 0 & \frac{\sin(\phi)}{\cos(\Theta)} & \frac{\cos(\phi)}{\cos(\Theta)} \end{bmatrix} \cdot \begin{bmatrix} p \\ q \\ r \end{bmatrix} \quad (12)$$

where  $\phi, \Theta, \Psi$  – are the orientation angles of roll, pitch and heading angle, respectively;  $p, q, r$  – angular velocities of banking, tilt, deflection;  $u, v, w$  – linear velocities; and  $x_G, y_G, z_G$  – coordinates in the  $G$  frame.

The sum of forces applied to the body frame of a fixed-wing UAV is as follows (Ambroziak and Gosiewski, 2015; Kownacki and Ambroziak, 2017):

$$F = \begin{bmatrix} F_x \\ F_y \\ F_z \end{bmatrix} = \begin{bmatrix} -mg \cdot \sin(\Theta) \\ mg \cdot \cos(\Theta) \cdot \sin(\phi) \\ mg \cdot \cos(\Theta) \cdot \cos(\phi) \end{bmatrix} + \begin{bmatrix} F_p \\ 0 \\ 0 \end{bmatrix} + \begin{bmatrix} F_x^a \\ F_y^a \\ F_z^a \end{bmatrix} \quad (13)$$

where:  $mg$  – force of gravity,  $F_p$  – propulsion force (Eq. 12),  $F_z^a$  – lifting force,  $F_x^a$  – drag force,  $F_y^a$  – lateral force.

The force  $F_p$  generated by the propulsion system, i.e. propeller and electrical engine, is modelled by the equation (Ambroziak and Gosiewski, 2015; Kownacki and Ambroziak, 2017):

$$F_p = \frac{A \cdot \rho \cdot [(k_m \cdot \delta_t)^2 - V_A^2]}{2} \quad (14)$$

where  $V_A$  – is airspeed of UAV;  $\rho$  – air density;  $k_m$  – the relation between throttle control signal,  $\delta$  and engine revolutions; and  $A$  – the area swept out by the propeller blade.

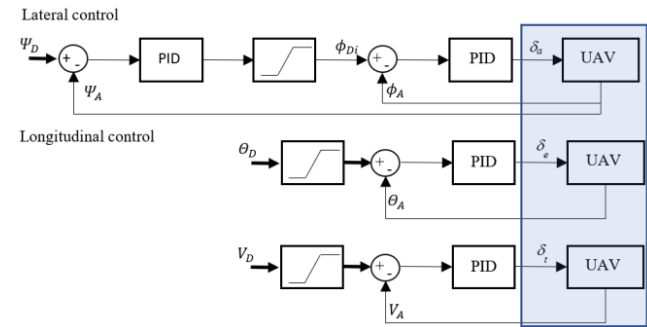
The sum of aerodynamic moments and the moment generated by the propulsion system are given as follows (Ambroziak and Gosiewski, 2015; Kownacki and Ambroziak, 2017):

$$\begin{bmatrix} L \\ M \\ N \end{bmatrix} = \begin{bmatrix} 0 \\ M_p \\ 0 \end{bmatrix} + \begin{bmatrix} L_a \\ M_a \\ N_a \end{bmatrix} = \begin{bmatrix} 0 \\ -k_t \cdot (k_m \cdot \delta_t)^2 \\ 0 \end{bmatrix} + \begin{bmatrix} L_a \\ M_a \\ N_a \end{bmatrix} \quad (15)$$

where  $M_p$  – is the moment generated by the propulsion system if the axis of propeller rotation coincides with the  $x$ -axis of the UAV's body;  $L_a$  – rolling moment;  $M_a$  – pitching moment;  $N_a$  – yawing moment;  $k_m$  – relation between throttle control signal,  $\delta$  and engine revolutions; and  $k_t$  – coefficient of propeller torque.

Aerodynamic moments  $L_a, M_a, N_a$  are functions of control sur-

face deflections, respectively:  $\delta_a$  – ailerons (roll angle),  $\delta_e$  – elevator (pitch angle) and  $\delta_r$  – rudder (yaw angle). In turn, the propulsion force  $F_p$  is a function of throttle  $\delta_t$ . Deflections  $\delta_a, \delta_e$  and throttle  $\delta_t$  are outputs of lateral and longitudinal controls of the UAV, which are based on PID loops as shown in Fig. 5.



**Fig. 5.** Lateral and longitudinal control of the  $i$ -th UAV based on PID loops.  $\Psi_{Di}$  and  $\Psi_{Ai}$  – respectively, desired and actual heading;  $\phi_{Di}$  and  $\phi_{Ai}$  – respectively, desired and actual roll angle;  $\Theta_{Di}$  and  $\Theta_{Ai}$  – respectively, desired and actual pitch angle;  $V_{Di}$  and  $V_{Ai}$  – respectively, desired and actual airspeed (Kownacki and Ambroziak, 2017). UAV – unmanned aerial vehicle

Desired values of heading angle  $\Psi_{Di}$ , pitch angle  $\Theta_{Di}$  and airspeed  $V_{Di}$  can be simply obtained from velocity vector field  $V_i^{AD}$  as given by equations (Kownacki C. and Ambroziak L., 2019; Kownacki C. and Ambroziak L., 2019):

$$\Psi_{Di} = \text{atan2} \left( V_i^{AD}(y_{Pi}), V_i^{AD}(x_{Pi}) \right) \quad (16)$$

$$\Theta_{Di} = \text{atan2} \left( V_i^{AD}(z_{Pi}), \sqrt{V_i^{AD}(x_{Pi})^2 + V_i^{SD}(y_{Pi})^2} \right) \quad (17)$$

$$V_{Di} = \sqrt{V_i^{AD}(x_{Pi})^2 + V_i^{AD}(y_{Pi})^2 + V_i^{AD}(z_{Pi})^2} \quad (18)$$

To verify the effectiveness of the proposed changes in the novel definitions of gradient  $V_i^{AD}$  and related velocity vector field  $V_i^{AD}$ , numerical simulations considering two scenarios were prepared. In each of them, the fixed-wing UAV follows a virtual point which is its desired position. Therefore, if the position tracking

algorithm is effective in minimising tracking errors, both flight paths, i.e. the flight path of the UAV and the reference trajectory of the virtual point, should overlap. During simulated flights, a step change of wind velocity is generated to observe the response of lateral and longitudinal controls based on the proposed self-

adaptive approach. In each scenario, the direction of the wind is different, which makes separate verification of lateral and longitudinal guidance possible (Fig. 6). In the next section, flight paths and time plots of tracking errors present the results achieved.

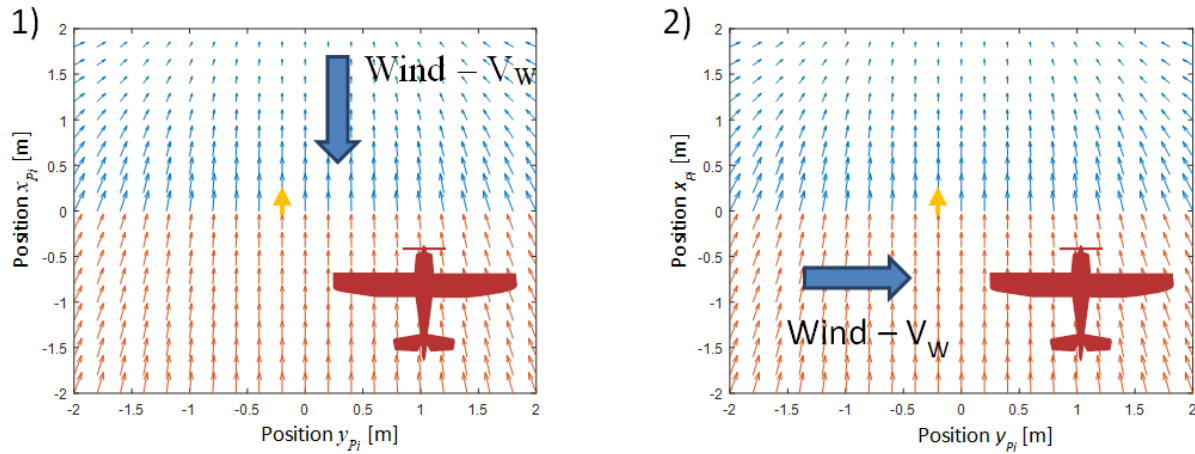


Fig. 6. Simulated scenarios of a step change of wind velocity to verify lateral and longitudinal controls of UAV. UAV - unmanned aerial vehicle

## 5. RESULTS

In each simulation, positions of the virtual tracked point and the starting point of the UAV overlap, and paths of the virtual point are designed as straight lines. Since the UAV tracks the virtual point and the initial airspeeds of both are zero, there should be inertia between the movements of the UAV and the tracked virtual point. In the first considered case, the direction of the simulated step change of wind velocity is exactly opposite to the direction of the virtual point's movement. Therefore, it should increase tracking error on the  $x_{Pi}$  axis as steady-state tracking error, i.e. wind

drift. In the second case, the direction of the wind is perpendicular to the line of the virtual point's path. Thus, the tracking error should increase on the  $y_{Pi}$  axis.

Firstly, it should be examined how the previous approach of AAPF is able to decrease tracking error in the steady state. To verify this, numerical simulations were prepared according to the second scenario for different values of coefficients  $\alpha$  (0.1, 0.9),  $\beta$  (0.1, 0.9) and  $\gamma$  (0.1, 0.9) (Eq. 3), and  $\delta_{x1}$ ,  $\delta_{x2}$ ,  $\delta_y$  and  $\delta_z$  equal zero. Time plots of tracking errors on each axis are presented in Fig. 7. The amplitude of the step change of wind velocity at  $t = 100$  s is 1 m/s.

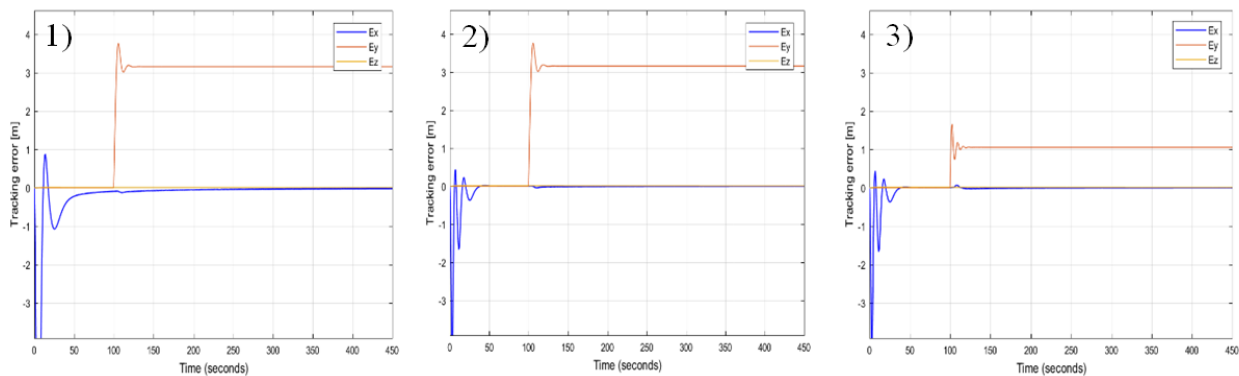


Fig. 7. Time plots of tracking errors on axes  $x_{Pi}$ ,  $y_{Pi}$  and  $z_{Pi}$  for the following values of coefficients  $\alpha$ ,  $\beta$  and  $\gamma$ : (1)  $\alpha = 0.1$ ,  $\beta = 0.1$  and  $\gamma = 0.1$ , (2)  $\alpha = 0.9$ ,  $\beta = 0.9$  and  $\gamma = 0.1$ , (3)  $\alpha = 0.9$ ,  $\beta = 0.9$  and  $\gamma = 0.9$

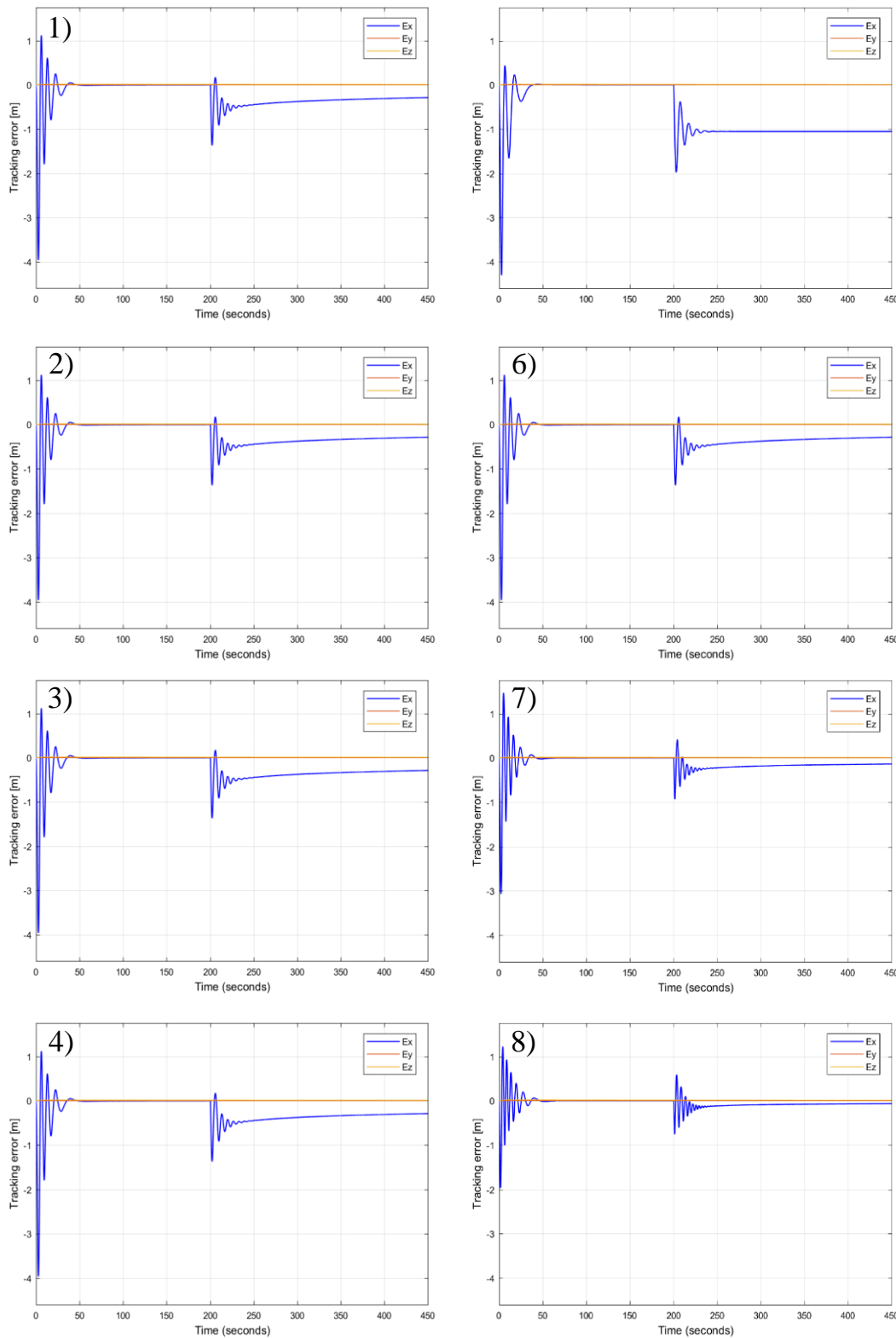
According to the first scenario (Fig. 6), different values of  $\delta_{x1}$ ,  $\delta_{x2}$  were used to observe minimisation of the tracking error on the  $x_{Pi}$  axis as the result of a step change of wind velocity at  $t = 200$  s. on this axis with an amplitude equal to 1 m/s. Simulation results are given in Fig. 8.

In Fig. 6, it can be seen that time plots of  $E_x$  are independent from the values of  $\delta_{x1}$  (Fig. 8.1–8.4). This is because this coefficient regulates the gain of integral  $I_x$  for  $x_{Pi} > 0$ , when the UAV is flying behind the virtual point, and thus  $x_{Pi} < 0$  and  $I_x < 0$ . This is

in accordance with the assumptions of guidance rules defined by Eqs (3), (4), (6), (7) and (8). On the other hand, in Figs. 8.5–8.8, a decrement of tracking error  $E_x$  can be observed for higher values of  $\delta_{x2}$ . A side effect of the action of integral  $I_x$  is transient and quickly fading oscillations whose frequency grows with the value of  $\delta_{x2}$ . Amplitudes of these oscillations are less than 1 m, and their durations are less than 25 s. Therefore, they should not have a significant impact on the effectiveness of flight guidance based on the proposed approach.

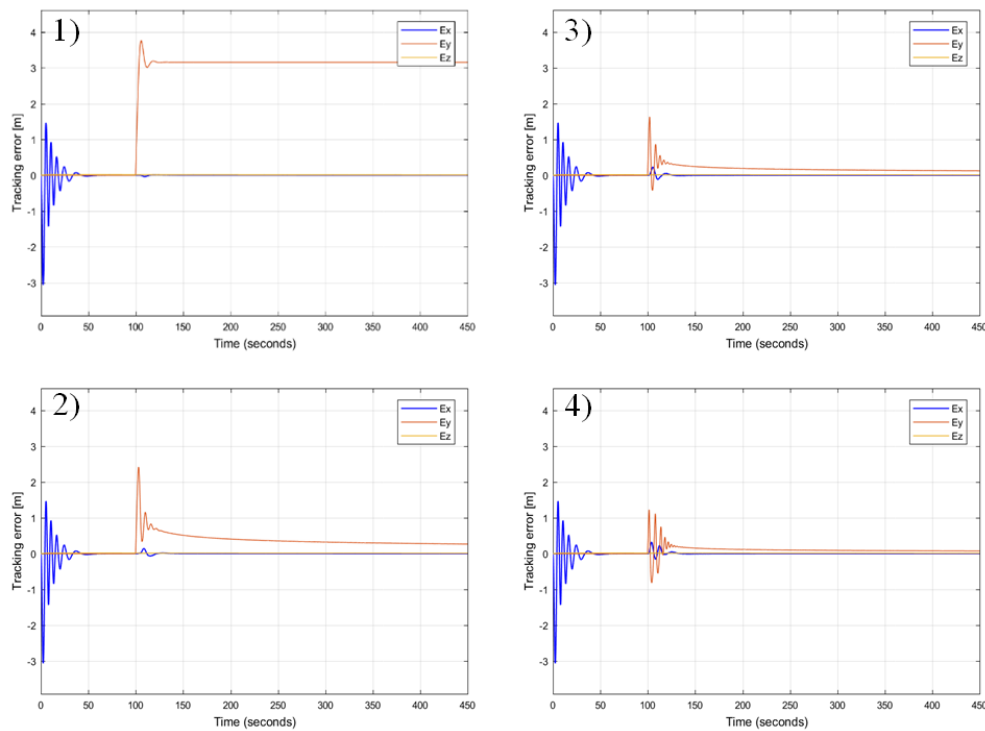
In the second scenario, where the wind direction is perpendicular to the simulated flight path of the virtual point, only coefficient  $\delta_y$  matters, because it is related to integral  $I_y$ . The rest of the parameters are as follows:  $\alpha$ ,  $\beta$  and  $\gamma$  remain the same,  $\delta_{x1} = 1$

and  $\delta_{x2} = 1$ . In Figs. 9.1–9.4, time plots of tracking errors are presented for a value of  $\delta_y$  equal to, respectively, 0, 0.1, 1 and 5.



**Fig. 8.** Time plots of tracking errors on axes  $x_{Pi}$ ,  $y_{Pi}$  and  $z_{Pi}$  for the following values of coefficients  $\delta_{x1}$ ,  $\delta_{x2}$ ,  $\delta_y$  and  $\delta_z$ : (1)  $\delta_{x1} = 0$ ,  $\delta_{x2} = 0.1$ ,  $\delta_y = 0$  and  $\delta_z = 0$ , (2)  $\delta_{x1} = 0.5$ ,  $\delta_{x2} = 0.1$ ,  $\delta_y = 0$  and  $\delta_z = 0$ , (3)  $\delta_{x1} = 1$ ,  $\delta_{x2} = 0.1$ ,  $\delta_y = 0$  and  $\delta_z = 0$ , (4)  $\delta_{x1} = 1.5$ ,  $\delta_{x2} = 0.1$ ,  $\delta_y = 0$  and  $\delta_z = 0$ , (5)  $\delta_{x1} = 1$ ,  $\delta_{x2} = 0$ ,  $\delta_y = 0$  and  $\delta_z = 0$ , (6)  $\delta_{x1} = 1$ ,  $\delta_{x2} = 0.1$ ,  $\delta_y = 0$  and  $\delta_z = 0$ , (7)  $\delta_{x1} = 1$ ,  $\delta_{x2} = 1$ ,  $\delta_y = 0$  and  $\delta_z = 0$ , (8)  $\delta_{x1} = 1$ ,  $\delta_{x2} = 10$ ,  $\delta_y = 0$  and  $\delta_z = 0$





**Fig. 9.** Time plots of tracking errors on axes  $x_{Pi}$ ,  $y_{Pi}$  and  $z_{Pi}$  for the following values of coefficients  $\delta_{x1}$ ,  $\delta_{x2}$ ,  $\delta_y$  and  $\delta_z$ :  $\delta_{x1} = 1$ ,  $\delta_{x2} = 1$ , (1)  $\delta_y = 0$ , (2)  $\delta_y = 0.1$ , (3)  $\delta_y = 1$ , (4)  $\delta_y = 5$

Based on Fig. 7, it is possible to conclude that  $\alpha$  and  $\beta$  improve guidance dynamics on the  $x_{Pi}$  axis by increasing the slope of potential function  $U_i^S$  on both sides of the  $y_{Pi} - z_{Pi}$  plane. Oscillations of tracking error on axis  $x_{Pi}$  are caused by inertia in position tracking at instant  $t = 0$  and UAV guidance switching between acceleration and deceleration zones separated by the  $y_{Pi} - z_{Pi}$  plane. The frequency of this oscillation increases with the increment of the potential function's slope caused by higher values of  $\alpha$  and  $\beta$ . As would be expected, values of  $\alpha$  and  $\beta$  have no effect on tracking error  $E_y$  on the  $y_{Pi}$  axis. This tracking error can be decreased by increasing the value of  $\gamma$ , which can be observed by comparing Figs 7 (2 and 3). However,  $E_y$  still does not decrease over time; thus, it should be considered as steady-state tracking error caused by wind drift.

Next, non-zero values of  $\delta_{x1}$ ,  $\delta_{x2}$ ,  $\delta_y$ , and  $\delta_z$  are applied in the novel definitions of gradient  $\nabla U_i^{AD}$  and velocity vector field  $V_i^{AD}$  to include integrals  $I_x$ ,  $I_y$ , and  $I_z$ . Values of  $\alpha$ ,  $\beta$  and  $\gamma$  are constant and are, respectively, 0.9, 0.9 and 0.1.

Also, in this case, a value of  $\delta_y$  higher than 0 guarantees that tracking error  $E_y$  decreases over time. The magnitude of decrement increases with the value of  $\delta_y$ , but simultaneously, the amplitude and frequency of oscillations of tracking error  $E_y$  also grow. However, these oscillations are still transient and fast-fading, and they have no bearing on the effectiveness of the approach to minimisation of tracking error in the steady state.

## 6. CONCLUSION

Both methods based on AAPFs have significance to the problem of position tracking by nonholonomic vehicles such as fixed-wing UAVs. They improve the stability and the precision of position tracking during manoeuvres. However, they do not prevent against position tracking errors in the steady state, caused by

wind drift in windy environments. Therefore, definitions of the gradient of the asymmetrical potential function and the VVF should be dependent on integrals of tracking errors, as in the definition of a proportional-integral-derivative controller, where the integral is used to minimise steady-state errors. As presented, numerical simulation results confirm that such modification will allow for reduction of tracking errors asymptotically in the steady state. This is because of the fact that integrals of tracking errors are variable gain coefficients which modify the gradient according to the growth of the steady-state error, in a manner identical to the increment of the potential function's slope. This effect is presented in Figs 8 and 9, where time plots of tracking errors for different values of integrals' coefficients,  $\delta_{x1}$ ,  $\delta_{x2}$ , and  $\delta_y$ , compare the effectiveness of tracking error minimisation. Increasing values of these integrals' coefficients amplify the magnitude of decrement but simultaneously increase the frequency of oscillation. Fortunately, oscillations are quickly suppressed by inertia in the unmanned aerial vehicle's dynamics. Therefore, integrals' coefficients,  $\delta_{x1}$ ,  $\delta_{x2}$ ,  $\delta_y$ , and  $\delta_z$ , as well as coefficients of the potential function,  $\alpha$ ,  $\beta$  and  $\gamma$ , should be precisely adjusted to the dynamics specific to each considered fixed-wing UAVs' construction.

In summary, the novel self-adaptive approach to the asymmetrical potential function makes the position tracking problem more resistant to external disturbances in windy environments, which is crucial for fixed-wing UAVs. This is not possible through the usage of other methods of path planning, which are based on symmetrical APFs.

## REFERENCES

1. Ambroziak L., Gosiewski Z. (2015), Two Stage Switching Control for Autonomous Formation Flight of Unmanned Aerial Vehicles, *Aerospace Science and Technology*, Vol. 46, 2015, pp. 221-226,

2. Ambroziak L., Kondratiuk M., Ciekowski M., Kownacki C. (2018), Hardware in the Loop Tests of the Potential Field-Based Algorithm for Formation Flight Control of Unmanned Aerial Vehicles, *Mechatronic Systems and Materials 2018, Zakopane, AIP Conference Proceedings 2029*, 020002-1–020002-10.
3. Barnes L., Fields M. and Valavanis K. (2007), Unmanned Ground Vehicle Swarm Formation Control Using Potential Fields, in *Mediterranean Conference on Control and Automation*, Athens.
4. Bennet D. J., McInnes C. R. (2008) Space Craft Formation Flying Using Bifurcating Potential Fields, in *International Astronautical Congress*.
5. Bennet D. J., McInnes C. R. (2011), Autonomous Three-Dimensional Formation Flight for a Swarm of Unmanned Aerial Vehicles, *Journal of Guidance, Control, and Dynamics*, vol. 34, no. 6, pp. 1899-1908.
6. Budiayanto A., Cahyadi A., Adji T. B., Wahyunggoro O. (2015), UAV Obstacle Avoidance Using Potential Field Under Dynamic Environment, in *2015 International Conference on Control, Electronics, Renewable Energy and Communications*, Bandung.
7. Cetin O., Yilmaz G. (2016), Real-time Autonomous UAV Formation Flight with Collision and Obstacle Avoidance in Unknown Environment, *Journal of Intelligent & Robotic Systems*, vol. 84, no. 1, pp. 415-433.
8. Chen Y., Luo G., Mei Y., Yu J. and Su X. (2016), UAV Path Planning Using Artificial Potential Field Method Updated by Optimal Control Theory, *International Journal of System Science*, vol. 47, no. 6, pp. 1407-1420.
9. Chen Y., Yu J., Su X., Luo G. (2015), Path Planning for Multi-UAV Formation, *Journal of Intelligent & Robotic Systems*, vol. 77, no. 1, pp. 229-246.
10. Frew E. W., Lawrence D. A., Dixon C., Elston J., Pisano W. J. (2007), Lyapunov Guidance Vector Fields for Unmanned Aircraft Applications, in *IEEE American Control Conference*.
11. Gosiewski Z., Ambroziak L. (2012), Formation Flight Control Scheme for Unmanned Aerial Vehicles, *Lecture Notes in Control and Information Science*, vol. 422, pp. 331-340, 2012.
12. Hatton R.L., Choset H. (2011). Geometric Motion Planning: the Local Connection, Stokes' Theorem, and the Importance of Coordinate Choice. *The International Journal of Robotics Research*, 30(8), pp.988-1014,
13. Khuswendi T., Hindersah H., Adiprawita W. (2011), UAV Path Planning Using Potential Field and Modified Receding Horizon A\* 3D Algorithm, in *Proceedings of the 2011 International Conference on Electrical Engineering and Informatics*.
14. Kokume N., Uchiyama K. (2010), Guidance Law Based on Bifurcating Velocity Field for Formation Flight, in *AIAA Guidance, Navigation, and Control Conference*.
15. Kowalczyk W., Kozłowski K. (2004), Artificial Potential Based Control for a Large-Scale Formation of Mobile Robots., in *Proceedings of the Fourth International Workshop on Robot Motion and Control*.
16. Kownacki C. (2016), Multi-UAV Flight Using Virtual Structure Combined with Behavioral Approach, *Acta Mechanica et Automatica*, Vol. 10, No 2. 92-99.
17. Kownacki C., Ambroziak L. (2017), Local and Asymmetrical Potential Field Approach to Leader Tracking Problem in Rigid Formations of Fixed-Wing UAVs, *Aerospace Science and Technology*, Vol. 68, September 2017, pp. 465-474.
18. Kownacki C., Ambroziak L. (2019), Adaptation Mechanism of Asymmetrical Potential Field Improving Precision of Position Tracking in the Case of Non-Holonomic UAVs, *Robotica*, doi: <https://doi.org/10.1017/S0263574719000286>, published online: 10 April 2019, pp. 1-12,
19. Kownacki C., Oldziej O. (2016), Fixed-wing UAVs Flock Control through Cohesion and Repulsion Behaviours Combined with a Leadership, *International Journal of Advanced Robotic Systems*, vol. 13, p. DOI: 10.5772/62249.
20. Li K., Han X., Qi G. (2009), Formation and Obstacle-Avoidance control for Mobile Swarm Robots Based on Artificial Potential Field, in *Conference on Robotics and Biomimetics*.
21. Mukherjee R., Anderson D.P. (1993), Nonholonomic Motion Planning Using Stokes' Theorem. In: *IEEE International Conference on Robotics and Automation*, pp. 802–809.
22. Nagao Y., Uchiyama K. (2014), Formation Flight of Fixed-Wing UAVs Using Artificial Potential Field, in *29th Congress of the International Council of the Aerospace Sciences*, St. Petersburg.
23. Nelson D. R., Barber D. B., McLain T. W., Beard R. W. (2007), Vector Field Path Following for Miniature Air Vehicles, *IEEE Transactions on Robotics*, vol. 23, no. 3, pp. 519-529.
24. Nieuwenhuisen M., Schadler M., Behnke S. (2013), Predictive Potential Field-Based Collision Avoidance for Multicopters, *International Archives of Photogrammetry, Remote Sensing and Spatial Information Sciences*, Vols. XL-1/W2.
25. Suzuki M., Uchiyama K. (2010), Autonomous Formation Flight Using Bifurcating Potential Fields, in *27th International Congress of the Aeronautical Sciences*, Nice.
26. Suzuki M., Uchiyama K. (2011), Three-Dimensional Formation Flying Using Bifurcating Potential Fields, in *AIAA Guidance, Navigation, and Control Conference*, Chicago.
27. Tobias P., Krogstad T. R., Gravdahl J. T. (2008), UAV Formation Flight Using 3D Potential Field, in *16th Mediterranean Conference on Control and Automation*.
28. Virágh C., Vásárhelyi G., Tarcai N., Szórényi T., Somorjai G., Nepusz T., Vicsek T. (2014), Flocking Algorithm for Autonomous Flying Robots, *Bioinspiration & Biomimetics*, vol. 9, no. 2, p. 025012.

Acknowledgments: The research was funded by statutory funds of Department of Robotics and Mechatronics, Faculty of Mechanical Engineering, Białystok University of Technology (WZ/1/WM/2019).

# IDENTIFICATION OF ANALYTICAL DEPENDENCIES OF THE OPERATIONAL CHARACTERISTICS OF THE WORKPIECE CLAMPING MECHANISMS WITH THE ROTARY MOVEMENT OF THE INPUT LINK

Borys PRYDALNYI\*, Heorhiy SULYM\*\*

\*Faculty of Technology, Department of Applied mechanics, Lutsk National Technical University, Lvivska Str 75, 43018 Lutsk, Ukraine

\*\*Faculty of Mechanical Engineering, Bialystok University of Technology, ul. Wiejska 45C, 15-351 Bialystok, Poland

[prydalnyy30@gmail.com](mailto:prydalnyy30@gmail.com), [h.sulym@pb.edu.pl](mailto:h.sulym@pb.edu.pl)

received 7 October 2019, revised 5 May 2021, accepted 10 May 2021

**Abstract:** The research is devoted to the problem of determining the efficiency of the workpiece fixing mechanism operation. Improving characteristics of workpiece fixing is one of the required conditions to increase the cutting modes, which may help to enhance the machining productivity. The study investigates the main characteristics and general features of a new structure of clamping mechanisms with electromechanical actuators for fixation of rotation bodies. The main advantages of using electromechanical clamping actuators with self-braking gear are presented. Two simplified dynamical models for the description of different stages of the clamping process are developed. The calculation scheme was formulated to find out how the mass-geometric parameters of mechanism elements should influence the main characteristics of the clamping mechanisms of this type.

**Keywords:** the mechanism for clamping of rotation bodies, clamping actuator, self-braking screw gear, kinematic characteristics, workpiece clamping efficiency

## 1. INTRODUCTION

One of the main trends in the metalworking machine tool industry, which contributes to improving the processing efficiency, is to increase the cutting modes: the cutting speed (related to a spindle speed) and the thickness of the layer of material being removed in one pass of the tool (related to feed). As the possibility to increase the maximum processing modes to a large extent depends on the quality of fixture of a workpiece, it is necessary to provide the required value and stability of the clamping force over a wide range of spindle speeds. The process of clamping workpieces in a metalworking machine tool is carried out by using the clamping mechanism (CM). Since the CM is mounted on the spindle of the machine, it affects not only the efficiency of the workpiece clamping process but also the performance characteristics of the spindle assembly (spindle unit), in general. Any CM contains two main subsystems: "clamping actuator" (CA) and "clamping chuck". CA can be defined as an intermediate device for converting and transmitting energy in the form of a power flux from an energy source (ES) to the clamping chuck with functional dependence on it. Characteristics of the CA have a large influence on the main power characteristics of a CM. Thus, the magnitude of the clamping force, stability of the clamping force under the influence of various perturbations such as the influence of centrifugal forces, deviation size of a clamping surface, heterogeneity of physical-mechanical characteristics of the material of the workpiece, and change of power supply characteristics are essential. Characteristics such as response time during mechanism operation, reliability of maintaining a tense system state while holding a workpiece, possibility of effective management and regulation of work of a CM are also important. A typical CA uses different methods to maintain the workpiece clamping force (tense system state) during processing. The need to use a large number of energy converters to create clamping forces by using of typical CA designs leads to additional energy losses, reduced reliability and

efficiency of control of these mechanisms, increased sensitivity to external perturbations, complications of design, manufacturing and operation, etc. Not only does the efficiency of the energy converters work very often decrease with the increase of a spindle rotational speed, but their design also deteriorates the dynamic characteristic of a spindle assembly. The main researches for improving the productivity of the spindle unit in machine tools are dedicated to the detection of influence of bearings, optimal interaction of nodes, temperature influence, increasing vibration resistance and functional rigidity. Increasing the efficiency of creation clamping efforts can help to improve the processing efficiency through better utilization of the potential abilities of machine tools of the existing designs in particular. This explains the expediency of creating new designs of CA based on new structures that meet the above requirements.

## 2. THE MAIN DISADVANTAGES OF TRADITIONAL DESIGNS OF ACTUATORS OF THE CLAMPING MECHANISM

As a result of the analysis, the common problems of the main types of CA were identified and formulated. In the case when mechanical energy is supplied to the CA as an external axial force, there is an additional axial load on the spindle and its bearings. This can also lead to uncontrolled movement of the elements of the spindle assembly due to elimination gaps or elastic deformations. This reduces the accuracy of processing. Centrifugal inertia forces appear on the moving elements of CA converters (lever, wedge, etc) and constantly try to move them. It can cause uncontrolled negative changes in power characteristics of this mechanism during high-speed rotation of the spindle. The value of clamping effort created by a CA with the mechanisms of geometric closure depends on the variations in the size of the workpiece from its nominal values. The problem of a CA actuated by hydraulic pressure is that there is an occurrence of losses working fluid

when bringing it to the rotating spindle. Also, the inertia forces acting on the liquid at high speeds counteract its displacement, which reduces the efficiency of the mechanism. Both types of CA require using large external mechanisms for preparing and supplying input energy (mechanical or hydraulic).

On the basis of the obtained information, ways of improving structure for the development of new CA designs are revealed:

- Characteristics of the energy converters should not depend on the influence of the centrifugal forces of inertia.
- Keeping the system's tense state while holding the workpiece must be ensured without supplying energy from the outside.
- The number of different types of energy converters should be minimal to simplify construction and reduce energy loss.
- Input energy must be supplied without external force interaction that can cause appearance of uncontrolled radial displacement of spindle units or offset of the rotation axis.
- Units that may complicate balancing of the spindle assembly or disturb it over a short period should be avoided.
- Change and adjustment of the characteristics of the clamping process must be available without disassembling the mechanism.

The safest and most economical CAs are those whose contour of force interaction is closed by braking inside the mechanism. CA of this kind can be disconnected from the power source after reaching the required clamping force and provide support even in the case of a power failure of a machine tool. Several basic types of self-braking gears can be used in the CA: screw, wedge, helix and cam. Self-braking mechanisms in the form of screw gearing have become most widespread as they are more economical in manufacturing and operation due to their simpler construction.

### 3. DEVELOPMENT OF A TYPICAL STRUCTURE OF A NEW CLAMPING MECHANISM

Following the identified requirements, a new CA structure was developed, with predictably better characteristics and where the input energy is electric. The widespread electrical actuator is an electromotor with rotation motion. The output force of a CA must be linear for work as a clamping chuck. To transform rotation motion in linear, it's reasonable to use a screw gear with the ability to self-brake (self-lock caused due to friction forces). It can keep a tensioned state of the system making it possible to hold a workpiece during processing without having to supply energy from an outer source. In such a way, the number of energy converters is reduced to two: one electromagnetic and one mechanical. Working characteristics of both converters do not depend on of centrifugal inertial forces and deviations of clamp surface size from nominal values. One variant of this structure is embodied in the patented CA design [Patent UA95323]. A feature of this design is the specific usage of an electromotor when a stator is attached to the body of the machine tool and the rotor is installed on a spindle. To create an effective CA based on this structure, it is necessary to identify the typical mathematical dependencies for this structure between the mass-geometric parameters of the elements of the mechanism, and the kinematic and power characteristics. That is why, it is necessary to establish the basic dependencies that describe the characteristics of displacement of the CA output link (value of displacement, velocity) and the amount of energy (value of output effort) spent to clamp the workpiece in the CM with CA of the proposed design.

The block diagram of a typical collet CM in which the proposed CA is used can be represented by the following set of structural elements (Fig. 1): the energy source ES is usually an industrial electrical network with voltage  $U$ ; the switching device (SD), which controls the operation of the drive motor D, consisting of a stator and rotor (on the shaft of which rotation moment  $Ma_0$  occurs); the drive self-braking mechanism (DSBM) changes the movement characteristics of the output link of the drive motor M and captures the tense state of the CM after it is switched off; a clamping chuck (CC), which directly fixes the object of the clamping (OC) with  $Fr_2$  radial force.

Several types of control of engine D can be implemented in this structure of CM to automatically adjust the parameters of the CM, for which different backward linkages I, II and III (Fig. 1) are commonly used. The control system of electrical CA, the core element of which is the SD switching device, must ensure that in addition to  $Fr_2$  clamping force control, there is also mutual locking with the main drive of the machine, feed and auxiliary movements.

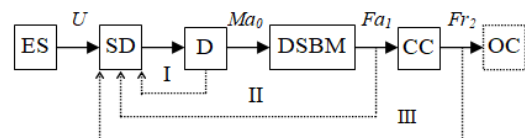


Fig. 1. Block diagram of a collet CM with the electrical CA and self-braking mechanism

The effective control of the operation of the CM with the electrical CA can be performed using a switching device (SD) by changing the stator current parameters that determine the rotor motion characteristics. The control signal may include characteristic operational values (displacement and force interaction) of the various CM subsystems and is transmitted to the SD through separate backward linkages I, II and III (Fig. 1). This improves the reliability and efficiency of the clamping process control. The influence of centrifugal inertia forces of unbalanced moving CM elements on changing the value of clamping force  $Fr_2$  can be determined from a function where the actual spindle speed is used as a variable.

Obtaining a predetermined value of clamping force  $Fr_2$  in CM with electrical CA can be carried out based on several principles of its control system organization. The simplest is the principle of control without deliberately limiting engine running time. In this case, the electrical CA drive motor operates in stopper mode operation until the rotor is stopped under the influence of resistance forces (overturning mode), which corresponds to the maximum value of the tense state for the given power supply characteristics. This is reflected in the characteristics of the motor current of the motor D and gives a signal for the switching device to switch it off. The system remains in the tense state which is supported by the self-braking mechanism (DSBM). Overloading of the drive motor during stopping is acceptable since it has a small duration. Other clamping process control principles use signals from sensors giving information about the value of displacement and force interaction in the CM subsystems to limit the clamping force and provide controlled stopping of the electrical CA engine. In these cases, the response time of the control equipment (relay and sensors) must be taken into account. The possibility of using different control schemes of electrical CA increases the efficiency of its usage in the CM for different technological equipment and different operation conditions.

In the proposed design of an electric CA (Fig. 2), the rotor of

the induction motor D is located on the threaded surface of the spindle with the possibility of their mutual movement, and the stator of electric CA is rigidly connected to the housing of the spindle assembly. Energy supply to the rotating spindle is carried out without contact – due to the influence of the stator electromagnetic torque. At the initial moment of operation of this CM, the rotor of the motor D electrical CA has an angular velocity relative to the stator, which is equal to the speed of rotation of the spindle. Rotation acceleration or deceleration of the rotor of motor D and its movement in relation to the spindle occurs under the action of the electromagnetic moment of stator due to the activation of motor D. This also results in the axial movement of the rotor on the spindle threaded surface with a force  $F_{a1}$ , which is the output force of electric CA.

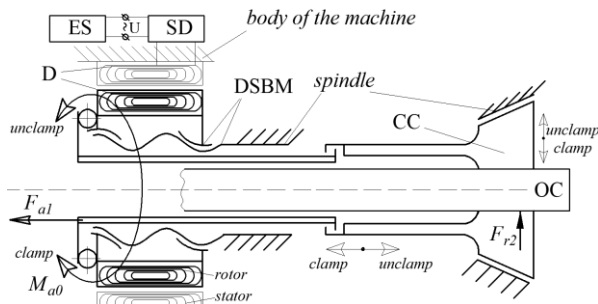


Fig. 2. Schematic diagram of electric CA according to the patent of Ukraine № 95323

#### 4. IDENTIFICATION OF ANALYTICAL DEPENDENCIES

The mathematical description of a multi-mass dynamic model, which reflects the working process of the CM with the proposed electric CA, can be carried out in accordance with the calculation scheme (Fig. 3a). Detailed calculations of this type are related to the difficulties in computation and their volume. Therefore, for practical calculations and further analytical studies, the multi-mass system is reduced to a single-mass system (Fig. 3b, c) with the equivalent moment of inertia  $J_{\Pi}$  and the equivalent torque  $M_{\Pi} = M_{a0}$ . On the scheme (Fig. 3b, c), the influence of forces of potential character (forces of elasticity) is reflected by the action of elastic elements with the corresponding stiffness coefficient  $c_{np}$ ,  $c_{\kappa}$ .

##### 4.1. Development of calculation schemes

It is reasonable to consider CM as a system in two cases: during the clearance  $\Delta$  adjustment, when mainly active forces of dissipative character are acting in the system, and during the creation of tension of the elastic system of CM (Fig. 3 b) when the forces of potential character dominate. The analysis of the clamping process in the CM with the electric CA (Fig. 3 b, c) should also take into account the forces of elasticity of the collet petals with the rigidity  $c_{nn}$ , stiffness of electric CA –  $c_{np}$ , and contact stiffness in the joints of the collet chuck cartridge  $c_{\kappa}$ . The study of the CA in the SM (Fig. 3) requires consideration of the kinematic characteristics of two interacting mechanical energy converters: a screw self-braking mechanism (DSBM) and a collet (CC).

In a screw-driven self-braking mechanism, the rotation rotor of D (which works like a nut in a screw mechanism) with an angular velocity  $\omega_{\delta}$  ensures its translational motion with the speed  $V_m$  transmitted to the output link of CA – “clamp pipe”. The relation-

ship between these kinematic parameters can be established based on the equality between the rotation angle of the motor rotor  $\varphi_{\delta}$  and the axial movement of the “clamp pipe”  $x_m$  in one complete turn of the rotor  $\phi_{\delta}/x_m = 2 \cdot \pi/h$  or

$$x_m = \frac{\phi_{\delta} \cdot h}{2\pi}, \quad (1)$$

where  $h$  is the pitch of the thread.

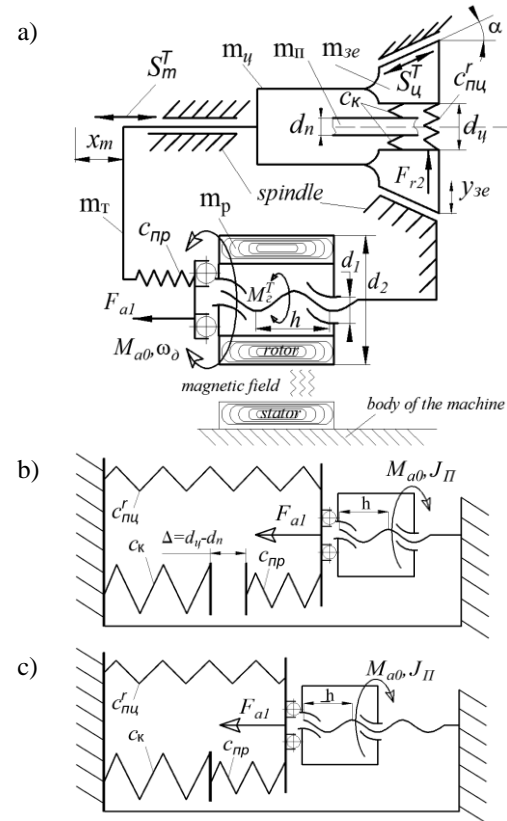


Fig. 3. Scheme of the CM: a) calculation scheme; b) simplified dynamic models during elimination gaps; c) simplified dynamic models when creating tension in the system

After differentiating the left and right parts of equations (1) in time, we obtain  $\partial x_m / \partial t = (\partial \phi_{\delta} / \partial t) \cdot h / 2\pi$ ,

$$V_m = \omega_{\delta} \cdot \frac{h}{2\pi} = 0.5 \omega_{\delta} \frac{h}{\pi} = \omega_{\delta} \cdot 0.5 d_1 \cdot \tan \psi, \quad (2)$$

where  $d_1$  is the diameter of the thread,  $\psi$  is the lead angle of the screw and  $\omega_{\delta}$  is the angular velocity of the rotor of the engine.

Express the value of  $i_s = 0.5 d_1 \cdot \tan \psi$  and substitute it in the equation (2). In that way, we get  $V_m = \omega_{\delta} \cdot i_s$  or:

$$V_m = \dot{\phi}_{\delta} \cdot i_s. \quad (3)$$

The movement of the collet chuck in the axial direction with velocity  $V_T$  provides radial movement of the clamping elements of the collet with velocity  $V_{3e}$ . The relationship between these kinematic parameters can be established based on the equality of relation of axial displacement  $x_m$  of the “clamp pipe” together with the body of the collet to the radial displacement  $y_{3e}$  of the collet surfaces intended to contact the object of fixation OC,  $x_m/y_{3e} = \tan \alpha$  from this it derives that:

$$y_{3e} = \frac{x_m}{\tan \alpha}, \quad (4)$$

$\partial x_m / \partial t = (\partial y_{3e} / \partial t) \cdot \tan \alpha$ ,  $V_m = V_{3e} \cdot \tan \alpha$  where  $\alpha$  is half of cone angle of collet.  $i_y = \tan \alpha$ , therefore,



$$V_{3e} = \frac{V_m}{i_y}. \quad (5)$$

After adding (3) to (5), we obtain

$$V_{3e} = \frac{\dot{\phi}_o \cdot i_z}{i_y} = \dot{\phi}_o \frac{i_z}{i_y}. \quad (6)$$

Analysis of the energy balance of the CM with proposed electrical CA (Fig. 3, a) during the workpiece clamping can be done by comparing the energy  $E_3$  consumed by the CM during a clamping process in general to the effective clamping energy  $E_{e\phi}$  consumed in the contact zone of collet surfaces with the object of fixation OC to create contact deformations. It should be noted that, unlike with pneumatic and hydraulic actuators, there is no component of energy lost for maintaining the system's tense state. Therefore, the calculation of the total energy required for operation of the CM can be carried out by the formula:

$$E_3 = E_{nm} + A_{mp} + E_{e\phi}, \quad (7)$$

where  $E_{nm}$  is the energy consumed for the movement of the masses of a unit CM,  $A_{mp}$  is the work (energy equivalent) performed to overcome friction forces, and  $E_{e\phi}$  is the effective clamping energy consumed in the contact zone of collet surfaces with the object of fixation OC to create contact deformations.

#### 4.2. Detection of dependencies between geometrical-mass parameters and power and kinematic characteristics of the mechanism

The efficiency coefficient of the mechanical part of the studied CM (Fig. 2) can be determined by the formula:

$$\eta_{3M} = \frac{E_{e\phi}}{E_{nm} + A_{mp} + E_{e\phi}}. \quad (8)$$

In this case,  $E_{nm}$  is the sum of the kinetic energy of mechanism links, which are rotating or have reciprocating motion:

$$E_{nm} = \sum_{i=1}^{i=n} \frac{m_i V_i^2}{2} + \sum_{i=1}^{i=n} \frac{I_i \omega_i^2}{2}, \quad (9)$$

$$E_{nm} = \frac{m_{oc}}{2} V_{oc}^2 + \frac{m_{p\partial}}{2} V_{p\partial}^2 + J_o \frac{\omega_o^2}{2},$$

$m_{oc} = m_p + m_m + m_y$ , where  $V_{oc}$ ,  $m_{oc}$  are, respectively, linear velocity (equal to "clamp pipe" velocity  $V_m$ ) and total mass of CM elements moving in the axial direction: motor rotor, "clamp pipe", collet of the clamping mechanism;  $m_{p\partial}$ ,  $V_{p\partial}$  are, respectively, the mass and linear velocity of the CM elements moving in the radial direction, in this case  $m_{p\partial} = m_{3e}$ , where  $m_{3e}$  is the mass of clamping elements of the collet and  $V_{p\partial} = V_{3e}$ , where  $V_{3e}$  is the radial speed of movement of clamping elements of the collet;  $J_o$ ,  $\omega_o$  are the moment of inertia of the rotor and its angular velocity.

Analytical dependencies (6) do not take into account the mass of the workpiece that moves with the collet, since it can change significantly in each specific cycle of fixation, which distorts the value of the efficiency as an inherent characteristic of the CM of the investigated structure.

Moment of inertia of the engine rotor  $J_o = m_p(d_1^2 + d_2^2)/8$ . According to (2), (5) between  $\omega_o$ ,  $V_{3e}$  and  $V_m$ , there are certain kinematic dependencies that are determined according to the calculation scheme:  $V_{oc} = V_m = \omega_o \cdot 0.5d_1 \cdot tg\psi$ ,  $V_m = V_{3e} \cdot ctg\alpha$ ,  $V_{p\sigma} = V_{3e} = \omega_o \cdot 0.5d_1 \cdot tg\psi \cdot tg\alpha$ . Then (9) can be

written in the following form:

$$E_{nm} = \frac{1}{8} (\omega_o d_1 tg\psi)^2 \left( m_{oc} + m_{p\sigma} tg^2 \alpha + 0.5 \frac{m_p (d_1^2 + d_2^2)}{(d_1 tg\psi)^2} \right) \quad (10)$$

The work  $A_{mp}$  (energy equivalent) performed to overcome the friction forces in CM consists of the following works: friction forces  $S_m^T$  of the "clamp pipe" in contact with the spindle during their mutual movement on the value of the "clamp pipe" stroke length  $x_m$ ; the friction forces  $S_\mu^T$  in contact with the collet cone with the spindle during their mutual movement on the value of the collet stroke length  $x_y = x_m / \cos \alpha$ ; given the proximity of the value  $\cos \alpha$  from 0.97 to 1, the calculations may be simplified to approximately  $x_y \approx x_m$ ; friction in the screw gear of the DSBM, which create the torque of friction forces  $M_s^T$  when turning with the angle  $\phi_o$ .

$$A_{mp} = S_m^T \cdot x_m + S_y^T \cdot x_m + M_s^T \cdot \phi_o. \quad (11)$$

The moment created by the forces of friction in the screw gear  $M_s^T$  can be defined as the action of the tangential component of the friction forces  $F_t$  with the shoulder equal to half the average diameter of the screw thread  $M_s^T = 0.5d_1 F_t$ . The torque generated by the friction in the connection bearings of the rotor to the "clamp pipe" is extremely small compared to  $M_s^T$ , so we can neglect its magnitude. The tangential component  $F_t$  of the friction force depends on the axial load  $Fa_1$  arising at the output of the gear.  $F_t = Fa_1 \cdot tg\phi^T$ , where  $\phi^T$  is the angle of friction in the threaded connection. Thus, the moment created by the friction forces in the screw transmission under load  $Fa_1$  can be determined from the following dependency:

$$M_s^T = 0.5 \cdot d_1 \cdot Fa_1 \cdot tg\phi^T. \quad (12)$$

The friction force between the surfaces of the collet cone and the spindle cone with the angle  $2\alpha$  is determined by the formula:

$$S_y^T = \frac{z \times Fa_1}{\cos \alpha + (\sin \alpha) / f_y}, \quad (13)$$

where  $z$  is the number of the collet segments and  $f_y$  is the coefficient of friction in the conical coupling of the collet with the spindle.

The force  $S_m^T$  of friction "clamp pipe" with a spindle:

$$S_m^T = g \cdot m_2 \cdot f_m, \quad (14)$$

where  $g$  is the free fall acceleration,  $m_2 = m_m + m_n$  is the mass equal to the sum of the mass of the "clamp pipe" and the workpiece (as a rod), and  $f_m$  is the coefficient of friction in the coupling of the "clamp pipe" with the spindle.

Using (12), (13) and (14), we write (11) as follows:

$$A_{mp} = Fa_1 \frac{\phi_o h}{2\pi} \left( \frac{gm_2 f_m}{Fa_1} + \frac{z}{\cos \alpha + (\sin \alpha) / f_y} + tg\phi^T \cdot ctg\psi \right). \quad (15)$$

Effective clamping energy  $E_{e\phi} = z \int_0^{h_k} Fr_2(h_k) dh_k$ , where  $h_k$  is the convergence in contact points between collet and spindle under the action of a normal clamping force, and the formula for determining it was obtained by experimentally  $h_k = f(S^k, Fr_2, \Delta d)$ , where  $S^k$  is the area of contact of the respective ribbed surfaces of the collet with the object of fixation. According to literary sources:

$$E_{e\phi} = \frac{m \cdot S^k \cdot z \cdot h_k}{A_M^{(1/m)} \cdot (1 + m)}, \quad (16)$$

where  $A_M$ ,  $m$  are coefficients selected according to the conditions

of the clamping process. For clamping conditions with a full fit of the clamping elements and object of fixation,  $m=1$ ,  $A_M=0.13$  and dependency (16) takes shape:

$$E_{e\phi} \approx 3.82 \cdot S^k \cdot z \cdot h_k. \quad (17)$$

Compute of the value of the work efficiency coefficient of clamping mechanisms with the electromechanical actuator derives from putting dependencies (10), (15), (17) into (8). Choosing appropriate characteristics of the elements of the new structure conduces to elimination of the problems related to increasing efficiency of fixation of a workpiece for high-performance machining. The obtained analytical dependencies (10), (15), (17), (18) make it possible to identify values that describe the efficiency of the CM and depend on some geometric and mass parameters of the elements of the mechanism:

$$\eta_{3M} = 3.82 S^k z h_k \left/ \frac{1}{8} (\omega_d d_1 t g \psi)^2 \times \left( m_{oc} + m_{p\partial} g^2 \alpha + 0.5 \frac{m_p (d_1^2 + d_2^2)}{(d_1 t g \psi)^2} \right) + F a_1 \frac{\phi h}{2\pi} \left( \frac{g m_2 f_m}{F a_1} + \frac{z}{\cos \alpha + (\sin \alpha)/f_u} + t g \phi^T \cdot c t g \psi \right) \right. \quad (18)$$

$$+ 3.82 \cdot S^k \cdot z \cdot h_k.$$

To illustrate the example of using the dependence (18), the efficiency of the prototype mechanism [16] is calculated. The separated components (10), (15), (17) of the expression (18) are calculated. In accordance with the dependence (10), the value of  $E_{NM}$  is determined at the parameters of the mechanism:  $\omega_d = 314 \text{ rad/s}$ ,  $d_1 = 0.09 \text{ m}$ ,  $t g \psi = 0.01$ ,  $m_{oc} = 3 \text{ kg}$ ,  $m_{p\partial} = 0.4 \text{ kg}$ ,  $t g \alpha = 0.268$ ,  $m_p = 2.4 \text{ kg}$ ,  $d_2 = 0.14 \text{ m}$ ,  $E_{NM} = \frac{1}{8} (314 \cdot 0.09 \cdot 0.01)^2 \times \left( 3 + 0.4 \cdot 0.268^2 + 0.5 \frac{2.4(0.09^2 + 0.14^2)}{(0.09 \cdot 0.01)^2} \right) = 409.7 \text{ Nm}$ .

In accordance with the dependence (15), the value of  $A_{mp}$  is determined at the parameters of the mechanism:  $F a_1 = 1200 \text{ N}$ ,  $\phi_d = 44 \text{ rad}$ ,  $h = 2 \cdot 10^{-3} \text{ m}$ ,  $g = 9.81 \text{ m/s}^2$ ,  $m_2 = 3.2 \text{ kg}$ ,  $f_m = 0.3$ ,  $z = 3$ ,  $\alpha = 15^\circ$ ,  $t g \phi = 0.2$ ,  $c t g \psi = 5$ ,  $f_u = 0.1$ ,  $A_{mp} = 1200 \frac{44 \cdot 2 \cdot 10^{-3}}{2\pi} \times \left( \frac{9.81 \cdot 3.2 \cdot 0.3}{1200} + \frac{3}{0.966 + 0.259/0.1} + 0.2 \cdot 5 \right) = 31.1 \text{ Nm}$ .

In accordance with the dependence (17), the value of  $E_{e\phi}$  is determined at the parameters:  $S^k = 95 \cdot 10^{-5} \text{ m}^2$ ,  $z = 3$ ,  $h_k = 100 \text{ kN/m}$ ,  $E_{e\phi} = 3.82 \cdot 10^{-5} \cdot 3 \cdot 100 \text{ kNm}$ .

In accordance with the dependence (8), the efficiency coefficient  $\eta_{3M}$  of the CM [16] is:

$$\eta_{3M} = \frac{1080}{409.7 + 31.1 + 1080} = 0.71.$$

The obtained dependences (18) allow to carry out the analysis of influence of the CM parameters on its work efficiency. It enhances the efficiency of design work allowing to find more appropriate parameters easier. Thus, (18) demonstrates that one of the promising ways to increase the efficiency of the CM is to reduce the value of moving masses  $m_{oc}$ ,  $m_p$ ,  $m_2$  and other. Reduction of the mass  $m_p$  of the motor rotor can be achieved through the use of modern high-torque motors with a rotor that has a much smaller mass, outer diameter  $d_2$  and moment of inertia. The weight of the elements of the CM can be reduced through the use of composite and polymeric materials which weigh three up to four times less. For example, the rod connecting the clamp drive and the clamping chuck which is made in the form of a pipe can be

made of carbon fibre. Using the formula (18) gives enhanced opportunities for the designer to make informed decisions about the feasibility of using new structural elements and materials, improving the quality of surfaces machining to reduce the coefficients of friction  $f_m$ ,  $f_u$ . That is, (18) makes it possible to evaluate the technical solutions in terms of comparing the costs of their implementation and the magnitude of productivity gains. Determining the appropriate periods between maintenance is dependent on the allowable amount of loss of the mechanism efficiency due to its normal wear. The level of degradation of the friction surfaces and the change of the friction coefficient allows to calculate the level of reduction of the mechanism productivity by means of (18) and to make more accurate decisions about the need for maintenance or overhaul.

The proposition would change the parameters  $m_{oc}$  and  $m_{oc}$  by making the parts of the mechanism from titanium with the purpose of improving. The magnitude of the change in the part's mass when changing its material while keeping its strength can be determined by comparing the coefficients of specific strength of each material. The specific strength is a material's strength divided by its density. In the manufacture of parts of titanium, their weight will be twice less than that made of alloy steel and two and a half times less compared to high-quality carbon steel with providing the same strength. The masses  $m'_{oc} = 1.5 \text{ kg}$  and  $m'_p = 1.2 \text{ kg}$  of the parts which are made of new material are reduced by 50% comparatively with the previous variant. The diameter of the rotor  $d'_2 = 0.13 \text{ m}$  can be reduced by 7% by using more expensive special manufacturing technologies. The parameters  $m_{oc}$ ,  $m_p$  and  $d_2$  have an influence on the value  $E_{NM}$ , and consequently on the efficiency  $\eta_{3M}$ . The value of  $E'_{NM}$  determined at the new parameters of the mechanism is:

$$E'_{NM} = \frac{1}{8} (314 \cdot 0.09 \cdot 0.01)^2 \times \left( 1.5 + 0.4 \cdot 0.268^2 + 0.5 \frac{1.2(0.09^2 + 0.13^2)}{(0.09 \cdot 0.01)^2} \right) = 184.88 \text{ Nm}.$$

The value of the mechanism's efficiency with new parameters  $\eta'_{3M}$  can be calculated with (18):  $\eta'_{3M} = \frac{1080}{184.88 + 31.1 + 1080} = 0.833$

The proposed changes of the masses and geometrical parameters resulted in the improvement of the efficiency coefficient  $\eta'_{3M} = 0.833$  comparatively with the previous  $\eta_{3M} = 0.71$  by 17%.

## 5. CONCLUSION

As a result of the evaluation of traditional CM design function, the main disadvantages, and factors limiting clamping process efficiency and in particular at high speeds of rotation, have been identified. Based on the obtained information, the characteristics of the elements and the structure of the CM with improved characteristics are revealed and described. Following the example of the patented mechanism design of this type, function is considered, and the calculation scheme and simplified dynamic models describing different stages of its work are made. It is revealed that for the mechanisms of this type, the first stage of operation which is related to elimination of the gaps is distinguished and displayed in the relatively enlarged rotation angle of the input link (rotor) in the free-running mode. Therefore, the special feature of the mechanism of the proposed structure is in the possibility of using the work of inertia forces of the input link, the magnitude of which increases over its acceleration period, can be adjusted and de-

depends on the magnitude of the rotation angle of the rotor during free-running. Also, by changing the geometrical-mass characteristics (moment of inertia) of the rotating input link, the force characteristics of the clamping process can be corrected.

The calculation scheme was formulated to determine mass-geometric parameters of mechanism elements should influence the main characteristics of the clamping mechanisms of this type. Based on the revealed information, dependencies for determining the specific kinematic and dynamic characteristics and the value of the work efficiency coefficient of the clamping mechanism of this type were found. The obtained dependencies are among the necessary prerequisites for creating an automatic system for calculating the work characteristics of CM of this type. Usage of obtained analytical dependence enhances the efficiency of design work and operation of the CM due to the possibility of selecting the mass and geometrical parameters of the elements.

## REFERENCES

1. Alquraan T., Kuznetsov Yu., Tsvyd T. (2016) High-speed clamping Mechanism of the CNC lathe with compensation of centrifugal forces, *Procedia engineering*, 150, 689-695.
2. An J., Jiamin C., Wenguo Y. (2019), Measurement of spindle radial error based on target trajectory tracking, *Measurement*, 146, 179-185.
3. Bediz B., Gozen B.A., Korkmaz E., Ozdoganlar O. B. (2014), Dynamics of ultra-high-speed (UHS) spindles used for micromachining, *International Journal of Machine Tools and Manufacture*, 87, 27-38.
4. Budniak Z. (2015), Modelling and numerical analysis of assembly system, *Acta mechanica et Automatica*, 9(3), 145-150.
5. Chao Xu, Jianfu Z., Pingfa F. (2014), Characteristics of stiffness and contact stress distribution of a spindle-holder taper joint under clamping and centrifugal forces, *International Journal of Machine Tools & Manufacture*, 82-83, 21-28.
6. Dogariu C., Bardac D. (2014), Prediction of the structural dynamic behavior of high speed turning machine spindles, *Applied Mechanics and Materials*, 555, 567-574.
7. Estrems M., Arizmendi M., Cumbicus W.E., López A. (2015), Measurement of clamping forces in a 3 jaw chuck through an instrumented aluminium ring, *Procedia Engineering*, 132, 456-463.
8. Fedorynenko D., Sapon S., Boyko S. (2016), Accuracy of spindle units with hydrostatic bearings, *Acta Mechanica et Automatica*, 10(2), 117-124.
9. Fedorynenko D., Sapon S., Boyko S., Urlina A. (2017), Increasing of energy efficiency of spindles with fluid bearings, *Acta Mechanica et Automatica*, 11(2), 204-209.
10. Foremny E., Schenck C., Kuhfuß B. (2016), Dynamic Behavior of an Ultra Precision Spindle used in Machining of Optical Components, *Procedia CIRP*, 46, 452-455.
11. Grama S.N., Mathur A., Badhe A.N. (2018), A model-based cooling strategy for motorized spindle to reduce thermal errors, *International Journal of Machine Tools and Manufacture*, 132, 3-16.
12. Grossi N., Scippa A., Montevicchi F. (2016), A novel experimental-numerical approach to modeling machine tool dynamics for chatter stability prediction, *Journal of advanced mechanical design systems and manufacturing*, 10(2), #15-00547.
13. Harris P., Linke B., Spence S. (2015), An Energy Analysis of Electric and Pneumatic Ultra-high Speed Machine Tool Spindles, *Procedia CIRP*, 29, 239-244.
14. Jia Q., Li B., Wei Y., Chen Y., Yuan X. (2016), Axiomatic Design Method for the Hydrostatic Spindle with Multisource Coupled Information, *Procedia CIRP*, 53, 252-260.
15. Kono D., Mizuno S., Muraki T., Nakaminami M. (2019), A machine tool motorized spindle with hybrid structure of steel and carbon fiber composite, *CIRP Annals*, 68(1), 389-392.
16. Li, W.; Zhou, Z. X.; Xiao, H. (2015), Design and evaluation of a high-speed and precision microspindle, *International journal of advanced manufacturing technology*, 78(5), 997-1004.
17. Liu T., Gao W., Zhang D., Tian Y. (2017), Analytical modeling for thermal errors of motorized spindle unit, *International Journal of Machine Tools and Manufacture*, 112, 53-70.
18. Longfei Z., Jun Z., Chao Z. (2019), A new method for field dynamic balancing of rigid motorized spindles based on real-time position data of CNC machine tools, *International journal of advanced manufacturing technology*, 102 (5-8), special edition, 1181-1191.
19. Matsubara A., Tsujimoto S., Kono D. (2015), Evaluation of dynamic stiffness of machine tool spindle by non-contact excitation tests, *CIRP Annals*, 1.V. 64(1), 365-368.
20. Mori K., Bergmann B., Kono D., Denkena B., Matsubara A. (2019), Energy efficiency improvement of machine tool spindle cooling system with on-off control, *CIRP Journal of Manufacturing Science and Technology*, 25, 14-21.
21. Postel M., Aslan D., Wegener K., Altintas Y. (2019), Monitoring of vibrations and cutting forces with spindle mounted vibration sensors, *CIRP Annals*, 68(1), 413-416.
22. Prydalnyi B. (2020), Characteristics of electromechanical clamping mechanism with asynchronous electric motor, *International Conference Mechatronic Systems and Materials (MSM)*, 1-5.
23. Rabreau C., Ritou M., Le Loch S., Furet B. (2017), Investigation of the Evolution of Modal Behavior of HSM Spindle at High Speed, *Procedia CIRP*, 58, 405-410.
24. Ritou M., Rabreau C., Le Loch S., Furet B., Dumur D. (2018), Influence of spindle condition on the dynamic behavior, *CIRP Annals*, 67(1), 419-422.
25. Shaoke W., Jun H., Fei D. (2019), Modelling and characteristic investigation of spindle-holder assembly under clamping and centrifugal forces, *Journal of mechanical science and technology*, 33(5), 2397-2405.
26. Thorenz B., Westermann H.-H., Kafara M., Nützel M., Steinhilper R. (2018), Evaluation of the influence of different clamping chuck types on energy consumption, tool wear and surface qualities in milling operations, *Procedia Manufacturing*, 21, 575-582.
27. Wang H.J. (2013), Study of dynamics characteristics for precision motor spindle system, *Advanced materials research*, 819, 389-392.
28. Xu C., Zhang J., Feng P., Yu D., Wu Z. (2014), Characteristics of stiffness and contact stress distribution of a spindle-holder taper joint under clamping and centrifugal forces, *International Journal of Machine Tools and Manufacture*, 82-83, 21-28.
29. Yadav M.H., Mohite S.S. (2018), Controlling deformations of thin-walled Al 6061-T6 components by adaptive clamping, *Procedia Manufacturing*, 20, 509-516.
30. Yang Y., Zhang W.H., Ma Y.C., Wan M. (2015), Generalized method for the analysis of bending, torsional and axial receptances of tool-holder-spindle assembly, *International Journal of Machine Tools and Manufacture*, 99, 48-67.
31. Yuan S.M. (2014), The analysis of static and dynamic characteristics of motorized high-speed spindle based on sensitivity analysis of fem model, *Applied mechanics and materials*, 43, 376-381.
32. Zabielski R., Trochimczuk R. (2011), Wybrane problemy projektowania wysokoobrotowych elektrowrzecion frezarskich o niestandardowym łożyskowaniu, *Acta Mechanica et Automatica*, 5(1), 131-136.
33. Zhang S., Yu J., To S., Xiong Z. (2018), A theoretical and experimental study of spindle imbalance induced forced vibration and its effect on surface generation in diamond turning, *International Journal of Machine Tools and Manufacture*, 133, 61-71.

Acknowledgement: The work has been accomplished under the research activity of Borys Prydalnyi at the Faculty of Mechanical Engineering, Białystok University of Technology, Poland, in frame of the PROM Project: "International scholarship exchange of PhD candidates and academic staff" within the Operational Programme Knowledge Education Development, co-financed from the European Social Fund.